



TECHNISCHE  
UNIVERSITÄT  
WIEN

# DIPLOMARBEIT

Electrochemical Characterization of  $(\text{La,Sr,Ca})_2\text{Co}_{2-x}\text{Mn}_x\text{O}_{6-\delta}$  as  
Cathode Materials for Solid Oxide Fuel Cells

Ausgeführt am Institut für

Chemische Technologien und Analytik

der Technischen Universität Wien

unter Anleitung von

Univ.-Prof. Dipl.-Phys. Dr.rer.nat. Jürgen Fleig

Dr.rer.nat. Edvinas Navickas, MSc

Dipl.-Ing. Dr.rer.nat. Markus Kubicek

durch

Alexander Viernstein, BSc.

Gymnasiumstraße 26/18

1180 Wien

Wien, am 23.August 2017

---

Unterschrift

In diesen wenigen Zeilen möchte ich all denjenigen meinen Dank aussprechen die mich auf meinem bisherigen Weg begleitet haben und ohne die diese Seiten nie entstanden wären.

An erster Stelle, vielen Dank Professor Fleig, dass Du mir die Gelegenheit gabst die Elektrochemie kennenlernen zu dürfen und die Arbeit in Deiner Arbeitsgruppe ermöglicht hast.

Weiters vielen Dank an meine beiden Betreuer Edvinas und Markus, ohne eure fachliche Unterstützung und Geduld wäre dies Alles nicht möglich gewesen. Durch das ausgezeichnete Arbeitsklima war es so gut wie an allen Tagen eine Freude an den Arbeitsplatz zu kommen. Daher danke an das gesamte restliche Forschungsteam.

Vielen Dank Werner Artner und Berthold Stöger für eure Hilfe bei den XRD-Messungen bzw. beim Auswerten der Ergebnisse.

Die Studentenzeit ist ein Lebensabschnitt, in dem man sich nicht nur fachliches Wissen aneignet, sondern hoffentlich auch Freundschaften fürs Leben schließt. Diese haben mich durch so manche herausfordernde Zeit gebracht. Vielen Dank, Viktor, Mathias, Klaus, Stephi, Ester, Eml, Marie, Jan, Marco und Clara, es war mir eine Freude. Wenn ich so an die gemeinsamen Laborpraktika, Festl und diversen Whiskeyverkostungen denke, kann ich nur sagen: „Sau geile Zeit, uns ist wirklich nicht fad geworden, lustig wars.“ Außerdem vielen Dank Sven für die wochenendlichen, feiertäglichen Gespräche und Kaffeepausen.

Natürlich auch an Bernhard, Johanner, Maxi und Consti vielen Dank. Jetzt sind wir schon fast 25 Jahre dieses Fünfergespann, ich glaube ihr wisst was ihr mir bedeutet.

Zu guter Letzt, möchte ich meinen Eltern danken, dass sie mir das Studium ermöglicht und mir das nötige Rüstzeug mitgegeben haben.

Sollte ich jemanden in meiner Verwirrtheit vergessen haben, auch an ihn/sie, vielen Dank.

Viel Spaß beim Lesen, ich weiß, nicht alle erwähnten Personen werden ihn haben, aber zum Glück sind unsere Interessen weit gefächert.

## Abstract

Intermediate temperature fuel cells, with a working temperature between 500 °C and 700 °C, suffer from the slow reduction kinetics of oxygen at the cathode side which is responsible for most of the resistive losses. The aim of this work was the investigation of the electrical properties, oxygen exchange kinetics and diffusion processes of  $^{18}\text{O}$  tracer ions in advanced cathode materials, such as perovskites with the generalized structure  $(\text{La,Ca,Sr})_2\text{Co}_{2-x}\text{Mn}_x\text{O}_{6-\delta}$ .

First, targets materials were synthesized by a Pechini-type method. Subsequently thin films of different compositions were grown by pulsed laser deposition (PLD) under various  $p(\text{O}_2)$  on three different single crystal substrates, since the background pressure in the PLD chamber and the used substrate have a massive impact on the thin film structure and properties. For ionic conductivity determination, some of the samples were microstructured by UV-lithography and impedance spectroscopy was performed.

The electrical properties of bulk and thin film samples were investigated by van der Pauw method. Keeping the Co/Mn ratio 1:1, a higher conductivity for Ca and Sr doped samples is observed due to p-type doping. Moreover, by changing the relative amount of Co without A-site doping conductivity can also be enhanced. All produced and investigated bulk samples possess a lower electrical conductivity and higher activation energy than  $\text{La}_{0.8}\text{Sr}_{0.2}\text{MnO}_3$  (LSM).

For applicable cathode materials, a good oxygen diffusion is crucial. Hence,  $\text{La}_2\text{CoMnO}_6$  thin film were investigated by performing  $^{18}\text{O}$  exchange experiments and ToF-SIMS depth profiling. With these techniques, the diffusion coefficient  $D^*$  and the surface exchange coefficient  $k^*$  were determined. In  $\text{La}_2\text{CoMnO}_6$  samples, grain boundary diffusion plays a vital role. Diffusion coefficients of the grain boundaries are one to two orders of magnitude higher than the bulk diffusion coefficients and stay constant when  $p(\text{O}_2)$  in the PLD-chamber during thin film growth is increased. Additionally, a high  $p(\text{O}_2)$  leads to an additional diffusion process and is most likely related to the dislocation concentration.

For the determination of the ionic area specific resistance of  $\text{La}_2\text{CoMnO}_6$  impedance spectroscopy was carried out. Activation energies below 550 °C indicate a triple phase boundary path of oxygen reduction. If the samples were heated for the first time above 500 °C

irreversible changes took place and the activation energies and resistivity rose tremendously in further measurements.

## Kurzfassung

Bei Mitteltemperatur-Brennstoffzellen, mit einer Betriebstemperatur zwischen 500 °C und 700 °C, stellt die langsame Reaktionskinetik der Sauerstoffreduktion an der Kathode ein ernstzunehmendes Problem dar. Sie ist oft verantwortlich für den größten Teil der elektrischen Verluste. Daher ist das Ziel dieser Arbeit, die elektrischen Eigenschaften, die Sauerstoffaustauschkinetik und die Diffusionsprozesse von  $^{18}\text{O}$  in neuen Kathodenmaterialien, wie den Perowskiten mit einer Zusammensetzung  $(\text{La,Ca,Sr})_2\text{Co}_{2-x}\text{Mn}_x\text{O}_{6-\delta}$  zu untersuchen.

Zu Beginn wurden targets über eine Abwandlung der Pechini-Methode synthetisiert. Anschließend wurden Dünnschichten mit Hilfe gepulster Laserabscheidung auf drei verschiedenen Einkristallsubstraten und unter verschiedenen  $p(\text{O}_2)$  aufgewachsen, da Substrat und Hintergrunddruck Einfluss auf die Struktur und Eigenschaften des Dünnschichtfilms haben. Zu guter Letzt wurden ausgewählte Proben mittels UV-Lithographie für impedanzspektroskopische Messungen mikrostrukturiert, um deren ionische Leitfähigkeit zu bestimmen.

Die elektrischen Eigenschaften wurden mit Hilfe der van der Pauw-Methode untersucht. Hierbei wurden bulk-Proben und Dünnschichten vermessen. Bei einem Co/Mn Verhältnis von 1:1 kann durch Dotieren des A-Platzes der Perowskite mit Ca und Sr (p-type doping) eine Verbesserung der Leitfähigkeit erzielt werden. Wenn der Co-Anteil gegenüber dem Mn-Anteil verändert wird, kann eine Verbesserung der Leitfähigkeit von Dünnschichtproben beobachtet werden, wobei alle hergestellten Proben eine schlechtere elektrische Leitfähigkeit und höhere Aktivierungsenergie als  $\text{La}_{0.8}\text{Sr}_{0.2}\text{MnO}_3$  (LSM) aufweisen.

Für Kathoden ist eine gute Sauerstoffdiffusion notwendig, daher wurden  $\text{La}_2\text{CoMnO}_6$  Dünnschichten mit Hilfe von  $^{18}\text{O}$  Austauschexperimenten und ToF-SIMS Tiefenprofilmessungen untersucht. Mit diesen konnten Diffusionskoeffizienten und Oberflächenaustauschkoeffizienten bestimmt werden. In den  $\text{La}_2\text{CoMnO}_6$  Proben spielt die Diffusion über die Korngrenzen eine wichtige Rolle, der Korngrenzendiffusionskoeffizient ist um zwei bis drei Ordnungen größer als der Volumendiffusionskoeffizient. Unterschiedliche Sauerstoffpartialdrücke während der Herstellung der Dünnschichten beeinflusst den Korngrenzendiffusionskoeffizienten nicht. Hingegen verursacht ein hoher Partialdruck die

Entstehung eines zusätzlichen Diffusionsprozesses, dieser steht höchst wahrscheinlich in einem Zusammenhang mit der Versetzungskonzentration in den Proben.

Für die Bestimmung des ionischen flächenbezogenen Widerstandes von  $\text{La}_2\text{CoMnO}_6$  wurden impedanzspektroskopische Messungen durchgeführt. Die erhaltenen Aktivierungsenergien unter  $550\text{ °C}$  weisen auf eine Sauerstoffreduktion an der Dreiphasengrenzfläche hin. Nachdem die Mikroelektroden erstmalig über  $550\text{ °C}$  erhitzt wurden, kam es zu irreversiblen Veränderungen der Proben und folglich stiegen die Aktivierungsenergien und Widerstände dramatisch an. Dies steht möglicherweise in Zusammenhang mit einer strukturellen Veränderung der Proben, oder kann auf eine mit dem verwendeten Photolack verknüpften Degradation zurückgeführt werden.

# Contents

1. Introduction .....	7
2. Theoretical Background .....	10
2.1 Solid Oxide Fuel Cells (SOFCs) .....	10
2.2 Perovskites .....	11
2.3 Mixed Ionic-Electronic Conductors (MIEC).....	13
2.4 $\text{La}_2\text{CoMnO}_{6-\delta}$ (LCM).....	14
2.5 Defects and Diffusion in Solids.....	16
2.6 Pulsed Laser Deposition (PLD).....	20
2.7 Van der Pauw Measurements .....	21
2.7.1 Basics of the Method.....	21
2.7.2 Conductivity Activation Energy and its Calculation from Arrhenius Plots .....	22
3. Experimental Part.....	24
3.1 Sample Preparation using a Pechini-type Method.....	24
3.2 Pulsed Laser Deposition.....	25
3.3 Microelectrode Preparation .....	26
3.3.1 UV-Lithography .....	26
3.3.2 $\text{Ar}^+$ Etching.....	26
3.4 Atomic Force Microscopy (AFM).....	27
3.5 Transmission Electron Microscopy (TEM).....	27
3.6 Van der Pauw Measurements .....	27
3.8 X-ray Diffraction (XRD Measurements).....	30
3.9 $^{18}\text{O}$ Gas Exchange and ToF-SIMS Tracer Depth Profiling .....	31
3.10 Impedance Spectroscopy.....	31
4. Results and Discussion.....	33
4.1. Powder X-ray Diffraction (XRD Measurements) .....	33
4.1.1 Purity Check PLD-Targets .....	33
4.1.1.1 LCM Target.....	33
4.1.1.2 LCCM Target .....	34
4.1.1.3 LSCM Target.....	35
4.1.1.4 $\text{LaCo}_{0.4}\text{Mn}_{0.6}\text{O}_3$ Target .....	36
4.1.1.5 $\text{LaCo}_{0.6}\text{Mn}_{0.4}\text{O}_3$ Target .....	37

4.1.2 LCM, LCCM and LSCM Cell Parameters .....	38
4.1.2.1 LCM Cell Parameters and Crystal Structure .....	38
4.1.2.2 LCCM Cell Parameters and Crystal Structure .....	40
4.1.2.3 LSCM Cell Parameters and Crystal Structure .....	42
4.2 Atomic Force Microscopy (AFM Measurements) .....	43
4.3 Transmission Electron Microscopy Images (TEM) .....	44
4.4 Van der Pauw Measurements .....	46
4.4.1 Bulk Samples .....	46
4.4.2 $\text{LaCo}_{0.5}\text{Mn}_{0.5}\text{O}_3$ Thin Film Samples .....	50
4.4.3 $\text{LaCo}_{0.4}\text{Mn}_{0.6}\text{O}_3$ Thin Film Samples .....	53
4.4.4 $\text{LaCo}_{0.6}\text{Mn}_{0.4}\text{O}_3$ Thin Film Samples .....	55
4.5 Tracer Diffusion Measurements .....	58
4.5.1 LCM $^{18}\text{O}$ Tracer Depth Profiles .....	58
4.5.1.1 LCM Samples Deposited with 1 Hz Repetition Rate .....	58
4.5.1.2 LCM Samples Deposited with 5 Hz Repetition Rate .....	60
4.5.1.3 1 Hz and 5 Hz Deposition Rate, Comparison of $D^*$ and $k^*$ Values .....	62
4.5.1.4 Grain Size Dependency on $p(\text{O}_2)$ and Quality of the Fits .....	63
4.5.2 Strain Effect for Oxygen Diffusion .....	64
4.6 Impedance Spectroscopy of LCM Microelectrodes .....	66
4.6.1 LCM 05 .....	66
4.6.2 LCM 06 and LCM 07 .....	70
5. Conclusion .....	75
6. Appendix .....	77
6.1 List of Figures .....	77
6.2 List of Tables .....	79
7. References .....	80

## 1. Introduction

Fuel cells are able to convert chemical energy directly to electrical energy. They are not limited to the Carnot efficiency. Facing greenhouse effect and global warming, it is more important than ever to cover the rising energy demand in a clean sustainable way. In the future fuel cells could be a valuable tool for meeting both interests, if hydrogen is obtained from sustainable resources. Thus, research focused on them in recent years.[1-3] To quote the CEO of Shell Hydrogen, Don Huberts, using nearly the same words as Sheikh Zaki Yamani, the former oil minister of Saudi Arabia, "The Stone Age did not end because we ran out of stones, and the oil age will not end because we run out of oil." Thus, maybe hydrogen is going to replace oil and society will experience a dramatic change to a hydrogen economy in the 21<sup>st</sup> century.[4, 5]

Solid fuel cells have some main advantages over other fuel cells types. Due to internal reforming, not only hydrogen can be used as fuel, but also hydrocarbons such as methane, methanol and ethanol. Moreover, it is one of the most efficient fuel cell type, since combination of electrical and heat applications are possible.[6, 7]

Nevertheless, improvements are necessary, there are still some technical issues. The costs have to be decreased and durability enhanced. State of the art SOFCs operate in a temperature range of 700 °C - 1000 °C, which makes great demands on the used materials. The composition of the different elements is very complex and many factors have to be considered such as the thermal expansion coefficients. Due to incompatible materials with different temperature expansion coefficients, strain can be introduced into the cells when heated. Strain can deform, even destroy the SOFCs. Another issue is that these high temperatures demand a high resilience of the interconnects. Since they are located between two cells, they must withstand both oxidizing and reducing atmospheres over a decent time. Nowadays mainly stainless steel is in use as material for such interconnects. Due to these and more problems, significant effort was put into the investigation of intermediate-temperature solid oxide fuel cells. Where the operation temperature range is lowered to around 500 °C - 700 °C.[7]

In intermediate-temperature SOFCs new concerns occurred, the limited conductivity of the electrolyte (yttria stabilized zirconia) and the slow oxygen reduction kinetics at the cathode. Especially the slow reduction kinetics is responsible for most of the resistive losses and limits



the efficiency.[8-10] Thus, the focus of this thesis is the characterization of a possible high activity cathode material, namely  $\text{La}_2\text{CoMnO}_{6-\delta}$  (LCM).

To understand why LCM is an interesting electrode candidate, formerly used or investigated cathode materials should be discussed. In high temperature fuel cells, Sr-doped  $\text{LaMnO}_3$  (LSM) is widely used. At around 1000 °C it has a high electronic conductivity, is compatible with diverse electrolytes, is stable under the present conditions, has acceptable oxygen reduction kinetics, an outstanding long-term performance stability and low overpotential.[6, 11] However, at 500 °C the polarization resistance rises quickly. Due to its low ionic conductivity and the limitation of oxygen reduction to the triple phase boundary, LSM cannot be used in intermediate-temperature SOFCs.[6]

Another investigated promising material is Sr-doped lanthanum ferrite (LSF). It has high electrical and ionic conductivity in the required temperature range and the thermal expansion coefficient is in the same range as YSZ. Cobalt containing LSF (LSCF) is an excellent mixed ionic electronic conductor, but its thermal expansion coefficient is too high. Moreover, it reacts with the electrolyte, hence a barrier layer is needed.[6]

Further oxides with perovskite structure were investigated, for example Sr-doped lanthanum cobaltite (LSC). It possesses excellent ionic and electrical conductivity; however, its thermal expansion coefficient is too high for an application as cathode material in SOFCs. Moreover, under the described conditions its stability is not good enough, it reacts with YSZ forming a resistive interlayer and Sr segregates at the surface.[8, 12]

Considering the properties of the reported materials the intention behind the investigation of LCM was to find a material, which combines the positive features of LSM and LSC. Exhibiting high electronic and ionic conductivity in a temperature range of 500 °C and 700 °C, with great long-term stability under oxidizing conditions and a similar thermal expansion coefficient as YSZ. Furthermore, the effects of the variation of deposition parameters and doping of LCM with known hole dopants for perovskites such as Sr and Ca, was of great interest.

Most studies on semiconducting LCM were made regarding its magnetic properties (especially the ferromagnetic insulating properties, Curie temperature, the zero-field-cooled and field cooled magnetization) and structure.[13-17] Polarized Raman spectroscopy and neutron diffraction can be used to distinguish between the B-site ordered double perovskite and the disordered perovskite, respective ordering can be verified with these methods.[18-22] When ordered former in the disordered structure type forbidden vibrations occur and can be observed via

Raman.[18, 22] Regarding the structure, thin film deposition under high  $p(\text{O}_2)$  (above 200 mTorr) lead to the double perovskite.[13, 23]

Conductivity measurements of the system  $\text{La}_{0.6}\text{Ca}_{0.4}\text{Mn}_{1-x}\text{Co}_x\text{O}_{3-1}$  with  $x = 0.1 - 1.0$  can be found in literature.[24] However, conductivity of non-doped LCM has not been studied intensively at elevated temperatures so far. Nevertheless a first-principles study suggested that LCM is a promising candidate as cathode in SOFCs.[25] On the other hand, in 1996 Jonker reported that in  $\text{LaMn}_{1-x}\text{Co}_x\text{O}_3$  the maximum resistivity at room temperature is obtained if  $x = 0.5$  and the minimal if  $x = 0.9$ . [26]

Ca and Sr-doped LCM is known from literature as well, the structure of the A-site doped perovskite was determined by XRD-measurements and the magnetic properties were studied.[27] The semiconductors  $\text{La}_{2-x}\text{Sr}_x\text{CoMnO}_6$  ( $0 < x < 1$ ) were investigated and Sr was identified to be a hole introducing p-dopant in these double perovskites. Raman spectra and the temperature and frequency dependent susceptibility was recorded.[28] Moreover Souza et al. (1998) investigated the oxygen diffusion in  $\text{La}_{1-x}\text{Sr}_x\text{Mn}_{1-y}\text{Co}_y\text{O}_{3+\delta}$  by performing isotope exchange experiments and ToF-SIMS depth profiling.[29]

For determination of the mentioned properties and to unveil the nature of oxygen reduction on LCM, model systems have to be installed. Therefore, epitaxial thin films on single crystals and microelectrodes were produced, even though in real fuel cells cathodes are porous. The available tools to study the materials properties were van der Pauw measurements.  $^{18}\text{O}_2$  exchange experiments with subsequent ToF-SIMS ion depth profiling were performed. Van der Pauw measurements are widely used to determine the electrical conductivity of arbitrary shaped samples.[30-34] Isotope depth profiles give a direct possibility to estimate oxygen mass transport, thus a combination of isotope exchange experiments and ToF-SIMS was applied.[35]. Oxygen exchange rate in LCM was measured by using impedance spectroscopy.

## 2. Theoretical Background

### 2.1 Solid Oxide Fuel Cells (SOFCs)

In solid oxide fuel cells, the reaction of a fuel and oxygen is used to produce electricity. Thereby the fuel ( $H_2$  or hydrocarbons) is fed to the anode and oxygen to the cathode side. On the anodic side, the compounds are oxidized forming water and  $CO_2$  if hydrocarbons are used. On the cathodic side, oxygen is reduced and  $O^{2-}$  ions travel through the electrolyte to the anode.[36] In return, electrons move from the anode to the cathode and thereby electrical loads can be operated. The basic reactions and a schematic of such fuel cells with  $H_2$  as fuel are shown below in Figure 1 and Equations 1-3.

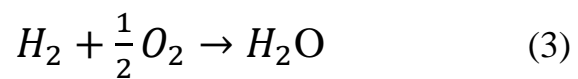
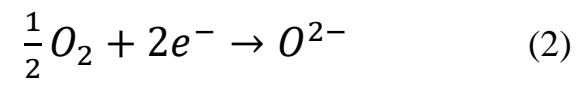
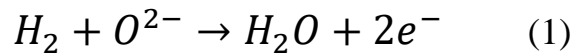
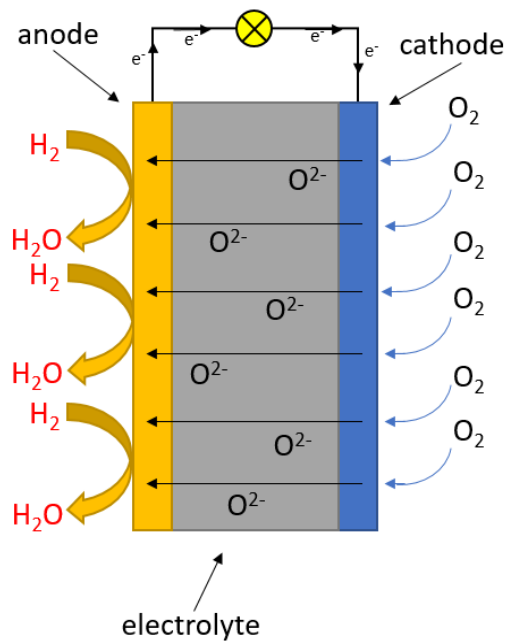


Figure 1: Schematic of an operating solid oxide fuel cell

The electrodes are porous, for anodes usually YSZ cermet is used, while the cathode consists out of strontium-doped lanthanum manganite (LSM), strontium-doped lanthanum cobaltite (LSC) or strontium-doped lanthanum cobalt ferrite (LSCF) and for the dense electrolyte oxide ion conducting yttria-stabilized zirconia (YSZ) are most common.[6] The operating temperature of SOFCs varies between 700 °C and 1000 °C and a wide range of fuels can be used.[36]

Its conversion efficiency does not underlie the Carnot limitation, it converts chemical energy directly to electrical energy.[37] The reversible efficiency of fuel cells is described in Equation 4, it is the ratio between the Gibbs enthalpy and the reaction enthalpy.[38, 39]

$$\eta = \frac{\Delta G_f}{\Delta H_f} = 1 - \frac{T^* \Delta S_f}{\Delta H_f} \quad (4)$$

$\Delta G_f$  .... Gibbs energy change of the reaction [kJ K/mol]

$\eta$  ..... cell efficiency [/]

T ..... temperature [K]

$\Delta S_f$  ... entropy change of the reaction [kJ/mol]

$\Delta H_f$  ... enthalpy change of the reaction [kJ K/mol]

Considering Equation 4 for hydrogen, the lower the operating temperature the higher the efficiency.[2] For methane however, the reversible efficiency is rather independent of temperature. The cost of the ceramic compounds, stability issues and the increased rate of interfacial reaction between the ceramic layers are still reasons, why intermediate temperature SOFC are in focus of research (working temperature 500 °C - 700 °C). [40] However, at lower temperatures a very conductive electrolyte and an active cathode is needed.[41] Most of the resistive losses arise from slow kinetics at the cathodic side, hence new cathode materials are under investigation such as the double perovskite  $\text{La}_2\text{CoMnO}_{6-\delta}$ . [8-10]

## 2.2 Perovskites

Perovskites are named after the mineral  $\text{CaTiO}_3$ , they have the structure of  $\text{ABX}_3$ . A and B are cations of different size, whereby the A ion is the larger one. In the thesis, just oxygen ions are discussed as anions, hence the X is replaced by an O. Therefore, the discussed structures have the formula  $\text{ABO}_3$ , respectively if the B-site is ordered  $\text{A}_2\text{B}'\text{B}''\text{O}_6$ .

B-site ordered perovskites are called double perovskites. The A-site cations in the middle of a unit cell are coordinated by 12 oxygen ions, while the B-site ions are located at the corners, in the middle of an octahedral oxygen cavity. The structure is shown in Figure 2. For stability reasons a tolerance factor (introduced by Goldschmidt) between 0.75 and 1.1 is required.[12] This geometric factor is defined in the following equation:

$$t = \frac{r_A + r_O}{\sqrt{2}(r_B + r_O)} \quad (5)$$

t.... tolerance factor [/]

r.... radii of the A, B and O ions [Å]

The calculation is only an estimation, due to the many factors the ionic radii are affected by, such as distortion, partial occupancy of cations, covalence, metallic character and spin state.[42] When Equation 5 is applied Goldschmidt factors between  $t = 0.95$  and  $1.00$  are obtained for the investigated compounds. (Shannon radii used as effective ionic radii). The used radii are based on  $O^{2-}$  ionic radius =  $1.40 \text{ \AA}$ . [43] The Goldschmidt factors are all in the stable perovskite range, nevertheless none of the investigated substances has a cubic structure. They are either monoclinic (nearly orthorhombic), rhombohedral or orthorhombic and therefore must have a factor between  $0.7$  and  $0.9$ . Since  $Ca^{2+}$  and  $Sr^{2+}$  ions are comparatively big, when  $La_2CoMnO_{6-\delta}$  is doped with them, they go to the A-site and lead mainly to an increase of the hole concentration, which is discussed in chapter 2.5.

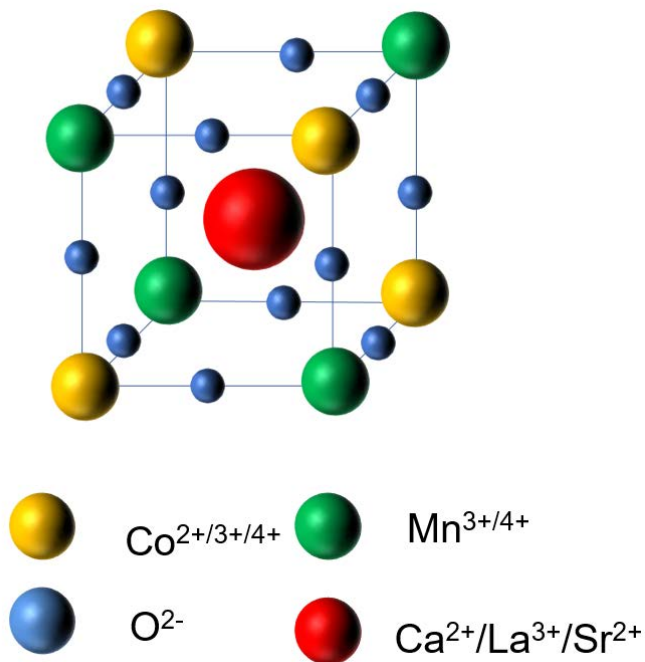


Figure 2: Perovskite structure

### 2.3 Mixed Ionic-Electronic Conductors (MIEC)

Wagner described transport processes of electrons and ions in the same material in 1975, he created the foundation of MIECs theory.[44, 45]

Mixed ionic-electronic conductors are both ionic conductive and electronic conductive, hence they are interesting candidates for cathode materials in SOFCs.[12, 46, 47] The oxygen reduction reaction of only electronically conductive cathodes is limited to the triple phase boundary, whereas in MIECs the reaction and incorporation of oxygen can take place at the whole surface of the porous electrode. Subsequently the resulting oxygen ions migrate through the cathode to the electrolyte.[48, 49] The difference of the two described reaction paths are shown in Figure 3 and Figure 4. The electrolyte surface path is a third option of oxygen reduction, but it is not pictured in the following two graphs.

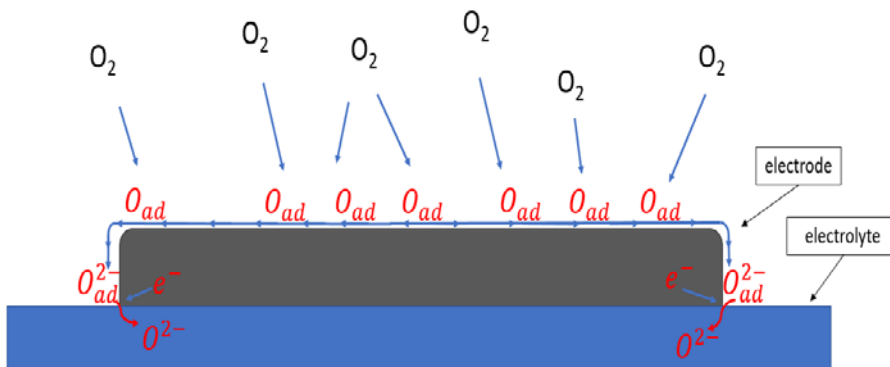


Figure 3: Triple phase reduction of oxygen, only electronically conductive electrode

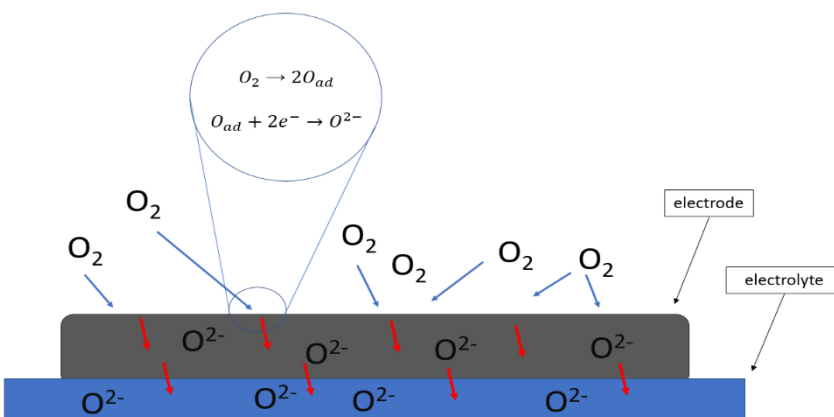


Figure 4: Volume (bulk) path of the oxygen reduction reaction, MIEC as electrode

Recently research has focused on transition metal oxides perovskites and perovskite-related structures. However, most of these materials are mainly electronically conductive and only few show a high transport number of oxide ions. Moreover, often conductivity or the reduction mechanism depends on temperature,  $p(\text{O}_2)$  and/or bias. [48, 50] LSM is an excellent example, in 2015 Huber et al. [50] showed, that the oxygen reduction and incorporation in the electrode tend to switch from mainly triple phase boundary surface path at low temperatures to a dominating volume path under a cathodic bias and at elevated temperatures (above 700 °C). Thereby the bias enhances the ionic conductivity of LSM. [50]

Cobaltites are very good MIEC materials, since Co is more difficult to oxidize to  $\text{Co}^{4+}$ , compared to Mn, which favors the formation of oxygen vacancies. A disproportionation reaction and Sr A-site doping often leads to a mixture of  $\text{Co}^{3+}/\text{Co}^{4+}$  ions, which enhances electrical conductivity, due to an increased hole concentration (for example doping of  $\text{LaCoO}_3$ ). [48] Therefore the oxygen reduction of many cobaltites like strontium doped lanthanum cobaltite (LSC) and strontium doped lanthanum cobalt ferrite take place via the described bulk path.[51]

The conductivity in mixed ion conductors can be described by the following equations, as mentioned it is a combination of the conductivities of the contributing species.[52]

$$\sigma_{ges} = \sigma_{cation} + \sigma_{anion} + \sigma_{electrons} + \sigma_{holes} \quad (6)$$

$$\sigma_i = c_i * q_i * \mu_i \quad (7)$$

$\sigma$  .... conductivity [S/cm]

$c_i$  .... concentration of the charge carrier [ $\text{cm}^{-3}$ ]

$q_i$  .... charge of each species [C]

$\mu_i$  .... mobility of the species [ $\text{cm}^2/\text{s} \cdot \text{V}$ ]

## 2.4 $\text{La}_2\text{CoMnO}_{6-\delta}$ (LCM)

In recent years LCM has been extensively investigated, due to its ferromagnetic insulating properties, even at room temperature.[53] Thereby B-site ordering has a massive impact on its physical properties.[15] When ordered, the Co and Mn cations in the octahedral cavities form a rock salt structure, since they are arranged alternately in the three spatial directions.[16]

Ordering leads to the formation of  $\text{Co}^{2+}/\text{Mn}^{4+}$  pairs, formed out of  $\text{Co}^{3+}/\text{Mn}^{3+}$  and therefore leads to  $180^\circ$ -superexchange interactions, resulting in a saturation magnetization of ca.  $6 \mu_{\text{B}}/\text{f.u.}$ . Moreover, the Curie-temperature is increased to 225 K, while disordered phases possess a lower saturation magnetization and a Curie Temperature of 150 K.[23]

Not only the magnetic properties change, the structural as well. A phase transition from orthorhombic to monoclinic is driven by B-site ordering.[15, 16, 18] In general, two transitions of the double perovskite can be observed, the first is an electrical at around 400 K and a structural transition from monoclinic to rhombohedral at 600 K.[54]

Due to those investigations on LCM, studies for its applicability as cathode material in intermediate-temperature SOFCs were made.[25] In 2014 Yuan et al. [25] did first-principle calculations on ordered and non-ordered LCM. The following trend for the oxygen vacancy formation energy was predicted:  $\text{Co}^{2+} - \text{O}^* - \text{Mn}^{4+}$  (ca. 3.3 eV) >  $\text{Co}^{2+} - \text{O}^* - \text{Co}^{3+}$  (ca. 2.73 eV) >  $\text{Mn}^{3+} - \text{O}^* - \text{Mn}^{4+}$  (ca. 2.20 eV). Considering these energy values, oxygen vacancies form most likely at anitsite defects. Thus, disordered LCM should have an enhanced oxygen ionic conductivity. Moreover due to the lower repulsion between two Mn next to an oxygen vacancy then between two Co, the formation of a vacancy between Mn ions is favored and the vacancy itself more stable. [25].

Since B-site ordering has a significant impact on the properties of LCM, it is important for the measurements to obtain either ordered or nonordered thin films. The fabrication parameters determine whether a perovskite or a double perovskite is produced. For ordered structures high growth temperatures and a high  $p(\text{O}_2)$  are required.[15, 23] At a growth temperature of  $800^\circ\text{C}$ . the lattice parameter  $b$  starts to decrease above 200 mTorr background pressure, above 600 mTorr it saturates.[15] Hence the transition from disordered to ordered thin films can be described through the lattice parameter  $b$  or a combination of growth temperature and oxygen partial pressure.

Due to the formation of  $\text{Mn}^{4+}$  and  $\text{Co}^{2+}$ , at room temperature a maximum resistivity is reported in  $\text{La}_2\text{Mn}_{1-x}\text{Co}_x\text{O}_6$  for a Co/Mn ratio of 1:1.[17, 26]

P-type doping of LSM with Ca or Sr leads to  $\text{La}_{0.7}\text{Ca}_{0.3}\text{Mn}_{0.5}\text{Co}_{0.5}\text{O}_3$  with a monoclinic unit cell and to  $\text{La}_{0.8}\text{Sr}_{0.2}\text{Mn}_{0.5}\text{Co}_{0.5}\text{O}_3$ , which possesses a rhombohedral structure. The long-range ferromagnetism is destroyed like in LCM. In the Sr-doped LCM Gamari-Seale et al. [27] assume that the introduced holes lead most likely to  $\text{Co}^{4+}$ , consequently a mixture of  $\text{Co}^{2+}$ ,  $\text{Co}^{4+}$  and  $\text{Mn}^{4+}$  is present in the described compound. Moreover, it is predicted that Ca doping induce



holes as well.[27] On the other hand, in 2008 Vashook et al. [24] could observe neither  $\text{Co}^{4+}$  nor  $\text{Mn}^{2+}$  ions in the system  $\text{La}_{0.6}\text{Ca}_{0.4}\text{Mn}_{1-x}\text{Co}_x\text{O}_{3-\delta}$ . Only mixtures of  $\text{Co}^{2+}/\text{Co}^{3+}$  and  $\text{Mn}^{3+}/\text{Mn}^{4+}$  were found to be present.[24]

## 2.5 Defects and Diffusion in Solids

Defects play a significant role in oxygen reduction reactions and in diffusion processes of oxygen through crystals.[52, 55] They can be categorized in zero dimension-point defects, such as vacancies and self interstitials, one-dimensional defects (dislocations), two-dimensional defects (external and internal surfaces) and three-dimensional defects (point defect clusters).[56]

Point defects appear during crystal growth and are so called native defects. These intrinsic defects exist in a thermodynamic equilibrium as well. Their formation is temperature dependent and can be described by Gibbs energy. The following equation quantify the change of Gibbs energy for the formation of an isolated vacancy. One assumption was made, the change of entropy comes just from the change of the configurational entropy.[52, 56, 57]

$$\Delta G_V = \Delta H_V - T * \Delta S_V \quad (8)$$

$$\Delta S_V = S_{conf} = k_B \ln W \quad (9)$$

$$W = \frac{N!}{(N-n)!*n!} \quad (10)$$

$\Delta G_V$  ..... Gibbs energy of vacancy formation [J]

$\Delta H_V$  .... vacancy formation enthalpy [J]

T ..... temperature [K]

$\Delta S_V$ ..... vacancy formation entropy [J/K]

$S_{conf}$  ..... configurational entropy [J/K]

$k_B$  ..... Boltzmann constant [J/K]

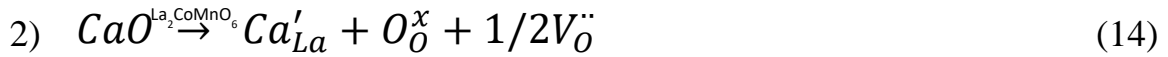
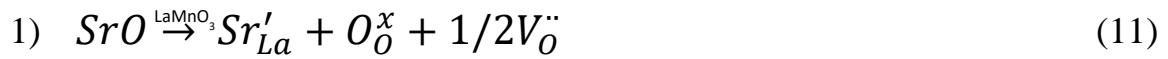
W ..... distinguishable ways of distributing n [/]

n ..... number of vacancies [/]

N ..... number of lattice sites [/]

Since introduced impurities increase the entropy in a formerly perfect crystal, Gibbs energy is decreased. The formation enthalpy of vacancies stays constant and is nearly temperature independent. Consequently, Gibbs energy has a local minimum at an equilibrium number of point defects for a given temperature. It rises again at the point when additional defects are not able to sufficiently increase the entropy in the crystal any more. Then more energy is needed to form a defect than disorder gains. The described native defects in ionic crystals are either due to Schottky defects, with a cation vacancy and an anion vacancy, or Frenkel disorder, which is a combination of a vacancy and an interstitial ion.[52, 56]

Over and above doping has a massive impact on point defects, it can introduce either ionic or electronic defects. As examples, Sr-doping of LaMnO<sub>3</sub> and Ca-doping of ordered/disordered La<sub>2</sub>CoMnO<sub>6-δ</sub> are given. In these examples holes and/or oxygen vacancies are formed.



Through Sr-doping most likely holes form in LaMnO<sub>3</sub>, Sr is a p-dopant and enhances the electrical conductivity of LaMnO<sub>3</sub>. The holes are localized on former Mn<sup>3+</sup>-sites, a polaron is formed, Mn<sup>3+</sup> becomes Mn<sup>4+</sup>. Sr doping of LaMnO<sub>3</sub> is described in the Equations 11-13.

In LCM either oxygen vacancies,  $\text{Co}^{3+}$  or a mixture of  $\text{Co}^{3+}$  and  $\text{Mn}^{4+}$  can be formed (Equations 14-17). The resulting oxygen states of the B-site cations depends on the ordering respectively disordering of the crystal structure. In a perfect double perovskite  $\text{Co}^{2+}$  becomes  $\text{Co}^{3+}$  and  $\text{Mn}^{4+}$  remains in its oxidation state (Equation 16 + 17). In a disordered LCM, where Co occupies some Mn-sites and vice versa,  $\text{Co}^{3+}$  remains on the Mn-sites and  $\text{Mn}^{4+}$  is additionally formed on the Co-sites. In compounds with the composition  $\text{La}_{0.6}\text{Ca}_{0.4}\text{Mn}_{1-x}\text{Co}_x\text{O}_{3-\delta}$ ,  $\text{Co}^{4+}$  and  $\text{Mn}^{2+}$  are not present. Moreover, it is suggested that  $\text{Mn}^{4+}$  acts as hole and is responsible for a p-type conductivity whereas  $\text{Co}^{2+}$  can be seen as ion with a localized electron, and therefore n-type conducting.[24]

On the other hand, dislocations are never in thermodynamic equilibrium with their surroundings. These linear defects are extrinsic, they are surrounded by a strain field. There are two types of dislocations in edge dislocations, screw dislocations and a mixture of both.[56]

As mentioned, defects play a vital role in diffusion as well, in fact vacancies are mandatory in many oxides for ion transport.[48] In general, a diffusion process can be described through the first and second Fick's laws, given in the equations below. They are the basis of the random walk theory, which is a simplified model where diffusion consists of uncorrelated jumps. Atoms jumping from a site A to a site B have to overcome a saddle point, which needs a decent amount of energy. Moreover, for describing the jump frequency an additional parameter is needed, the attempt frequency. Typical values are in the order of  $10^{12} \text{ s}^{-1}$ , which is in the range of the Debye frequency.[52, 56]

$$J = -D * \frac{dc}{dx} \quad (18)$$

$$\frac{dc}{dt} = D * \frac{d^2c}{dx^2} \quad (19)$$

J ..... diffusion flux [ $\text{mol}/\text{m}^2 \text{ s}$ ]

D .... diffusion coefficient [ $\text{m}^2/\text{s}$ ]

c ..... concentration [ $\text{mol}/\text{m}^3$ ]

t ..... time [s]

x ..... distance [m]

The diffusion coefficient introduced by Equation 18 and Equation 19 has an Arrhenius dependency on temperature. Moreover, the diffusion is related to the pressure as well, due to the activation volume. This pressure dependence is negligible at ambient pressures and an often-suppressed factor. It describes the increase of the lattice volume during the migration of an atom, when the moving species are located at the saddle point.[52, 58]

Another often ignored fact is the different diffusivity of two isotopes, since the attempt frequency is related to the harmonic oscillation of the atom and therefore connected to mass. In most cases the difference is negligible, nevertheless it should always be kept in mind.[52]

Diffusion as such can be divided into several types, the most important one is the vacancy diffusion. Thereby an atom jumps into an adjacent vacancy, the vacancy is the moving species through the lattice. Another mechanism is the interstitial mechanism, it describes a small dissolved atom moving from an interstitial site to another interstitial site. A description of the collective, the divacancy and the interstitially mechanism is given by Helmut Mehrer in his book Diffusion in Solid Fundamentals, Methods, Materials, Diffusion-Controlled Processes, published in 2007.[52, 56, 57]

Thin films may exhibit grain boundaries and/or dislocations. These can be high diffusivity paths and often play key roles, especially grain boundary diffusion.[59] For example in thin films with grain boundaries the diffusion process can consist out of the bulk diffusion, a diffusion along the boundaries and a lateral diffusion from the boundaries into the bulk. The diffusion process along the grain boundaries of oxides is not fully understood. It is believed that the formation energy of point defects in the boundaries is lower compared to the energy needed in the bulk and that a vacancy mechanism is responsible for the fast diffusion. Moreover, collective motion might play a vital part as well. J.C. Fisher and R.T.P. Whipple laid the mathematical fundamentals of the proposed model.[52, 60-62]

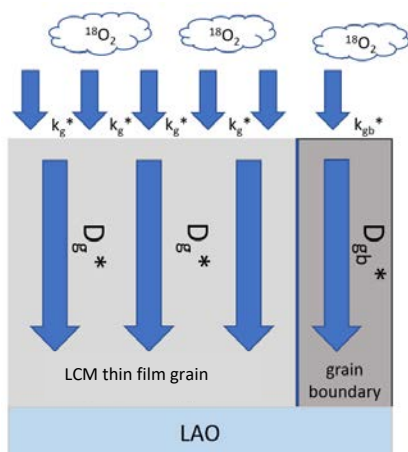


Figure 5: Model of grain boundary diffusion

## 2.6 Pulsed Laser Deposition (PLD)

The most effective technique for the growth of complex crystalline oxides is pulsed laser deposition (PLD). It is a physical vapor deposition process and is carried out in systems where defined atmospheres can be established. With this technique stoichiometrically ablated material can be transported from a target to an opposing substrate.[63, 64] Thereby the target is hit by an UV-laser beam, whose energy is absorbed only by a small volume of the target. Subsequently target material is vaporized, a plasma plume is established and material deposited on the substrate, which is positioned on a heating coil. The ablation itself has a nonequilibrium nature. The properties of the produced thin film can be tailored by varying deposition parameters such as temperature, laser pulse rate and oxygen pressure. The so-called background pressure can have two functions, firstly it can react with the ablated material and can be required for the formation of the desired phase, secondly it can be used to impact the kinetic energy of the ablated species.[63] The volume of the plasma plume is reduced at high background pressures, due to the interaction with the gas in the PLD-chamber. [63, 65] The deposition process is sketched in Figure 6.

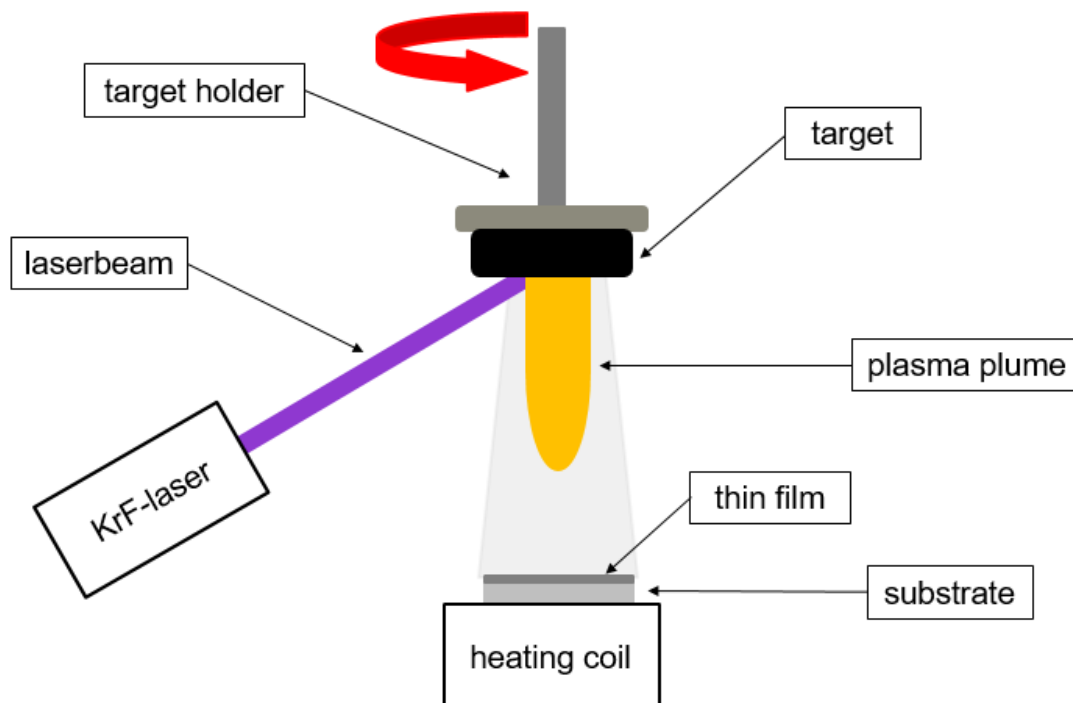


Figure 6: Pulsed Laser Deposition (PLD)

## 2.7 Van der Pauw Measurements

### 2.7.1 Basics of the Method

The method is widely used to determine the specific resistivity of thin, flat samples of arbitrary shape.[30, 33, 66] Thereby a specimen is contacted at the edges by four electrodes A, B, C and D. Considering the following equations, the electrical resistivity can be calculated.[30, 32, 66]

$$\rho = \frac{\pi * d}{\ln 2} * \frac{(R_{AB,CD} + R_{BC,DA})}{2} * f \quad (20)$$

$$R_{AB,CD} = \frac{U_{CD}}{I_{AB}} \quad R_{BC,DA} = \frac{U_{DA}}{I_{BC}} \quad (21+22)$$

$\rho$  ..... resistivity [ $\Omega * \text{cm}$ ]

$d$  ..... sample thickness [ $\text{cm}$ ]

$f$  ..... formfactor [1]

$R_{AB,CD}, R_{BC,DA}$  ... resistances [ $\Omega$ ]

For  $R_{AB,CD}$  the current between A B and the voltage between C D is measured.  $R_{BC,DA}$  is determined by following the same procedure, measuring the current between B C and the voltage between D A. Since the shape of any sample can be arbitrary, a formfactor  $f$  as function of  $R_{AB,CD} / R_{BC,DA}$  is introduced. An approximation of  $f$  can be obtained from Equation 23.[30]

$$f \approx 1 - \left( \frac{R_{AB,CD} - R_{BC,DA}}{R_{AB,CD} + R_{BC,DA}} \right)^2 * \frac{\ln 2}{2} - \left( \frac{R_{AB,CD} - R_{BC,DA}}{R_{AB,CD} + R_{BC,DA}} \right)^4 * \left( \frac{(\ln 2)^2}{4} - \frac{(\ln 2)^3}{12} \right) \quad (23)$$

For receiving convincing reproducible results, the specimens have to meet some requirements. The samples must be flat of homogeneous thickness and the thickness should be sufficiently smaller than the lateral extension. The electrodes must be well conducting, placed at the edges of the sample and as small as possible (ideally point like). At the surface, there should not be any cracks or isolated holes.[30, 33]

Due to these preconditions, a lot of possible error sources arise, such as the placement of the contacts and the sample thickness. In 2005 Kasl et al. determined the limiting thickness of a

circular specimen, with contacts on the edge of the surface, to be about half the sample's diameter. The limiting thickness can be extended, if the contacts are placed across the edges, since a more 2 D like current distribution is achieved.[31]

## 2.7.2 Conductivity Activation Energy and its Calculation from Arrhenius Plots

In most mixed ionic electronic conductors, the conductivity increases exponentially with rising temperature, an Arrhenius type dependency is present. Thus, an increased temperature increases the charge carrier concentration and/or their mobility. The connection between conductivity and mobility of the charge carriers is given by following equation derived from Equation 5.

$$\sigma = z * \mu * n * e_0 \quad (24)$$

$\mu$  ..... mobility of ions [ $\text{cm}^2/\text{s}$ ]

$\sigma$  ..... conductivity [ $\text{S}/\text{cm}$ ]

$e_0$  .... elementary charge [ $\text{eV}$ ]

$n$  ..... concentration of charge carriers [ $\text{cm}^{-3}$ ]

$z$  ..... charge of the conducting species [/]

Furthermore, the mobility itself can be described by the Nernst-Einstein relation. It is dependent on the diffusion coefficient, which is the reason for the discussed Arrhenius type nature of conductivity.[52]

$$\mu = \frac{z * e_0 * D}{k_B * T} \quad D = D_0 * e^{\frac{-E_a}{k_B * T}} \quad (25+26)$$

$D$  .... diffusion coefficient [ $\text{cm}^2/\text{s}$ ]

$k_B$  ... Boltzmann constant [ $\text{eV}$ ]

$T$  .... temperature [ $\text{K}$ ]

$E_a$  ... activation energy [ $\text{eV}$ ]

The activation energy in the Arrhenius equation describes the energy barrier, which must be overcome for the transport of localized charge carriers. Combining the Equations 24-26 the conductivity is given by:

$$\sigma = \frac{z^2 n e_0^2 D_0}{k_B T} * e^{\frac{-E_a}{k_B T}} \quad (27)$$

Finally, the conductivity multiplied by temperature is plotted against the inverse temperature. As a result, the negative activation energy of the mobility can be calculated by multiplying the slope  $m$  of the linear fit function of the plotted data points by the Boltzmann constant, provided the concentration itself as temperature independent.

$$\ln(\sigma * T) = \ln(A_T) - \frac{E_a}{k_B T} \quad A_T = \frac{z^2 * n * e_0^2}{k_B} \quad (28+29)$$

$$-E_a = m * k_B \quad (30)$$



## 3. Experimental Part

### 3.1 Sample Preparation using a Pechini-type Method

PLD targets were produced by a Pechini-type method.[67, 68] For the LCM ( $\text{La}_2\text{CoMnO}_6$ ),  $\text{LaCo}_{0.4}\text{Mn}_{0.6}\text{O}_3$  and  $\text{LaCo}_{0.6}\text{Mn}_{0.4}\text{O}_3$  samples  $\text{Co}_3\text{O}_4$  (99.5 Sigma Aldrich, Missouri),  $\text{La}_2\text{O}_3$  (99.999% Sigma Aldrich, Missouri) and  $\text{MnCO}_3$  ( $\geq 99.9$  % Sigma Aldrich, Missouri) were weighed out according to the stoichiometric values to receive 5 g target material. For the LCCM ( $\text{La}_{0.7}\text{Ca}_{0.3}\text{Co}_{0.5}\text{Mn}_{0.5}\text{O}_3$ ) sample additionally  $\text{CaCO}_3$  (99.995 % Sigma Aldrich, Missouri) and for the LSCM ( $\text{La}_{0.8}\text{Sr}_{0.2}\text{Co}_{0.5}\text{Mn}_{0.5}\text{O}_3$ ) target  $\text{SrCO}_3$  (99.995 % Sigma Aldrich, Missouri) were needed. The components were dissolved in 10 ml distillation purified 70 %  $\text{HNO}_3$  ( $\geq 99.999$  % Sigma Aldrich, Missouri) and 10 to 15 ml double dist.  $\text{H}_2\text{O}$ .  $\text{Co}_3\text{O}_4$  did not dissolve under these conditions, a complex builder was needed. After stirring for 30 min, citric acid monohydrate ( $\geq 99.9998$  % Fluka, Switzerland) in excess of 10 % assuming a 1: 1 reaction with the cations was added to the reaction mixture. The obtained solution was heated and the water was removed from the beaker till the reaction mixture turned into a dark red/ violet viscous mass. Further heating lead to the evolution of  $\text{NO}_x$  gas and a black foam was received. For a complete combustion of the citric acid and decomposition of the nitric compounds to  $\text{NO}_x$  the foam was burned by using a tripod and a Bunsen burner.

The received black powder was grained and transferred into a  $\text{Al}_2\text{O}_3$  crucible and calcinated following the protocol shown in Figure 7. After the calcination step the powder was filled in self-made silicon molds, isostatically pressed at 300 bar for 2 min and sintered following the protocol shown in Figure 8. All calcination and sintering steps were performed in a CWF1300 (Carbolite, Germany) furnace.

To check the purity of each of the finalized PLD targets XRD measurements were done. In case of multiple phases in a produced sample, it was sintered a second time. Finally, the obtained pellets were glued to steel target holders with 100 parts Duralco 4700 HT Resin (Cotronics, New York) plus 28 parts Duralco 4700 HT Hardener (Cotronics, New York). To harden the resin, the glued components were heated to 120 °C kept there for 4<sup>00</sup> h, then to 175 °C holding the temperature for 1<sup>30</sup> h and in a last step to 230 °C for 16<sup>00</sup> h.

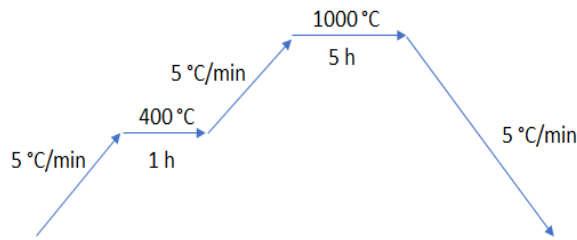


Figure 7: Calcination program

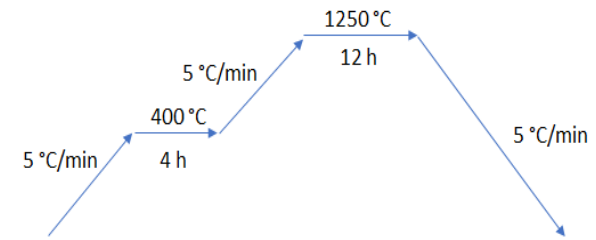


Figure 8: Sintering program

### 3.2 Pulsed Laser Deposition

Thin films were prepared by pulsed laser deposition (PLD on YSZ (001), LAO (001) and STO (001) single crystals. The PLD chamber was evacuated to ca.  $4 \cdot 10^{-5}$  mbar pressure and a specific oxygen pressure was established and the single crystals were heated with 80 % or 90 % heating power, leading to a substrate temperature between 645 °C and 675 °C, depending on the oxygen partial pressure during film growth. The temperature was monitored during the depositions with a Heitronics KT19.99 (HEITRONICS Infrarot Messtechnik GmbH, Germany) pyrometer. The distance between the target and the single crystals was kept constant at 5.7 cm for all depositions. A KrF (248 nm) excimer laser (Lambda COMPexPro 205F, California) was used to ablate the target materials. The beam energy per pulse was also kept constant for all experiments at 400 mJ. STO and LAO substrates are polished on one side only and on this side one thin film was deposited. The YSZ crystals were polished on both sides and two thin films were deposited one on each side. The film which was produced secondly, was then microstructured and the obtained microelectrodes acted as working electrodes in the impedance spectroscopy. The non-structured film acted as counter electrode. An overview of the deposition parameters is given in Table 1.

Table 1: PLD deposition parameters

sample	pressure [mTorr]	deposition time [min]	deposition rate [Hz]	substrate	heating [%]
LCM 05	113	30/15	5	YSZ	80
LCM 06	113	30/30	5	YSZ	80
LCM 07	113	15/15	5	YSZ	80
LCM 13	100	20	1	LAO	90
LCM 15	750	20	1	LAO	90
LCM 18	500	20	1	LAO	90
LCM 19	100	30	5	LAO	90
LCM 20	500	30	5	LAO	90
LCM 21	900	30	5	LAO	90
LCCM 04	30	5	1	LAO	90
LCCM 05	30	15	1	LAO	90

LCCM 06	30	15	1	STO	90
LCCM 07	30	40	1	LAO	90
LCCM 08	30	40	1	STO	90
LCCM 09	30	70	1	LAO	90
LCCM 10	30	70	1	STO	90
LaCo <sub>0.4</sub> Mn <sub>0.6</sub> O <sub>3</sub>	100	30	5	LAO	90
LaCo <sub>0.4</sub> Mn <sub>0.6</sub> O <sub>3</sub>	500	30	5	LAO	90
LaCo <sub>0.4</sub> Mn <sub>0.6</sub> O <sub>3</sub>	900	30	5	LAO	90
LaCo <sub>0.6</sub> Mn <sub>0.4</sub> O <sub>3</sub>	100	30	5	LAO	90
LaCo <sub>0.6</sub> Mn <sub>0.4</sub> O <sub>3</sub>	500	30	5	LAO	90
LaCo <sub>0.6</sub> Mn <sub>0.4</sub> O <sub>3</sub>	900	30	5	LAO	90

### 3.3 Microelectrode Preparation

#### 3.3.1 UV-Lithography

The microelectrodes for the impedance spectroscopy were prepared by UV-lithography and subsequent Ar<sup>+</sup>-ion etching. All steps of the lithography were done in a clean room environment. First the LCM samples were coated with 50 μm of the photoresist ma-N1420 (Micro Resist Techn., Germany) using a KLM Spin-Coater-200 (Schaefer Technologie GmbH, Germany). Afterwards the samples were heated to 100 °C for 2 min., to dry the photoresist. After the alignment of the photomask the samples were illuminated with UV-light for 40 s, using an Ushio USH-350DP 350 Watt mercury short arc lamp (USHIO INC., Japan) to polymerize parts of the photoresist. The samples were placed in a ma-D 533s developer (Micra Resist Techn., Germany) for nearly one min.. To stop the dissolution of the photoresist, which was not illuminated with UV-light, the samples were immersed in dest. H<sub>2</sub>O.

#### 3.3.2 Ar<sup>+</sup> Etching

After the photoresist layer was developed further, the thin films were structured by ion beam etching. The following etching parameters were used: 4 kV extractor current, acceleration voltage 2 kV,  $1,2 \cdot 10^{-4}$  mbar Ar-pressure, between 1.37 mA and 2.28 mA ion current and 80 min etching time. Finally, the remaining photoresists was removed by an acetone bath and the obtained microelectrodes controlled under the microscope. They were circular with nominal diameters between 50 μm and 450 μm.

### 3.4 Atomic Force Microscopy (AFM)

All AFM pictures were taken by Prof. Gernot Friedbacher with a NanoScope V Multimode SPM (Veeco Instruments GmbH, Germany) in tapping mode, at the Institute of Chemical Technologies and Analytics, TU Wien, Getreidemarkt 9, 1040 Vienna.

### 3.5 Transmission Electron Microscopy (TEM)

The TEM images were taken by Wolfgang Wallisch using a FEI Quanta 200 FEG (FEI Technologies Inc., Oregon) with Schottky emitter at the USTEM, Wiedner Hauptstr. 8-10, 1040 Vienna.

### 3.6 Van der Pauw Measurements

Sheet resistivity was measured by van der Pauw method, thereby a self-built measurement setup (Figure 9) from the working group of Prof. Jürgen Fleig at the Institute of Chemical Technologies and Analytics, TU Wien, was used. The working principle is described in section 2.7.1; voltage and temperature were measured by a Keithley 200 multimeter (Keithley Instruments Inc, Cleveland, Ohio) and the current by a Keithley 2410 1100V source meter (Keithley Instruments Inc., Cleveland, Ohio). To establish a constant temperature, a tube oven (Gero SR 70-200/12SO, Carbolite Gero GmbH & Co. KG, Germany) with a Eurotherm temperature controller (Euro Electronic S.r.l., Italy) and for a controlled gas flow of N<sub>2</sub> and O<sub>2</sub> during measurements the mass flow controllers Tylan FC280S (Tylan General Inc., California) and Aera FC7700C (Aera Corp., Texas) were used. The measured current, voltage and temperature data were saved as text file and analyzed with the help of an Excel Macro, written by Andreas Nennung.

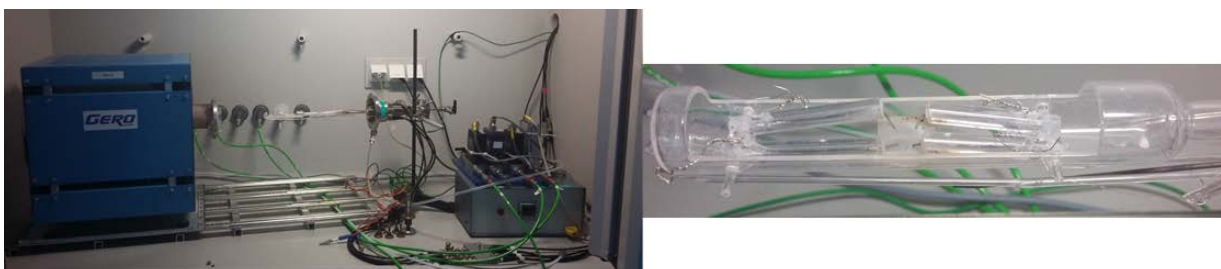


Figure 9: Left: Overview van der Pauw set up; Right: Sample holder with the four Pt-needles

Before measuring, the bulk samples were cut on a Struers Secotom-10 (Struers Inc., Ohio) cutting machine, equipped with a 50A20 Al<sub>2</sub>O<sub>3</sub> cutting wheel (Struers Inc., Ohio). After cutting the bulk samples were grinded and polished with SiC foil #500, #1200, #2000 and #4000 (Struers Inc., Ohio). Pt-electrodes for van der Pauw measurements were painted on the edges.

The thin film samples for the van der Pauw measurements were produced by PLD (see chapter 3.2) on non-conducting LaAlO<sub>3</sub> single crystal substrates with an orientation of (001). The substrates were cut from 10x10x0.5 mm<sup>3</sup> single crystals by a diamond cutter and had the dimension of roughly 5x5x0.5 mm<sup>3</sup>. The existing twin structures at the surface are negligible for sheet resistivity determination. In the last step of the sample preparation Pt-electrodes were painted on the edges and the specimens were sintered at 850 °C for two hours in a Carbolite CWF 1300 chamber oven (Carbolite Gero GmbH & Co. KG, Germany).

For the measurement, the thin films and bulk samples were contacted with Pt-needles, which were placed on the painted Pt-electrodes. Since a correction factor is needed for conductivity determination, three to five measurements were carried out each in bottom and top configuration at the lowest temperature of a temperature cycle. Thereby the direction of the electric current was changed only once, thus each measurement needed 38 s. The collection time for one measurement during a temperature cycle varied between 38 s and 118 s (collection time temp. cycle). In all mentioned measurement cycles the first data point was recorded at t = 0 s; to change the current direction, the measurement paused for 1 s. Consequently, during a collection time of 38 s with one change of the current direction 38 data points were recorded, 19 in each direction.

The starting temperature (T<sub>min</sub>), the maximum temperature (T<sub>max</sub>) and the number of steps of the performed temperature cycles were optimized during the thesis. These parameters were not changed during a measurement cycle. In Table 2 an overview of the used samples and measurement parameters is given.

Table 2: Van der Pauw measurement parameters

sample	sample thickness [mm]	atmosphere	Tmin [K]	Tmax [K]	number of measurement points (heating up + cooling down)	collection time temp. cycle [s]	voltage [V]
LSM 20 bulk	0.733 +/- 0.002	air and N <sub>2</sub>	507/509	986/989	21	118	0.1
LCM 1 bulk	0.566 +/- 0.001	air and N <sub>2</sub>	322/294	846/846	23	38	0.01
LCM 2 bulk	1.021 +/- 0.003	air and N <sub>2</sub>	412/412	892/892	23	38	0.1
LCCM bulk	1.337 +/- 0.009	air and N <sub>2</sub>	556/556	843/845	13	38	0.1
LSCM bulk 1	1.294 +/- 0.002	air, O <sub>2</sub> and N <sub>2</sub>	511/461/460	894/848/848	19	38	0.1
LaCo <sub>0.6</sub> Mn <sub>0.4</sub> O <sub>3</sub> bulk	1.153 +/- 0.004	air and N <sub>2</sub>	507/510	986/989	21	118	0.1
LaCo <sub>0.4</sub> Mn <sub>0.6</sub> O <sub>3</sub> bulk	0.893 +/- 0.001	air and N <sub>2</sub>	555/508	986/989	21	118	0.1
sample	sample thickness [nm]	atmosphere	Tmin [K]	Tmax [K]	number of steps (heating up + cooling down)	collection time temp. cycle [s]	voltage [V]
LCM 13 thin film	14	air	504	939	17	38	0.1
LCM 17 thin film	6	air	558	941	17	38	0.1
LCM 18 thin film	11	air	460	941	17	38	0.1
LCM 19 thin film	104	air	508	940	21	38	0.1
LCM 20 thin film	84	air	556	940	17	38	0.1
LCM 21 thin film	47	air	555	940	17	38	0.1
LaCo <sub>0.6</sub> Mn <sub>0.4</sub> O <sub>3</sub> thin films	104/84/47	air and N <sub>2</sub>	506/509/508 510/508/508	987/987/989 800/988/990	21	118	0.1
LaCo <sub>0.4</sub> Mn <sub>0.6</sub> O <sub>3</sub> thin films	104/84/47	air and N <sub>2</sub>	509/507/509 504/510/510	989/988/988 989/990/989	21	118	0.1

### 3.8 X-ray Diffraction (XRD Measurements)

Phase purity of all targets produced by the Peccini-type method were checked by powder XRD measurements, using Bragg-Brentano configuration. A Cu-target was used for X-ray generation. The emitted wavelengths after the monochromator are  $K_{\alpha 1} = 1.540601 \text{ \AA}$  and  $K_{\alpha 2} = 1.54443 \text{ \AA}$ . The measurements were done by a PANalytical XPert Pro MPD ( $\theta$ - $\theta$  diffractometer) (PANalytic B. V., Netherlands) at the X-ray center of TU Wien, Getreidemarkt 9, 1040 Vienna. It uses a X'Celerator semiconductor  $2.1^\circ$  as detector and has a Bragg reflector as monochromator. The distances source to sample and sample to detector are 240 mm each.[69]

For the purity checks the surfaces of the sintered targets were ground and cleaned for 3 to 5 min in an EtOH ultrasonic bath. Subsequently the samples were placed on a piece of plasticine and in a final step, the heights were aligned for the powder XRD measurement.

To determine the cell parameters, pieces of LCM-, LCCM- and LSCM-targets were powdered, mixed with the internal standard  $\text{LaB}_6$  (Standard Reference Material 660b) and placed on Si single crystals cut in (711) direction. After the measurements were done by an Empyrean PANalytical ( $\theta$ - $\theta$  diffractometer) (PANalytic B. V., Netherlands) the obtained diffractograms were corrected with the standard and the cell parameters determined using Rietveld refinement.

All measurements were done under ambient atmosphere, pressure and temperature. The analyses were done in X'Pert HighScore (PANalytical B.V., Netherlands). Rest of the measurement details are given in Table 3.

Table 3: Powder XRD measurement details

sample	step size [ $^\circ$ ]	$2\theta$ range [ $^\circ$ ]	scan step time [s]
LCM purity check	0.002	10.80 – 104.04	69.85
LCM cell parameter determination	0.002	10.02 – 89.79	147.39
LCCM purity check	0.002	5.02 – 99.98	99.70
LCCM cell parameter determination	0.002	16.58 – 89.74	147.39
LSCM purity check	0.002	5.02 – 99.98	99.70
LSCM cell parameter determination	0.002	10.02 – 89.97	147.39
$\text{LaCo}_{0.4}\text{Mn}_{0.6}\text{O}_3$ purity check	0.002	5.02 – 99.98	80.01
$\text{LaCo}_{0.6}\text{Mn}_{0.4}\text{O}_3$ purity check	0.002	5.02 – 99.98	80.01

### 3.9 $^{18}\text{O}$ Gas Exchange and ToF-SIMS Tracer Depth Profiling

For  $^{18}\text{O}$  gas exchange experiments and ToF-SIMS tracer depth profiling many studies can be found, described by Kubicek et al., Gerstl et al. and Holzlechner et al.[9, 70, 71] Considering these, the samples consisting of single crystal substrates STO (001) or LAO (001) ( $5 \times 0.5 \times 0.5 \text{ mm}^3$ ) with deposited layers of LCM or LCCM on the top were put in a quartz tube for the tracer exchange experiments. Afterwards the measurement sword was heated in ambient air to the annealing point. After 2 to 4 hours the tube was evacuated (for nearly 15 min) and filled with  $^{18}\text{O}_2$  enriched gas (97.1 %  $^{18}\text{O}_2$  isotope, Campro Scientific, Germany). In all experiments, the filling process to ca. 200 mbar took 20 s to 30 s and the exchange times were 919 min and 210 min at 600 °C and 575 °C. To stop the tracer exchanges, the tubes were pulled out of the furnace and the samples rapidly cooled down with a cooling rate of  $\sim 60 \text{ K/min}$  under an atmosphere of 200 mbar  $^{18}\text{O}_2$ . [9, 72]

The tracer ion depth profiles were obtained on a TOF.SIMS 5 (ION-TOF, Germany) instrument. The  $70 \times 70 \mu\text{m}^2$  probing areas were scanned using  $512 \times 512$  measuring points. The used  $\text{Bi}^{3+}$  primary ions had an energy of 25 keV and the set-up alignment allowed to measure the natural  $^{18}\text{O}$  isotope concentration with an accuracy of  $0.206 \pm 0.004 \%$  and a beam diameters below 100 nm [71]. ToF-mass spectra were recorded and the thin films ablated with 2 keV  $\text{Cs}^+$  ions ( $\sim 104 \text{ nA}$ ). Following this procedure, tracer ion depth profiles with step sizes of 0.13 to 1.33 nm were received. For charge compensation a low energy electron gun was used.[9] All ToF-SIMS measurements were carried out by Edvinas Navickas at the Institute of Chemical Technologies and Analytics, TU Wien, Getreidemarkt 9, 1040 Vienna. In a last step, the data were fitted by COMSOL Multiphysics® Modeling Software (COMSOL Inc., Germany) to obtain diffusion and surface exchange coefficients. For the fitting, the  $^{18}\text{O}$  concentration in the gas phase was assumed to be constant, since its decrease is negligible.

### 3.10 Impedance Spectroscopy

Impedance spectroscopy were carried out on the samples LCM 05, LCM 06 and LCM 07. These consist of YSZ (001) single crystal substrates and LCM microelectrodes on their top side and a LCM thin film on their bottom side. The measurements of LCM 05 were carried out at the so-called II-Pot, equipped with a FS70Z-S (Mitutoyo, Japan) microscope, Linkam TS 1000 (Linkam Scientific Instruments, UK) furnace and a Novocontrol Alpha-A High Performance Frequency Analyzer (Novocontrol Technologies GmbH & Co. KG, Germany) to measure the impedance at frequencies from  $10^6 \text{ Hz}$  down to  $10^{-2} \text{ Hz}$ . A gold covered steel needle acted as



working electrode contact and a Pt-sheet as counter electrode. Microelectrodes of varied sizes were measured multiple times at three temperatures to calculate activation energies.

The impedance of LCM 06 and LCM 07 were measured on a MicroMacro setup (quartz sword with Pt-needles and a Pt-sheet as working and counter electrodes), heated by a tube furnace. Temperature cycles and degradation impedance measurements were carried out.

All impedance measurements were done under ambient air and pressure in a temperature range of 380 °C and 593 °C.

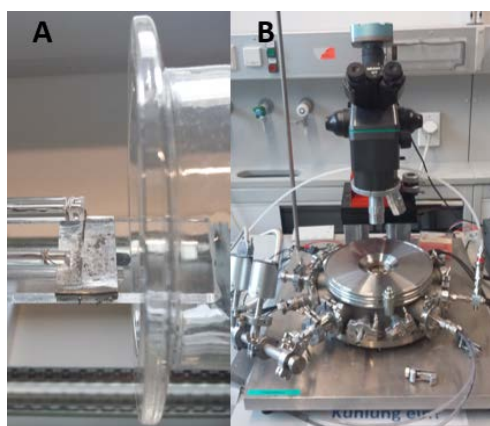


Figure 10: A) MicroMacro measurement set-up with Pt needle as working electrode contact and Pt sheet as counter electrode  
B) II-Pot with microscope and gas supply

In Figure 10 the two impedance measurement setups are pictured. On the left side A the MicroMacro setup with the Pt needles as working electrodes and the Pt sheet as counter electrode. The second picture B gives an overview of the II-Pot including the microscope, the pressure gauges and gas supply units.

## 4. Results and Discussion

### 4.1. Powder X-ray Diffraction (XRD Measurements)

#### 4.1.1 Purity Check PLD-Targets

It is essential that all used PLD-targets are as phase-pure as possible and consider out of the desired material. Therefore, before thin films production all targets had been analyzed by powder X-ray diffraction. In the following chapter, the diffractograms and peak lists of the target and the reference materials are shown. With these all present phases can be determined and visualized.

##### 4.1.1.1 LCM Target

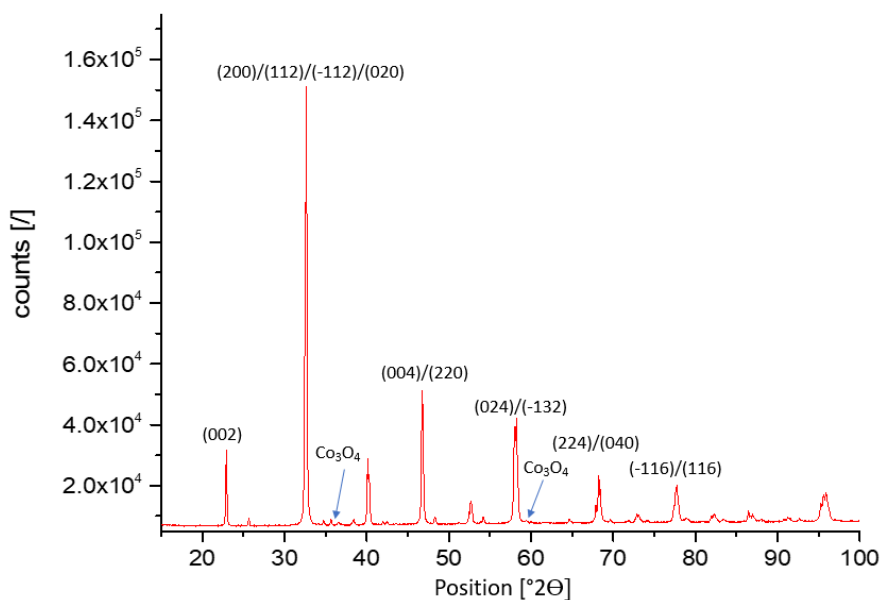


Figure 12: XRD diffractogram of the LCM target

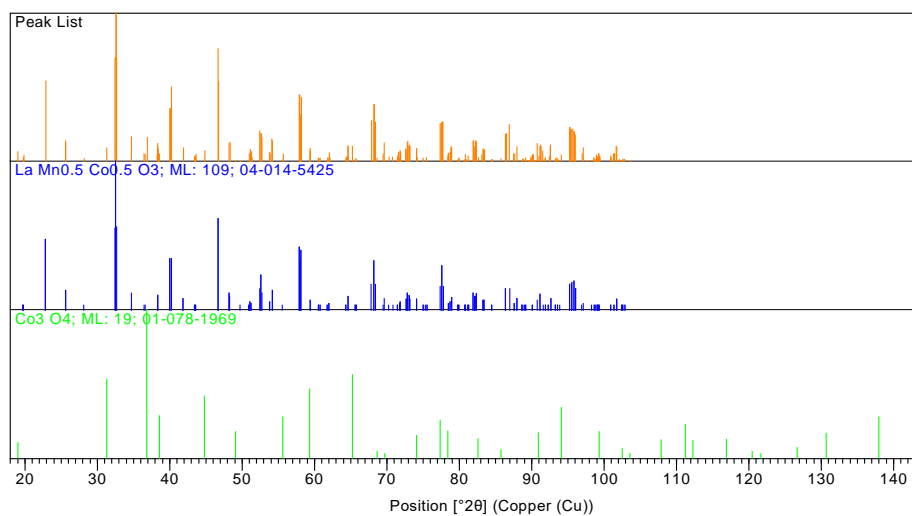


Figure 11: Peak lists of the target, LCM and  $\text{Co}_3\text{O}_4$  (top to bottom)

The XRD diffractogram of the LCM target (Figure 11) shows a minor impurity, as second phase  $\text{Co}_3\text{O}_4$  is present. A second sintering step did not lead to a single-phase structure, the  $\text{Co}_3\text{O}_4$  amount remained constant. The composition is 98.2 % LCM (reference code: 04-014-5425) and 1.8 %  $\text{Co}_3\text{O}_4$ . (ref. code: 01-078-1969). As expected both the LCM and  $\text{Co}_3\text{O}_4$  phase are polycrystalline. The peaks (311) at approximately  $36.8^\circ$  and (511) at nearly  $59.4^\circ$  are the most pronounced cobalt oxide peaks and the only ones which are assignable to the impurity in Figure 11. In Figure 12 the peak list of the measured target and literature peak lists of LCM and  $\text{Co}_3\text{O}_4$  are shown. The peaks of  $\text{Co}_3\text{O}_4$  with the highest relative intensity can be found in the target peak list. The cell parameters and crystal structures of the two compounds are listed in chapter 4.1.2.

#### 4.1.1.2 LCCM Target

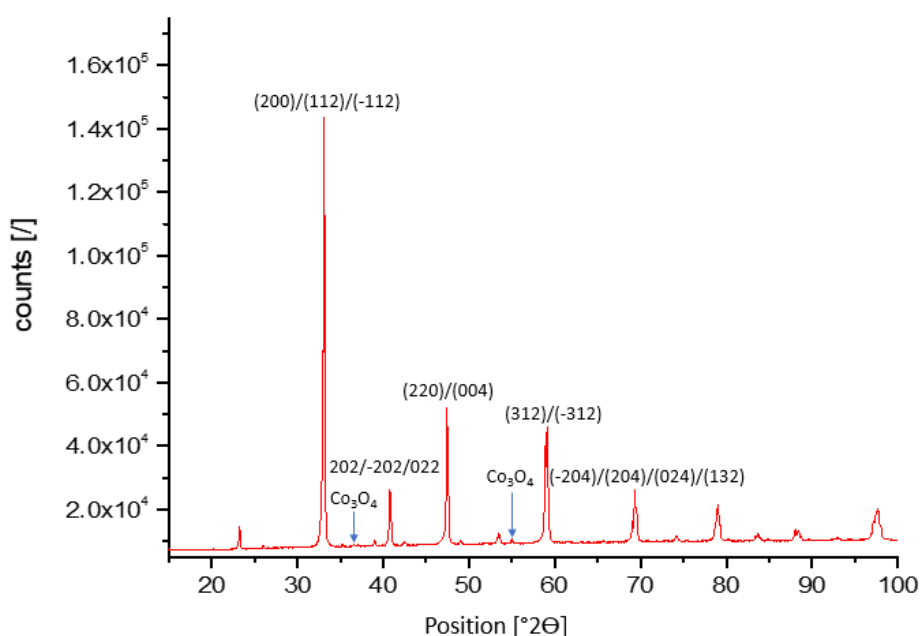


Figure 13: XRD diffractogram of the LCCM target

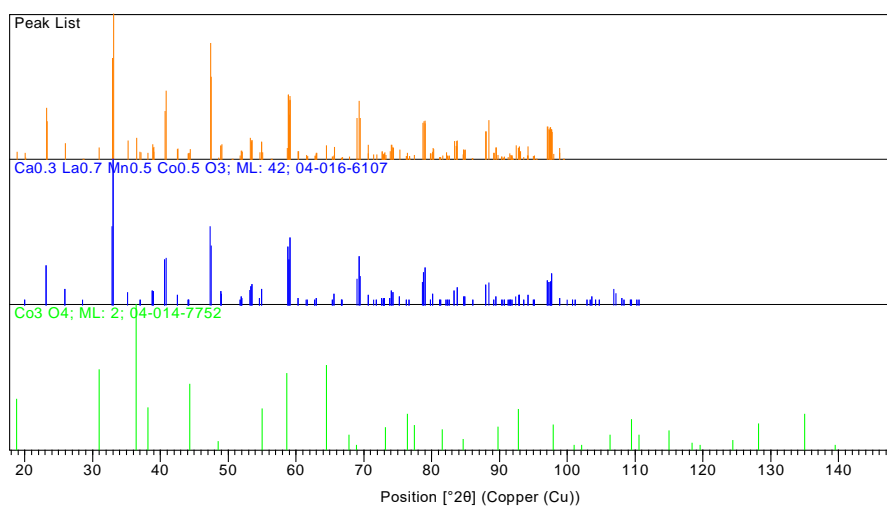


Figure 14: Peak lists of the target, LCCM,  $\text{Co}_3\text{O}_4$  (top to bottom)

The XRD diffractogram (Figure 13) of the LCCM target unveils tiny amounts of  $\text{Co}_3\text{O}_4$ . The polycrystalline sample consists of 99.1 % LCCM (ref. code 04-016-6107) and 0.9 %  $\text{Co}_3\text{O}_4$  (ref. code 04-014-7752). The two cobalt oxide peaks marked in Figure 13 refer to the (311) at  $36.4^\circ$  and the (422) peak at  $55.0^\circ$ . The peak lists (Figure 14) strengthen the assumption of two phases present in the target. This is due to the fact that the five most pronounced cobalt oxide peaks are present in the target, but cannot be found in the LCCM peak list. The cell parameters and crystal structures of the two compounds are listed in chapter 4.1.2

#### 4.1.1.3 LSCM Target

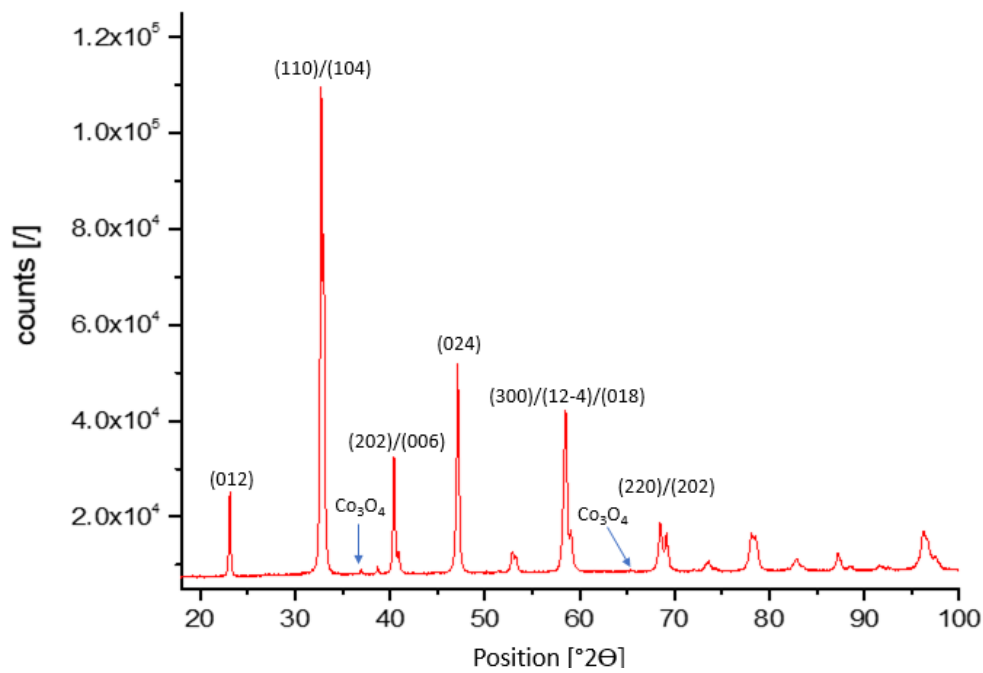


Figure 15: XRD diffractogram of the LSCM target

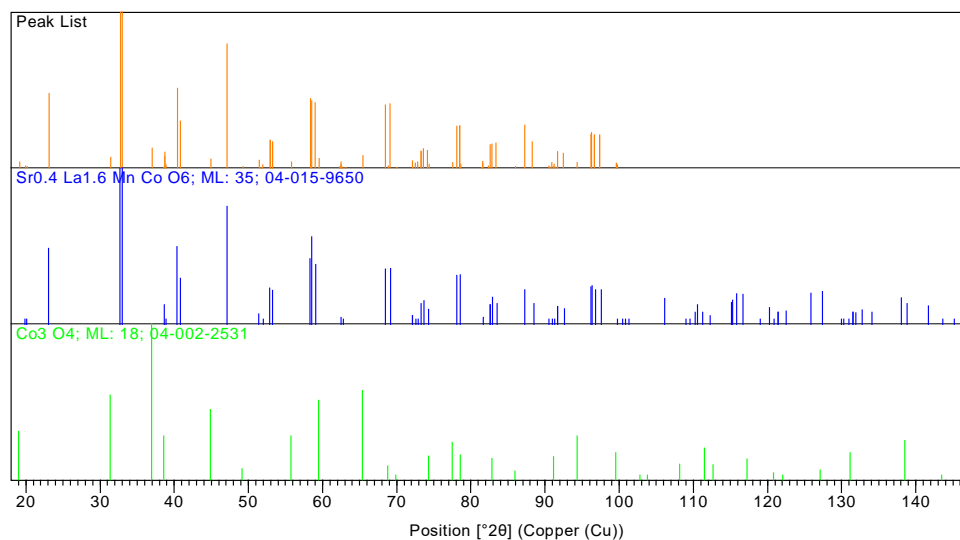


Figure 16: Peak lists of the target, LSCM and  $\text{Co}_3\text{O}_4$  (top to bottom)

The composition of the polycrystalline LSCM target is 99.2 % LSCM (ref. code 04-015-9650) and 0.8 %  $\text{Co}_3\text{O}_4$  (ref. code 04-002-2531). The two cobalt oxide peaks marked in Figure 15 refer to the (311) at  $36.9^\circ$  and the (440) peak at  $65.4^\circ$ . In Figure 16 the six most intensive  $\text{Co}_3\text{O}_4$  can be found only in the reference peak list of cobalt oxide and the target peak list, but not in the LSCM reference peak list. This proves the presence of an impurity in form of cobalt oxide in the target pellet. The cell parameters and crystal structures of the two compounds are discussed in chapter 4.1.2.

#### 4.1.1.4 $\text{LaCo}_{0.4}\text{Mn}_{0.6}\text{O}_3$ Target

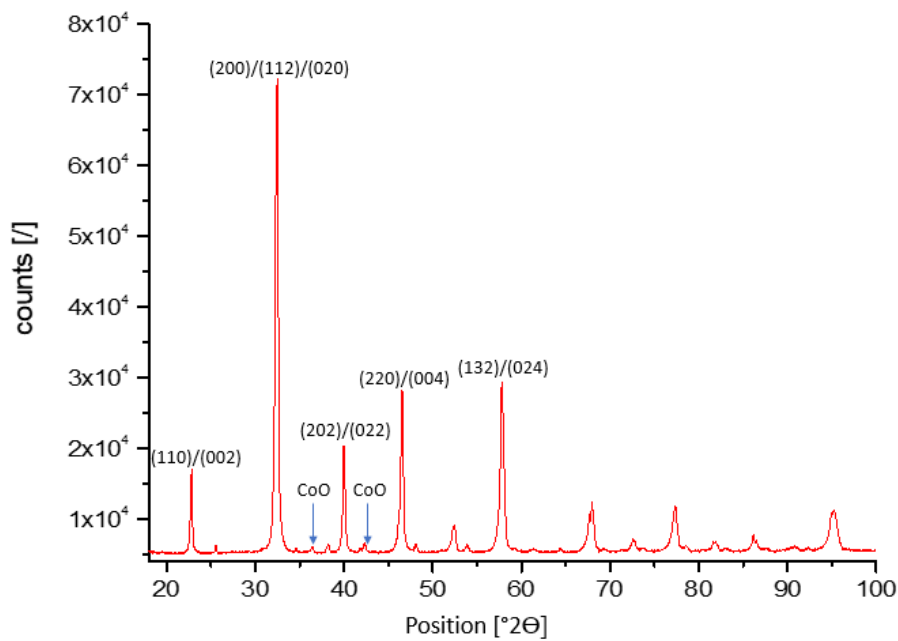


Figure 17: XRD diffractogram of the  $\text{LaCo}_{0.4}\text{Mn}_{0.6}\text{O}_3$  target

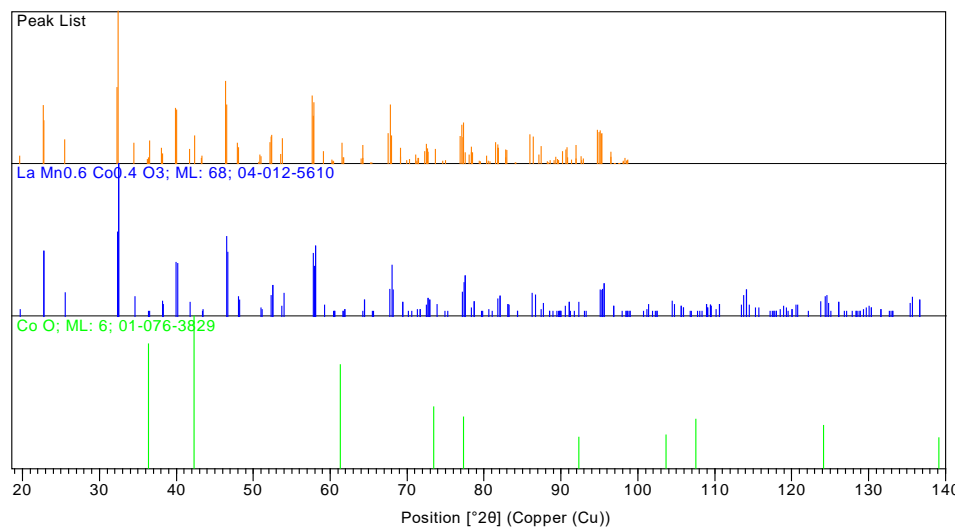


Figure 18: Peak lists of the target,  $\text{LaCo}_{0.4}\text{Mn}_{0.6}\text{O}_3$  and  $\text{CoO}$  (top to bottom)

The composition of the polycrystalline  $\text{LaCo}_{0.4}\text{Mn}_{0.6}\text{O}_3$  target is 98.4 %  $\text{LaCo}_{0.4}\text{Mn}_{0.6}\text{O}_3$  (ref. code 04-012-5610) and 1.6 %  $\text{CoO}$  (ref. code 01-076-3829). First the  $\text{CoO}$  was not found by the X'Pert HighScore program, the component had to be selected manually and subsequently its amount was calculated by Rietveld refinement. The identified  $\text{CoO}$  peaks in Figure 17 are (111) at  $36.5^\circ$ , (200) at  $42.4^\circ$  and (220) at  $61.5^\circ$ . The calculated cell parameters (without any internal standard) of the orthorhombic  $\text{LaCo}_{0.4}\text{Mn}_{0.6}\text{O}_3$  are a:  $5.5124 \text{ \AA}$ , b:  $7.7965 \text{ \AA}$  and c:  $5.5444 \text{ \AA}$  giving a cell volume of  $238.286 \text{ \AA}^3$ ; the corresponding space group is Pbnm.

#### 4.1.1.5 $\text{LaCo}_{0.6}\text{Mn}_{0.4}\text{O}_3$ Target

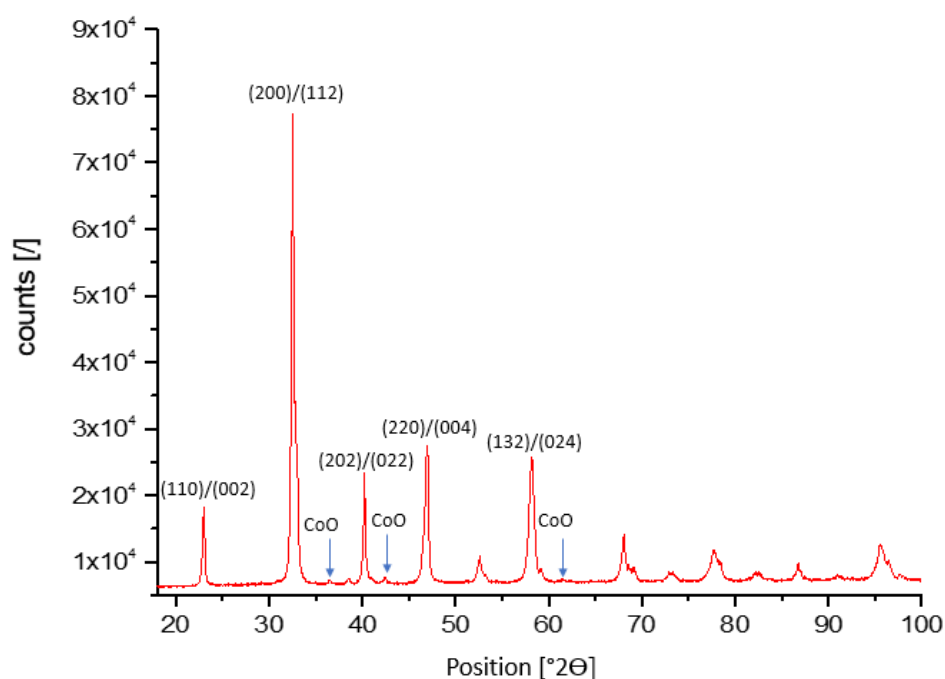


Figure 19: XRD diffractogram of the  $\text{LaCo}_{0.6}\text{Mn}_{0.4}\text{O}_3$  target

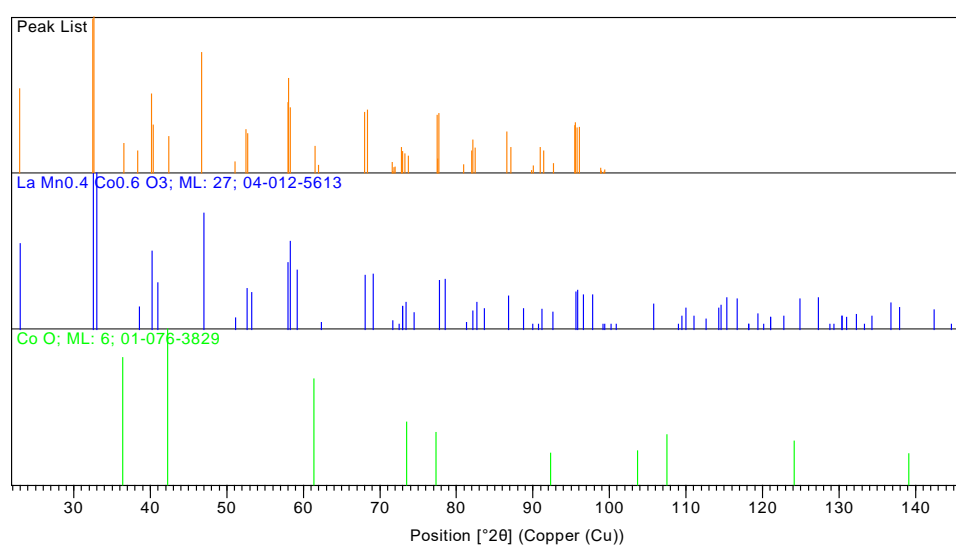


Figure 20: Peak lists of the target,  $\text{LaCo}_{0.6}\text{Mn}_{0.4}\text{O}_3$  and  $\text{CoO}$

The composition of the polycrystalline  $\text{LaCo}_{0.6}\text{Mn}_{0.4}\text{O}_3$  target is 98.7 %  $\text{LaCo}_{0.6}\text{Mn}_{0.4}\text{O}_3$  (ref. code 04-012-5613) and 1.3 %  $\text{CoO}$  (ref. code 01-076-3829). The identified  $\text{CoO}$  peaks in Figure 19 are (111) at  $36.5^\circ$ , (200) at  $42.4^\circ$  and (220) at  $61.5^\circ$ . The peak list (Figure 20) also unveils the presence of  $\text{CoO}$  in the target, since its three strongest peaks can only be found in the target peak list and not in the  $\text{LaCo}_{0.6}\text{Mn}_{0.4}\text{O}_3$  reference peak list. The calculated cell parameters (without any internal standard) of the rhombohedral  $\text{LaCo}_{0.6}\text{Mn}_{0.4}\text{O}_3$  are  $a = b: 5.5094 \text{ \AA}$  and  $c: 13.4140 \text{ \AA}$  giving a cell volume of  $352.629 \text{ \AA}^3$ ; the corresponding space group is  $R\bar{3}c$ .

To sum up all measurements for checking purity, the investigated targets are mostly phase pure and consist of the desired material and tiny amounts of cobalt oxide. LSCM is the purest target with only 0.8 %  $\text{Co}_3\text{O}_4$ .

#### 4.1.2 LCM, LCCM and LSCM Cell Parameters

In addition to the purity checks, the cell parameters of three target materials were determined by using an internal standard, starting with LCM in the following chapter.

##### 4.1.2.1 LCM Cell Parameters and Crystal Structure

For a precise cell parameter determination, errors from the sample preparation and measurement set-up have to be excluded. For that the internal standard  $\text{LaB}_6$  was used. The sharp intensive  $\text{LaB}_6$  peaks can clearly be identified and distinguished from the LCM peaks, hence it is suitable as internal standard. The distinguishability can be seen in the diffractogram of the mixture of  $\text{LaB}_6$  and LCM powder (Figure 21) and the peak lists of the measured sample, the reference  $\text{LaB}_6$  peak list and the reference LCM peak list (Figure 22)

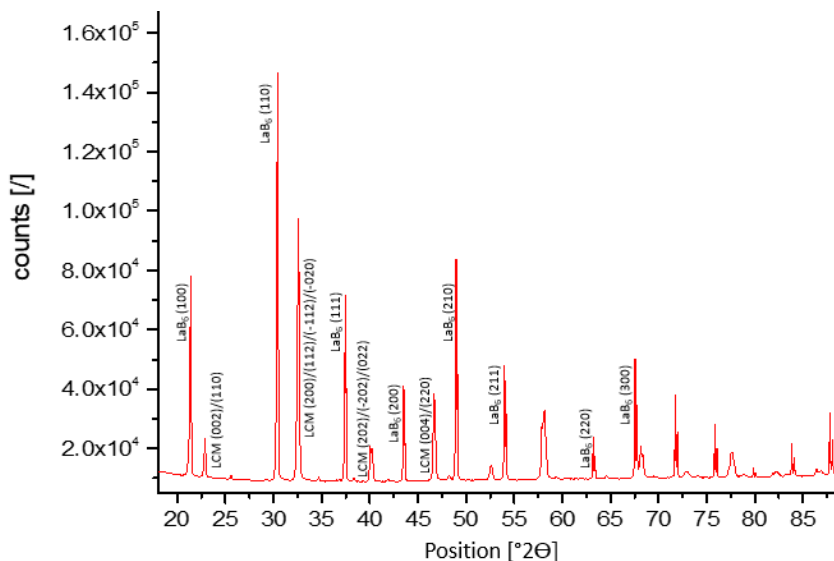


Figure 21: XRD diffractogram of LCM and  $\text{LaB}_6$  powder

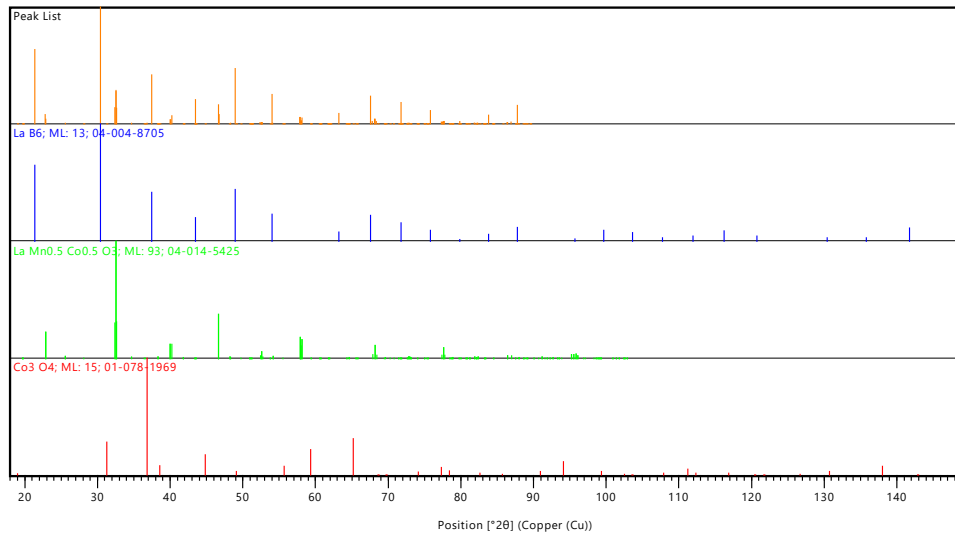


Figure 22: Peak lists target of the powder + LaB<sub>6</sub>, LaB<sub>6</sub>, LCM and Co<sub>3</sub>O<sub>4</sub> (top to bottom)

Rietveld refinement gives the following cell parameters  $a$ : 5.5225 Å  $b$ : 5.4871 Å  $c$ : 9.5262 Å and  $\beta$ : 125.358°. These values refer to the monoclinic space group P21/n, nevertheless there is a dramatic difference between the reported  $b$  and  $\beta$  parameters compared to the calculated ones. This is a consequence of the use of a different basis in the Rietveld refinement. The transformation to the originally used basis is shown in Figure 23 and the following equations.

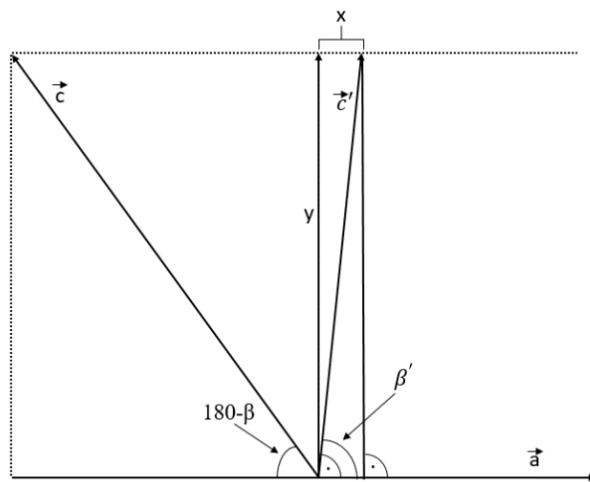


Figure 23: Basis transformation of a monoclinic unit cell

$$x = c \cdot \cos \beta + a \quad (31)$$

$$y = c \cdot \sin \beta \quad (32)$$

$$\beta' = \tan^{-1} \left( \frac{c \cdot \sin \beta}{c \cdot \cos \beta + a} \right) \quad (33)$$

$$c' = \sqrt{x^2 + y^2} \quad (34)$$

$c, a$  ..... cell parameters before transformation [Å]

$\beta$  ..... cell parameter before transformation [°]

$c'$  ..... cell parameter after transformation [Å]

$\beta'$  ..... cell parameter after transformation [°]

$x, y$  ..... auxiliary parameters [Å]



Considering the transformation, the determined cell parameters are  $c'$ : 7.6596 Å and  $\beta'$ : 89.923°, giving a cell volume of 235.319 Å<sup>3</sup>.

To classify the quality of the analysis, the cell parameters of the cubic LaB<sub>6</sub> calculated by Rietveld refinement were compared to the indexed parameters of the standard reference material 660b; calculated:  $a = b = c = 4.15699$  Å, indexed:  $a = b = c = 4.15691$  (8) Å. Thus, the cell parameter determination worked well and they match with the reported values.[15-17, 19]

Moreover Singh et al. described that B-site ordering is accompanied by a phase transition from an orthorhombic to a monoclinic phase.[15] Even though in our case B-site ordering cannot be confirmed directly with the used XRD diffractometers, the monoclinic structure of the sample allows the assumption that the B-sites of the synthesized LCM target are partially ordered.

#### 4.1.2.2 LCCM Cell Parameters and Crystal Structure

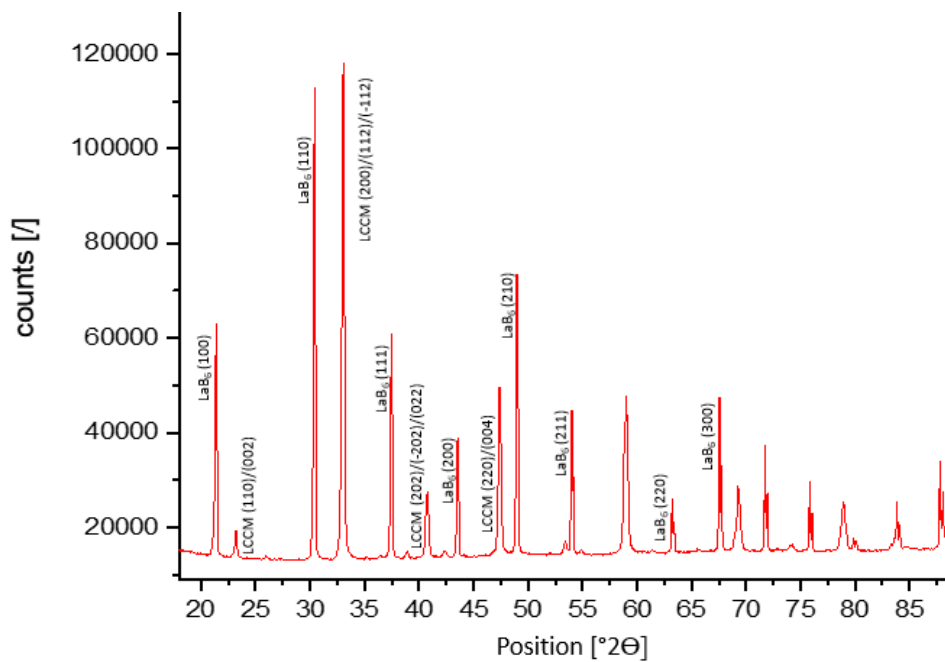


Figure 24: XRD diffractogram of LCCM + LaB<sub>6</sub> powder

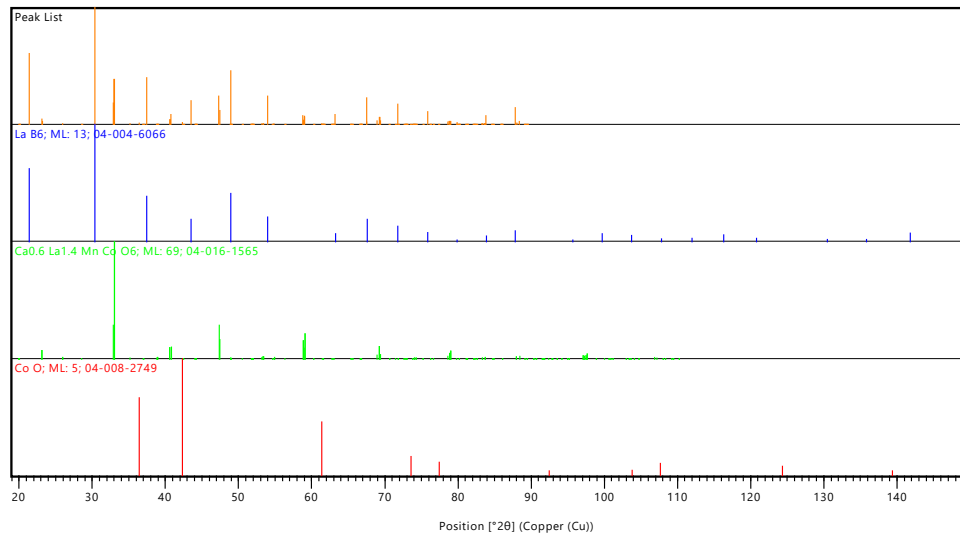


Figure 25: Peak lists of the target powder +  $\text{LaB}_6$ ,  $\text{LaB}_6$ , LCCM and  $\text{CoO}$

Based on the XRD diffractogram of the LCCM target powder mixed with the internal standard  $\text{LaB}_6$  (Figure 25) the following cell parameters are obtained:  $a$ : 5.4435 Å,  $b$ : 5.4138 Å  $c$ : 9.3915 Å and  $\beta$ : 125.354°. The volume of the unit cell is 225.729 Å<sup>3</sup> and the space group P21/n (monoclinic crystal structure). The transformation to the mostly used basis gives  $c$ : 7.5961 Å and  $\beta$ : 89.930°. Thus, Ca doping of LCM leads to smaller cell parameters. The suitability of  $\text{LaB}_6$  as internal standard can be seen in Figure 27, there are no peaks at the  $2\theta$  positions of  $\text{LaB}_6$ , either from  $\text{CoO}$  or LCCM.

The quality of the refinement is excellent, since the calculated cell parameter of  $\text{LaB}_6$  is  $a$ : 4.15691 Å. Compared with literature data a good accordance is found. [27]

#### 4.1.2.3 LSCM Cell Parameters and Crystal Structure

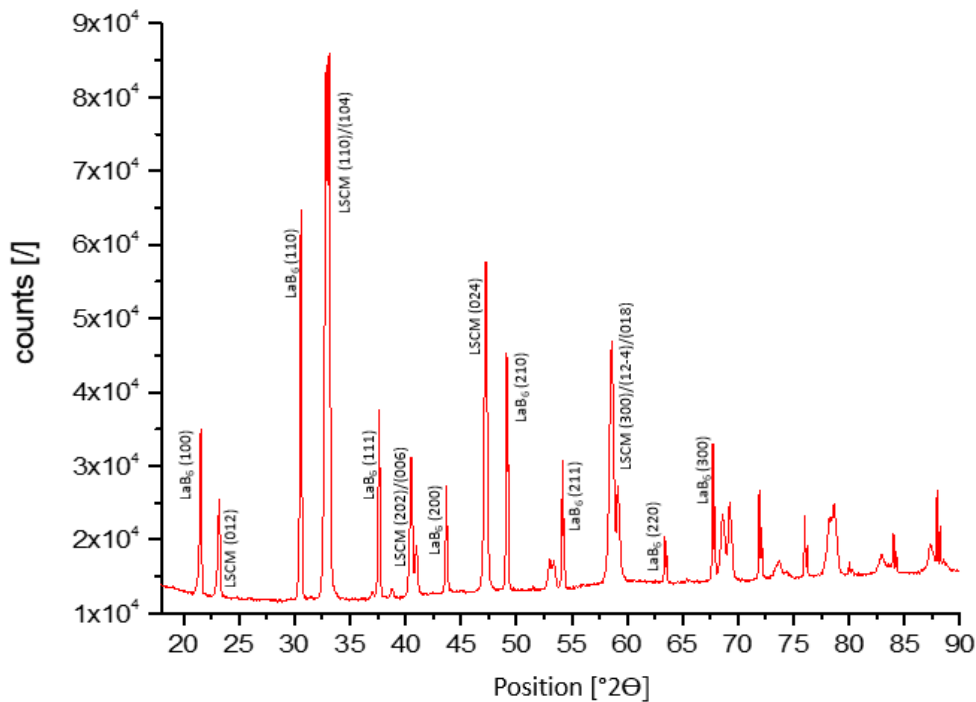


Figure 26: XRD diffractogram of LSCM + LaB<sub>6</sub> powder

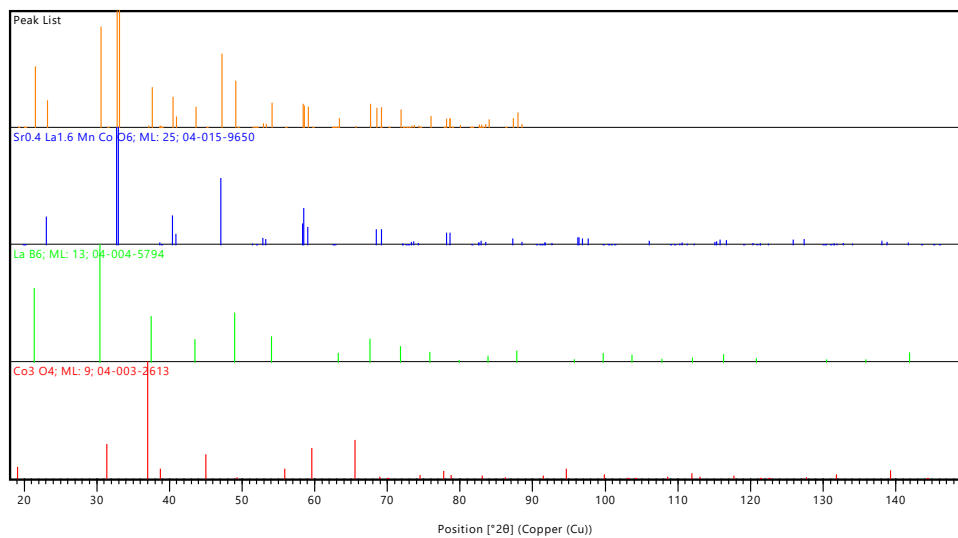


Figure 27: Peak lists target of the powder + LaB<sub>6</sub>, LaB<sub>6</sub>, LSCM and Co<sub>3</sub>O<sub>4</sub>

Rietveld refinement of the LSCM powder mixed with the internal standard gives  $a = b = 5.4788 \text{ \AA}$ ,  $c = 13.2555 \text{ \AA}$ ,  $\alpha = \beta = 90.00^\circ$  and  $\gamma = 120.00^\circ$  as cell parameters. The volume of the rhombohedral (R-3) unit cell is  $344.584 \text{ \AA}^3$ . The cell parameter of LaB<sub>6</sub> is smaller than expected, it is  $a = 4.15412 \text{ \AA}$ . Nevertheless, the measurement is precise enough for our purpose. Again, the values are in line with parameters from literature. [27, 28] The diffractogram of the measurement is shown in Figure 26. The 111 LaB<sub>6</sub> peak is very close to the 311 Co<sub>3</sub>O<sub>4</sub> peak, however that is not a problem, since the amount of cobalt oxide is so small that this specific

peak cannot be found in the recorded diffractogram respectively in the peak list of the measurement (Figure 27).

## 4.2 Atomic Force Microscopy (AFM Measurements)

For surface roughness determination AFM measurements in tapping mode were performed. The films of the investigated samples LCM 13, LCM 17 and LCM 18 were grown with a deposition rate of 1 Hz and the thin films LCM 19, LCM 20 and LCM 21 with 5 Hz. The taken pictures are shown in Figure 28 and Figure 29.

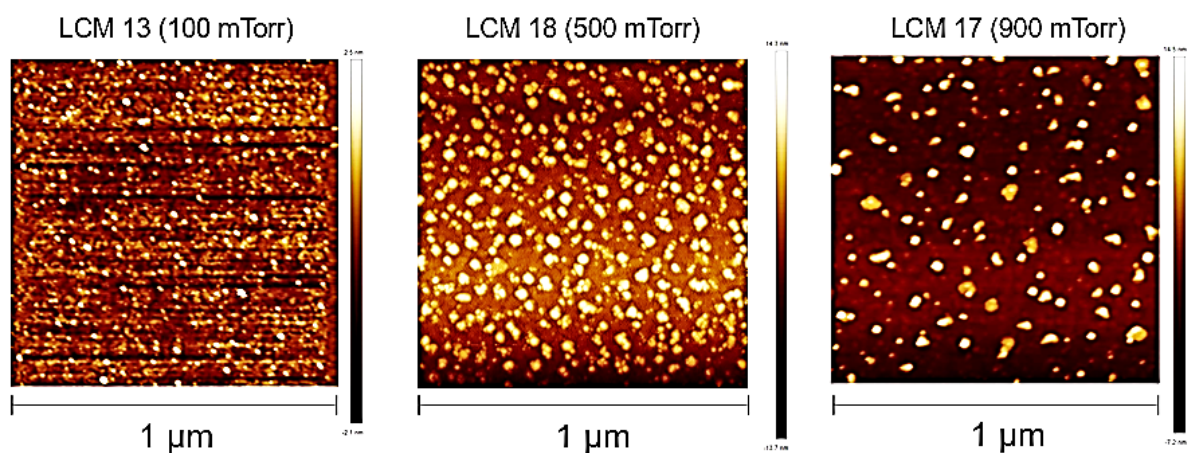


Figure 28: AFM pictures of LCM 13, 17 and 18

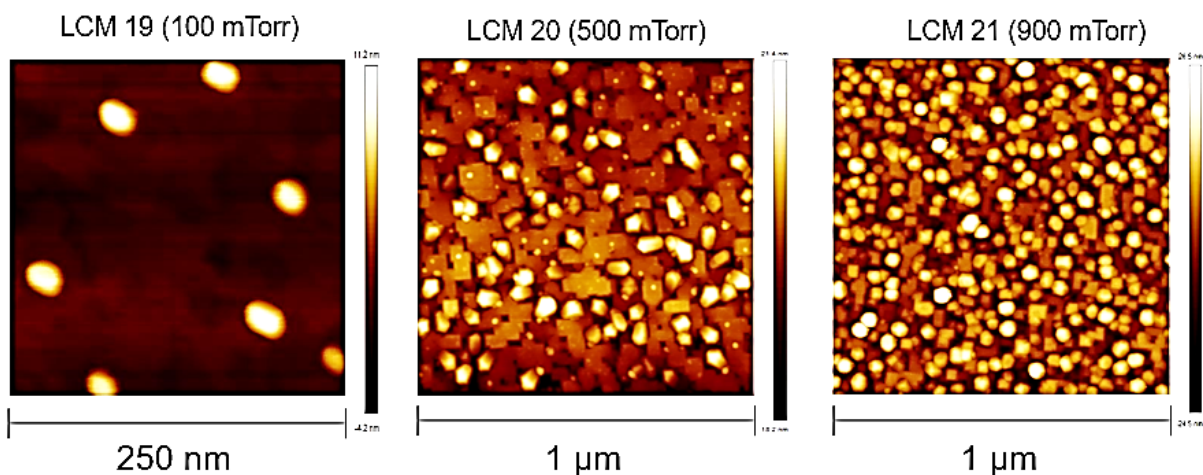


Figure 29: AFM pictures of LCM 19, 20 and 21

All samples have numerous islands on their surfaces. Those grow in number and size with increasing deposition background pressure. In addition, samples grown with 5 Hz deposition rate have a higher surface roughness than LCM 13, 17 and 18 deposited with 1 Hz. In Figure 30 the change in surface roughness is plotted. Both series show the same trend of a rising  $R_q$

and reach their maximum at 900 mTorr  $p(\text{O}_2)$  and 2.69 nm (1 Hz) and 7.41 nm (5 Hz). In general, low  $p(\text{O}_2)$  in combination with elevated temperatures during thin film growth minimize the nucleation on top of a 2D island, since diffusivity of the adatoms on the surface is enhanced. Thus, the higher the pressure and the lower the temperature the higher the probability of island growth and the rougher the surface becomes.[65] Furthermore, it is known from literature that lower deposition rates lead to smaller islands and therefore to a smoother surface. Looking at the surface morphology either Volmer–Weber or Stranski–Krastanov growth mode can be proposed.[73]

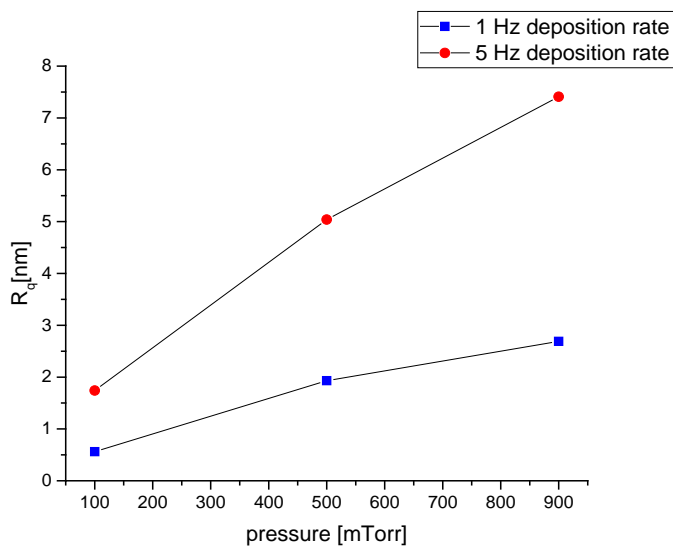


Figure 30: Surface roughness  $R_q$  of LCM thin films

### 4.3 Transmission Electron Microscopy Images (TEM)

TEM-images were taken to characterize the deposited thin films, to get an idea whether dislocations are present and to determine the film thickness. The following four images were taken at the USTEM and give an impression of the samples structure.

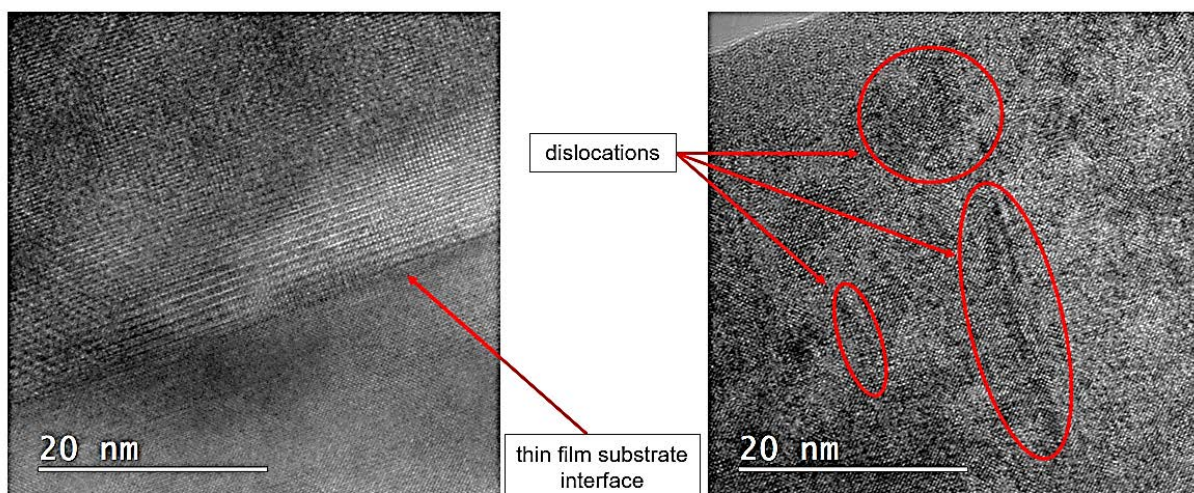


Figure 31: TEM images of LCM on a STO (001) single crystal

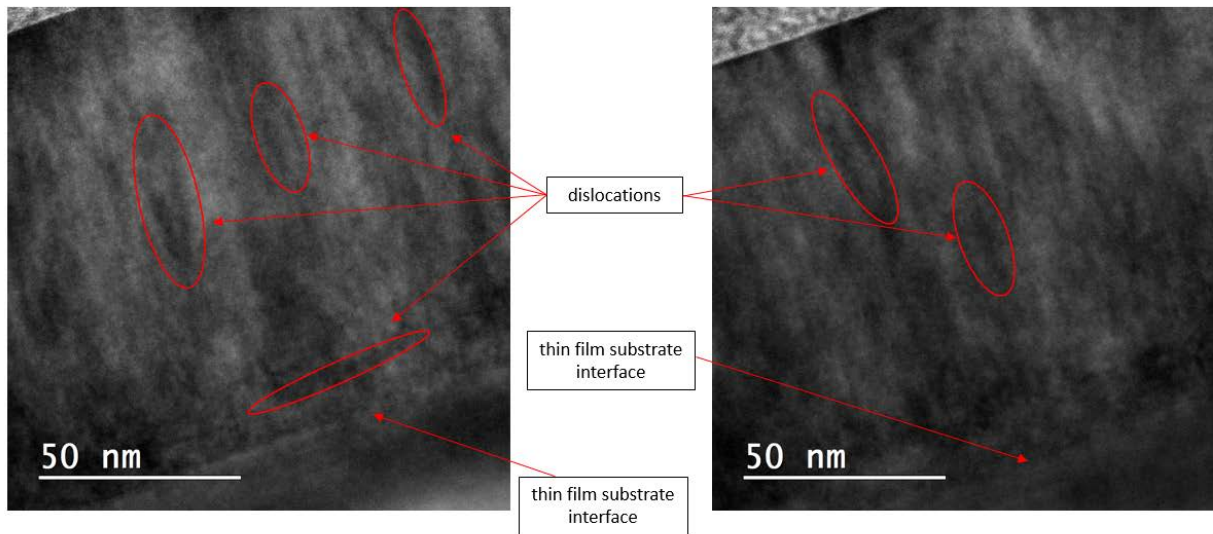


Figure 32: TEM images of LCM on LAO (001) single crystal (sample LCM 21)

The transmission electron microscopy pictures (Figure 31 and Figure 32) show LCM thin films deposited on STO and LAO. In Figure 31 a LCM film with a clearly distinguishable film substrate (STO) interface can be seen. The deposited LCM has a lot of features that might be dislocation, marked with red circles. LCM 21 (Figure 32) exhibits an epitaxial film with a clear thin film substrate interface and supposed dislocations pictured as dark areas and marked with red circles.

Furthermore, the thickness of the samples LCM 19, LCM 21 and LCCM 09 were determined from the TEM pictures. LCM 21 has a film thickness of 104 nm, LCM 19 of 47 nm and LCCM 9 of 60 nm, the thicknesses of the other samples were calculated by using the sputtering SIMS rate or the PLD deposition rate. It was assumed that the LCM samples have the same dimensions as the  $\text{LaCo}_{0.4}\text{Mn}_{0.6}\text{O}_3$  and  $\text{LaCo}_{0.6}\text{Mn}_{0.4}\text{O}_3$  thin films, prepared under the same conditions.

## 4.4 Van der Pauw Measurements

Van der Pauw Measurements were made to determine the conductivity of the targets and of the produced thin films. Moreover, the impact of A-site doping and of a reducing atmosphere during the resistivity measurements on the conductivity and activation energy was investigated, starting with the bulk samples.

### 4.4.1 Bulk Samples

All bulk samples were cut from the targets and exhibit painted Pt-electrodes at the edges. An overview of the natural logarithm of the obtained conductivities multiplied by the temperature against the reciprocal temperature is given in Figure 33.

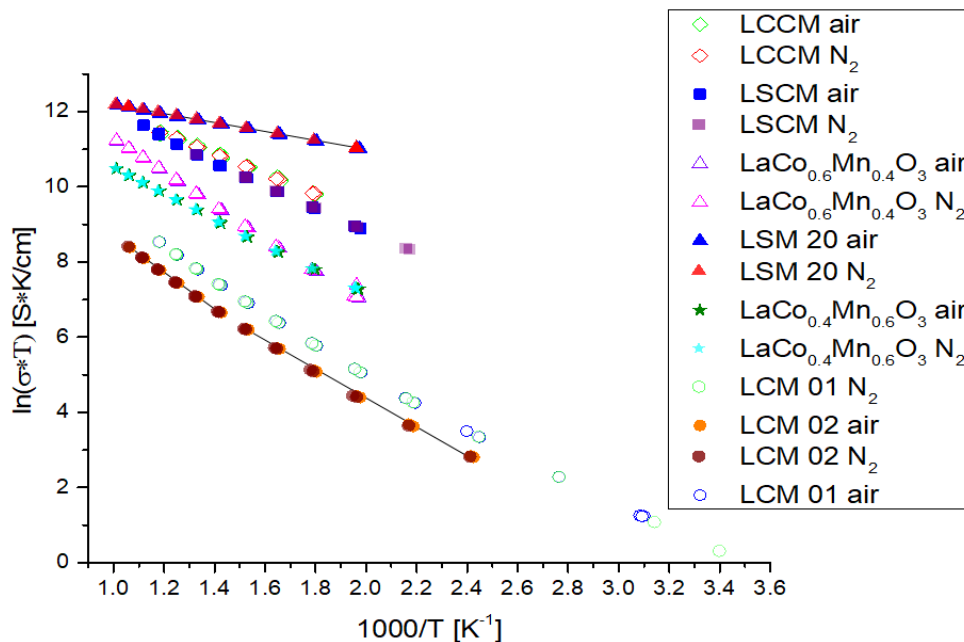


Figure 33:  $\ln(\sigma^*T)$  vs the reciprocal temperature of all polycrystalline bulk samples

For almost all specimens, a linear correlation between  $\ln(\sigma^*T)$  and the reciprocal temperature is observed. LCM has the lowest conductivity of all measured bulk samples. Both produced LCM bulk targets (LCM 01 and LCM 02) have a very similar conductivity. Minor differences are nothing to be concerned of, since the samples differ a little bit in their optical appearance. This is in accordance with literature, since in 1966 Jonker observed the lowest conductivity at room temperature in the described compound system for a Co to Mn ratio of 1:1.[26]

Only the least conducting LCM bulk specimens show a bending of the curve, all other bulk samples have one activation energy. Due to this bend, two linear fits were made to calculate the

activation energies of the conductivity. The black lines in Figure 33 illustrate the obtained functions.

$\text{LaCo}_{0.4}\text{Mn}_{0.6}\text{O}_3$  has the second lowest conductivity, nevertheless a clear increase can be observed compared to bulk LCM. At low temperatures, the conductivity of  $\text{LaCo}_{0.6}\text{Mn}_{0.4}\text{O}_3$  is in the same range, but its increase with temperature is much stronger.  $\text{LaCo}_{0.6}\text{Mn}_{0.4}\text{O}_3$  exhibits the lowest resistivity of all non-doped bulk samples. A higher relative amount of Co in the material was expected to lead to an increase in the conductivity, since  $\text{LaCoO}_3$  is much more conductive than  $\text{LaMnO}_3$ .

LCCM's and LSCM's resistivity is nearly the same, even though LCCM is doped with 30 % Ca and LSCM only with 20 % of Sr at the A-site. The impact of doping can be seen in Figure 35. The highest bulk conductivity of the investigated compounds at all measured temperatures has  $\text{La}_{0.8}\text{Sr}_{0.2}\text{MnO}_3$ . The dark line illustrates that only one fit with the least square method was needed to obtain the activation energy. All materials were studied under ambient air and  $\text{N}_2$  containing nominal 2 ppm of  $\text{O}_2$ , the conductivity of LSCM was even measured under ca. 1 atm  $\text{O}_2$ . Since the atmosphere during the measurements seems to have no impact on the conductivity, the investigated bulk specimens are hardly reducible.

The activation energy ( $E_a$ ) gives an impression of the evolution of the mobility of the charge carriers in the investigated materials with the change in temperature. All obtained values are listed in Table 4 below.

Table 4: Bulk activation energies of the electrical conductivity under ambient and  $\text{N}_2$  atmosphere

bulk samples	activation energy [eV]
LSM 20 air	0.10
LSM 20 $\text{N}_2$	0.10
LCM 02 air low temp	0.31
LCM 02 air high temp	0.39
LCM 02 $\text{N}_2$ low temp	0.31
LCM 02 $\text{N}_2$ high temp	0.39
LCM 01 air low temp	0.30
LCM 01 air high temp	0.39
LCM 01 $\text{N}_2$ low temp	0.30
LCM 01 $\text{N}_2$ high temp	0.39
LCCM air	0.23
LCCM $\text{N}_2$	0.23
LSCM 01 air	0.27



LSCM 01 O <sub>2</sub>	0.26
LSCM 01 N <sub>2</sub>	0.26
LaCo <sub>0.4</sub> Mn <sub>0.6</sub> O <sub>3</sub> N <sub>2</sub>	0.29
LaCo <sub>0.4</sub> Mn <sub>0.6</sub> O <sub>3</sub> air	0.29
LaCo <sub>0.6</sub> Mn <sub>0.4</sub> O <sub>3</sub> N <sub>2</sub>	0.37
LaCo <sub>0.6</sub> Mn <sub>0.4</sub> O <sub>3</sub> air	0.38

The difference of the activation energies obtained from measurements from the same material under air, N<sub>2</sub> or O<sub>2</sub> are negligible. LSM has the lowest activation energy with 0.10 eV and LCM at elevated temperature the highest. The bend in the LCM data series leads to a steeper slope and therefore to an increase in  $E_a$  of 0.09 eV above ca. 450 °C. With an increasing relative amount of Co an increase of  $E_a$  (at temperatures below 450 °C) can be observed in undoped specimens. The activation energy rises from 0.29 eV in LaCo<sub>0.4</sub>Mn<sub>0.6</sub>O<sub>3</sub> to 0,38 eV in LaCo<sub>0.6</sub>Mn<sub>0.4</sub>O<sub>3</sub>.

Even though LCCM and LSCM show nearly the same conductivity their  $E_a$  differ (LCCM: 0.23 eV and LSCM: 0.26 eV), hence LSCM is going to surpass LCCM in terms of conductivity at temperatures above about 800 °C. This was calculated from the linear fits, since such high temperatures were not achieved during the measurement cycles. The standard derivations of all  $E_a$  are below 0.01 eV, hence they are not mentioned in Table 4.

In undoped LaCo<sub>1-x</sub>Mn<sub>x</sub>O<sub>3</sub> samples conductivity changes with the ratio between Co and Mn. To describe this particular resistivity evolution the log of the conductivities at 500 °C and 700 °C and under ambient air are plotted against the relative Mn concentration in Figure 34 below.

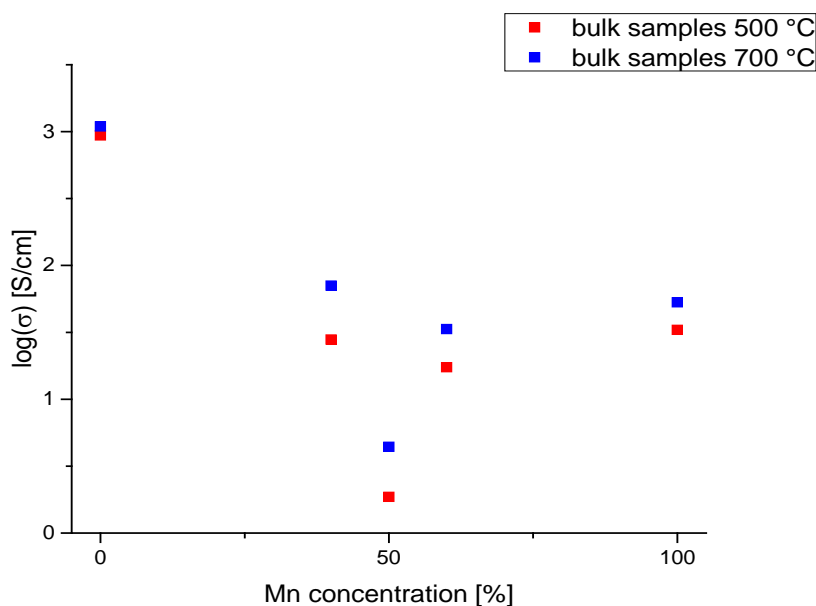


Figure 34: Log( $\sigma$ ) vs relative Mn concentration of undoped bulk samples

The data of  $\text{LaCoO}_3$  and  $\text{LaMnO}_3$  presented in Figure 34 were not measured during the thesis they were taken from literature and only used to complete the picture and help to understand the connection between Mn:Co ratio and conductivity. Polycrystalline  $\text{LaMnO}_3$  was investigated by the four-point technique at 400 Hz at 1 atm  $p(\text{O}_2)$ . [74] Since the impact of  $p(\text{O}_2)$  on the conductivity at such high pressures is nearly negligible the data can be used despite the difference in oxygen partial pressure. [74]

The conductivity of a 3-4 mm thick  $\text{LaCoO}_3$  single crystal was obtained by Mizusaki et al. using a DC four probe as well. [75, 76] Even though a single crystal was used for conductivity determination, the data were compared to the investigated specimens, since only a qualitative idea of the obtained values should be gained.

$\text{LaCoO}_3$  exhibits by far the highest conductivity, it is in a range of 1000 S/cm and temperature seems to have a minor impact. By increasing Mn concentration the conductivity drops sharply to 28 S/cm at 500 °C respectively 71 S/cm at 700 °C for 40 % Mn. The maximum of the measured resistivity is reached at a Mn concentration of 50 %, this phenomenon is known from literature. It is assumed that the formation of  $\text{Mn}^{4+}$  and  $\text{Co}^{2+}$  is responsible for the occurrence of this minimum in the conductivity. [26] A further increase of the relative amount of Mn causes a rise in conductivity, nevertheless a ratio of Mn:Co 60:40 is slightly less conductive than a composition of 40:60. Even though Co acts as p-dopant in  $\text{LaMnO}_3$  [26], pure  $\text{LaMnO}_3$  possesses the second lowest resistivity after  $\text{LaCoO}_3$  at 500 °C. At 700 °C its conductivity is higher than the conductivity of  $\text{LaCo}_{0.4}\text{Mn}_{0.6}\text{O}_3$ .

Not only the B-site composition had an impact on the conductivity, Ca and Sr A-site doping have a massive influence as well. Both act as p-dopants and increase the hole concentration, the theoretical background is given in chapter 2.5. In Figure 35 the effect of A-site doping is pictured.

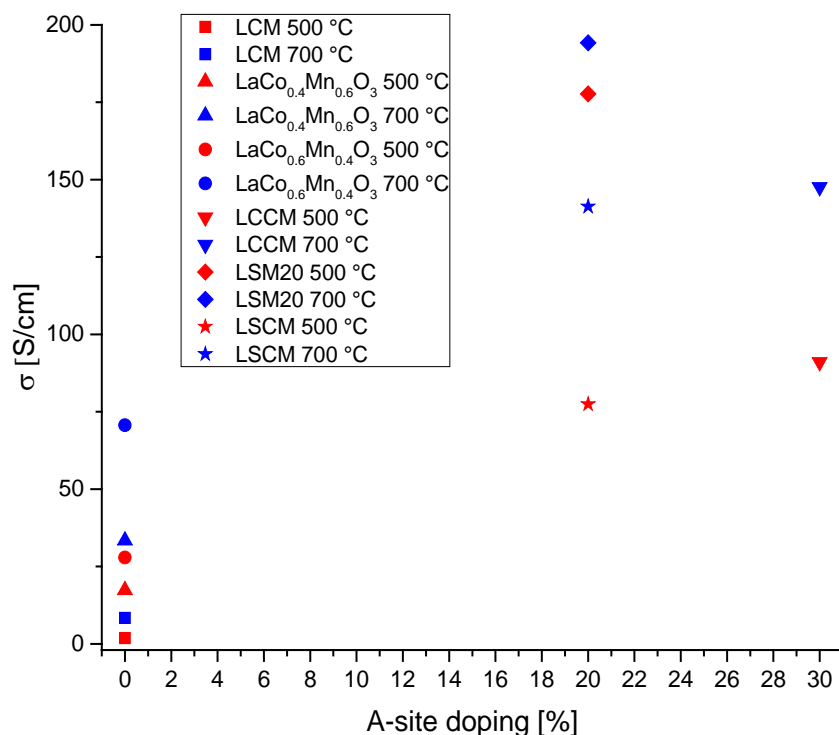


Figure 35: Impact of Ca or Sr A-site doping on the conductivity

The higher the relative amount of A-site doping the higher conductivity becomes, considering LCM as reference point. LCCM with 30 % Ca has the lowest resistivity of all investigated LaCo<sub>1-x</sub>Mn<sub>x</sub>O<sub>3</sub> bulk specimens and LSCM with 20 % Sr the second lowest. Nevertheless at 700 °C both show nearly the same conductivities. Hence, Sr seems to be a better dopant as Ca at elevated temperatures. Moreover as mentioned above, a change in the Co:Mn ratio increases the conductivity as well, but not as much as A-site doping. LSM is doped with 20 % Sr and exhibits the lowest resistivity at both 500 °C and 700 °C.

#### 4.4.2 LaCo<sub>0.5</sub>Mn<sub>0.5</sub>O<sub>3</sub> Thin Film Samples

Since thin films mostly show a different resistivity than the bulk, also thin film samples were investigated by the van der Pauw method. As mentioned deposition parameters have a tremendous influence on the structure of LCM, therefore thin films produced under three different background pressures and two different repetition rates were analyzed.

The results of the  $\text{LaCo}_{0.5}\text{Mn}_{0.5}\text{O}_3$  (LCM) thin film measurements under ambient atmosphere are summarized in Figure 36. Thin films were deposited with a repetition rate of 1 Hz and 5 Hz and under three different background pressures in the PLD chamber during thin film growth, giving different thick specimens.

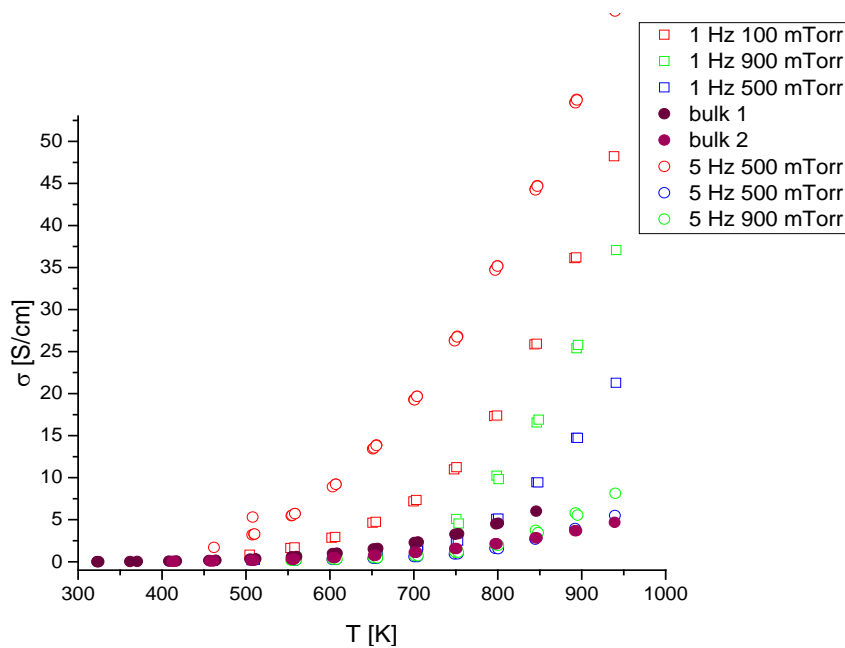


Figure 36: Van der Pauw measurements of  $\text{LaCo}_{0.5}\text{Mn}_{0.5}\text{O}_3$  thin films deposited with 1 Hz and 5 Hz repetition rate

The plotted thin films in Figure 36 show an increase of their conductivity with increasing temperature. Most of the samples exhibit a lower resistivity than the corresponding two bulk samples in the investigated temperature range. Generally speaking, specimens deposited under 100 mTorr  $p(\text{O}_2)$  have the highest conductivity, followed by those produced under 500 mTorr and those prepared under 900 mTorr. The preparation parameters 5 Hz and 100 mTorr lead to the highest conductivity and 5 Hz 900 mTorr to the lowest. The 5 Hz 500 mTorr and 5 Hz 900 mTorr samples have nearly the same conductivity. The resistivity of the 1 Hz samples lies between those of 5 Hz 100 mTorr and the other 5 Hz specimens. The activation energies were calculated from the slope of the linear fit obtained from the data series gained if  $\ln(\sigma \cdot T)$  is plotted against the reciprocal temperature. For all samples except 5 Hz 100 mTorr these Arrhenius plots show a bend between 377 °C and 452 °C with an increased slope at temperatures above these transition points (1 Hz samples bend is between 377 °C to 411 °C; for 5 Hz samples at 450 °C and 452 °C). Hence for these thin films two activations energies were calculated, one for low temperatures below each transition point and one for high temperatures above each transition point. The mentioned transition temperatures are the

calculated intersection points of the two linear fits for each specimen. The standard deviation of the slopes was again negligible. An overview of the obtained  $E_a$  is given in Table 5 below.

*Table 5: Activation energies of LCM thin films measured under ambient air and  $N_2$  containing 10 ppm  $O_2$*

Thin films with deposition parameters	$E_a$ [eV]
1 Hz 100 mTorr low temp	0.37
1 Hz 100 mTorr high temp	0.50
1 Hz 500 mTorr low temp	0.31
1 Hz 500 mTorr high temp	0.77
1 Hz 900 mTorr low temp	0.33
1 Hz 900 mTorr high temp	0.73
5 Hz 100 mTorr	0.34
5 Hz 500 mTorr low temp	0.34
5 Hz 500 mTorr high temp	0.65
5 Hz 900 mTorr low temp	0.34
5 Hz 900 mTorr high temp	0.72

Below the transition all thin films exhibit activation energies in the range of 0.31 eV and 0.37 eV. Hence the increase of conductivity with temperature is quite similar in this temperature range. Below the bend in the obtained data series all samples deposited with a repetition rate of 5 Hz have the same activation energy ( $E_a = 0.34$  eV). The behavior is quite bulk like, since the LCM bulk samples have an  $E_a$  of 0.30 eV respectively 0.31 eV.

Above 452 °C the slope of the linear fits rises strongly and the  $E_a$  values differ a lot. They are in a range of 0.34 eV for the 5 Hz 100 mTorr sample and 0.77 eV for the thin film deposited with 1 Hz under 500 mTorr. Especially samples prepared under 500 mTorr and 900 mTorr show high activation energies of around 0.7 eV.

Since deposition parameters have a significant impact on the conductivities and activation energies, conductivity at three different temperatures is plotted against the background pressure during the depositions in Figure 37.

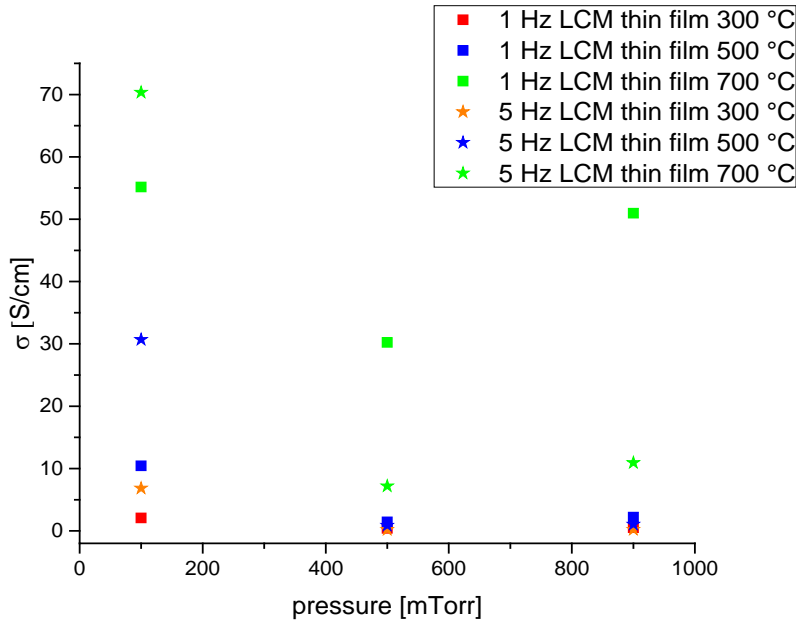


Figure 37: Conductivity evolution of LCM thin film samples with background pressure during deposition at 300 °C, 500 °C and 700 °C

As mentioned above, thin films deposited under 500 mTorr have the highest resistivity. The conductivity increase of all specimens is more pronounced between 500 °C and 700 °C than between 300 °C and 500 °C. This behavior can be explained with the Arrhenius dependence of the conductivity from temperature combined with the transition at around 400 °C. Thin films produced under 500 mTorr and 900 mTorr  $p(\text{O}_2)$  have nearly the same conductivity at 300 °C and 500 °C, the repetition rate seems to have an impact at high temperatures only.

#### 4.4.3 $\text{LaCo}_{0.4}\text{Mn}_{0.6}\text{O}_3$ Thin Film Samples

Thin films of  $\text{LaCo}_{0.4}\text{Mn}_{0.6}\text{O}_3$  were produced under various  $p(\text{O}_2)$  and their resistances measured by van der Pauw method under ambient air and  $\text{N}_2$  containing nominal 2 ppm  $\text{O}_2$ . The results are summarized in the Arrhenius plot (Figure 38) below. All thin films have bends in their data series at around 460 °C and a steeper slope above these transition points. Moreover, a reduced conductivity was observed when the specimens were measured under  $\text{N}_2$ . When  $p(\text{O}_2)$  is reduced in the van der Pauw set-up most likely oxygen vacancies and electrons form. Thus, it is suggested that the investigated material is slightly p-type conducting. Once again deposition parameters play a crucial role. Thin films produced under 100 mTorr background pressure have the highest resistivity. Samples prepared under 500 mTorr and 900 mTorr exhibit nearly the same conductivity, nevertheless the higher the  $p(\text{O}_2)$  in the PLD chamber during film growth the lower the resistivity becomes. All thin films of this composition are less conductive

than the bulk specimen. A factor of 6.3 and 2.6 for  $R_{ABCD}/R_{BCDA}$  were obtained for the measurements of the 500 mTorr and 900 mTorr thin film under ambient air and  $N_2$ , resulting in small form factors of 0.79 and 0.92 (calculated using Equation 23). These high ratios are most probably caused by a combination of inhomogeneities in the prepared thin films and unideal shapes of the by hand cut samples. Nevertheless, the data can be used to get an impression of the resistivity of these two thin films. However, when comparing the various compositions this should be taken into account.

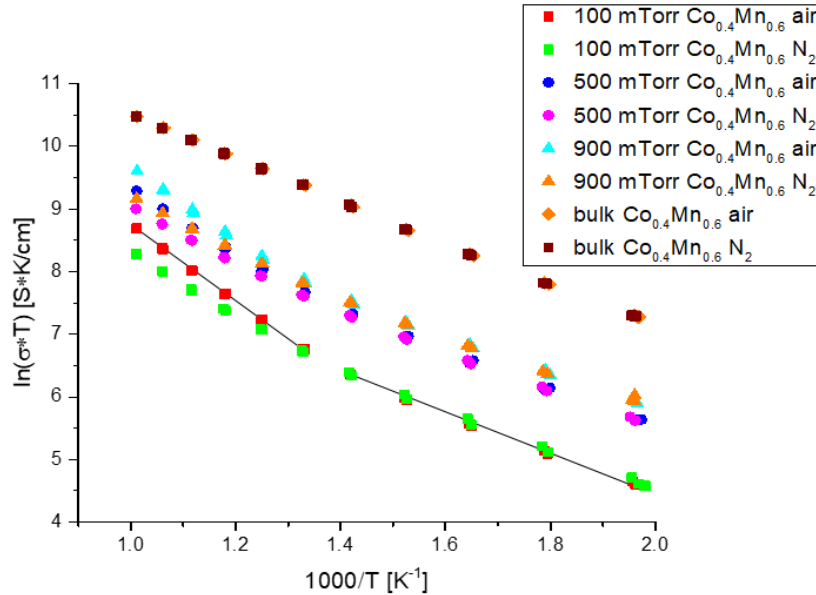


Figure 38: Arrhenius plot of the conductivity of  $LaCo_{0.4}Mn_{0.6}O_3$  thin films and corresponding bulk sample, measured under ambient atmosphere and  $N_2$  containing nominal 2 ppm  $O_2$

From the Arrhenius plot in Figure 38 two activation energies can be calculated for each specimen and measurement cycle. These are listed in Table 6 below.

Table 6: Activation energies of  $LaCo_{0.4}Mn_{0.6}O_3$  thin films measured under ambient atmosphere and  $N_2$  containing 10 ppm  $O_2$

Thin films with deposition parameters	$E_a$ [eV]
$LaCo_{0.4}Mn_{0.6}O_3$ 100 mTorr air low temp	0.27
$LaCo_{0.4}Mn_{0.6}O_3$ 100 mTorr air high temp	0.52
$LaCo_{0.4}Mn_{0.6}O_3$ 100 mTorr $N_2$ low temp	0.27
$LaCo_{0.4}Mn_{0.6}O_3$ 100 mTorr $N_2$ high temp	0.42
$LaCo_{0.4}Mn_{0.6}O_3$ 500 mTorr air low temp	0.26
$LaCo_{0.4}Mn_{0.6}O_3$ 500 mTorr air high temp	0.44
$LaCo_{0.4}Mn_{0.6}O_3$ 500 mTorr $N_2$ low temp	0.26
$LaCo_{0.4}Mn_{0.6}O_3$ 500 mTorr $N_2$ high temp	0.37
$LaCo_{0.4}Mn_{0.6}O_3$ 900 mTorr air low temp	0.25
$LaCo_{0.4}Mn_{0.6}O_3$ 900 mTorr air high temp	0.48
$LaCo_{0.4}Mn_{0.6}O_3$ 900 mTorr $N_2$ low temp	0.24

The activation energies of all measured thin films are in the range of 0.24 eV and 0.27 eV. The slopes of the linear fits below the transition point at ca. 460 °C do not differ significantly, they are independent of the background pressure during thin film deposition. The measurement atmosphere seems to play a negligible role as well. Moreover, these  $E_a$  are similar to the bulk values of 0.29 eV.

The slopes of the second fits at elevated temperatures however are connected to the  $p(O_2)$  in the van der Pauw set-up. Under ambient air higher activation energies are obtained than under N<sub>2</sub> atmosphere. Moreover, the higher the background pressure during thin film deposition the lower the activation energies above 460 °C becomes. None of the thin films shows a bulk like behavior over the whole investigated temperature range.

#### 4.4.4 LaCo<sub>0.6</sub>Mn<sub>0.4</sub>O<sub>3</sub> Thin Film Samples

Thin films with a composition of LaCo<sub>0.6</sub>Mn<sub>0.4</sub>O<sub>3</sub> were produced under 100 mTorr, 500 mTorr and 900 mTorr  $p(O_2)$  background pressure. Subsequently their conductivity was measured under ambient air and N<sub>2</sub> containing nominal 2 ppm O<sub>2</sub> by using the van der Pauw method. The Arrhenius plots of these measurements are shown in Figure 39.

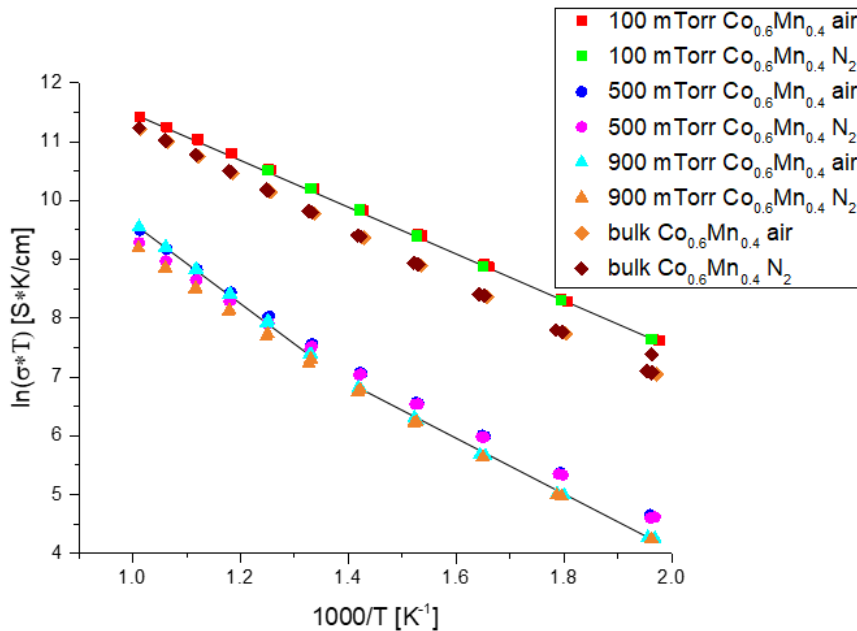


Figure 39: Arrhenius plots Van der Pauw measurements of LaCo<sub>0.6</sub>Mn<sub>0.4</sub>O<sub>3</sub> thin films

All thin films show a linear dependency of the  $\ln(\sigma \cdot T)$  on the reciprocal temperature in certain temperature ranges. The thickest sample, which was deposited under 100 mTorr  $p(O_2)$  has the lowest resistivity of all samples with the composition of LaCo<sub>0.6</sub>Mn<sub>0.4</sub>O<sub>3</sub>. It is very bulk like, due to the fact, that there is no bend in its data series and the established N<sub>2</sub> atmosphere was



not able to reduce it. The data obtained from the 100 mTorr thin film could be easily fitted, giving only one activation energy. An overview of the calculated  $E_a$  is given in Table 7 below.

The data series of the thin films deposited under 500 mTorr and 900 mTorr possess a bend at around 430 °C, with an increased slope above the transition point. Hence, two activation energies were calculated for each sample and measurement cycle. Moreover, the atmosphere in the van der Pauw set-up during the measurements has an impact on the conductivity. Above the bend, the resistivity of the thin films is increased, when measured under  $N_2$ . Thus, it is suggested that  $LaCo_{0.6}Mn_{0.4}O_3$  is a p-type semiconductor. Both specimens have nearly the same conductivity. At lower temperatures, the 500 mTorr sample is more conductive than the 900 mTorr under both atmospheres. Nevertheless, above the transition point the linear fit of the 900 mTorr sample measured under air is steeper than the slope of the 500 mTorr thin film, consequently at elevated temperatures the 900 mTorr has a higher conductivity under ambient air than the 500 mTorr specimen.

The obtained activation energies in Table 7 below, give an impression of the dependency of the conductivity from temperature.

Table 7: Activation energies of  $LaCo_{0.4}Mn_{0.6}O_3$  thin films measured under ambient atmosphere and  $N_2$  containing 2 ppm  $O_2$

Thin films with deposition parameters	$E_a$ [eV]
$LaCo_{0.6}Mn_{0.4}O_3$ 100 mTorr air	0.34
$LaCo_{0.6}Mn_{0.4}O_3$ 100 mTorr $N_2$	0.35
$LaCo_{0.6}Mn_{0.4}O_3$ 500 mTorr air low temp	0.38
$LaCo_{0.6}Mn_{0.4}O_3$ 500 mTorr air high temp	0.52
$LaCo_{0.6}Mn_{0.4}O_3$ 500 mTorr $N_2$ low temp	0.39
$LaCo_{0.6}Mn_{0.4}O_3$ 500 mTorr $N_2$ high temp	0.48
$LaCo_{0.6}Mn_{0.4}O_3$ 900 mTorr air low temp	0.40
$LaCo_{0.6}Mn_{0.4}O_3$ 900 mTorr air high temp	0.59
$LaCo_{0.6}Mn_{0.4}O_3$ 900 mTorr $N_2$ low temp	0.40
$LaCo_{0.4}Mn_{0.6}O_3$ 900 mTorr $N_2$ high temp	0.52

When the thin films were measured under ambient air or  $N_2$  atmosphere at temperatures below the transition point, hardly any difference in the activation energies can be seen.  $E_a$  differ by a maximum of 0.01 eV. However, at elevated temperatures above 430 °C the differences enlarged to 0.04 eV for the 500 mTorr and 0.07 eV for the 900 mTorr sample. With an  $E_a$  of 0.34 eV under ambient air respectively 0.35 eV under  $N_2$  atmosphere the 100 mTorr thin film even

exhibits lower activation energies than the bulk sample with the same composition. Moreover, the higher the background pressure during film growth the higher the activation energies become.

A comparison of the resistivity evolution with temperature of the  $\text{LaCo}_{0.4}\text{Mn}_{0.6}\text{O}_3$  and  $\text{LaCo}_{0.6}\text{Mn}_{0.4}\text{O}_3$  specimens and the mentioned dependency on the  $p(\text{O}_2)$  is shown in Figure 40 below.

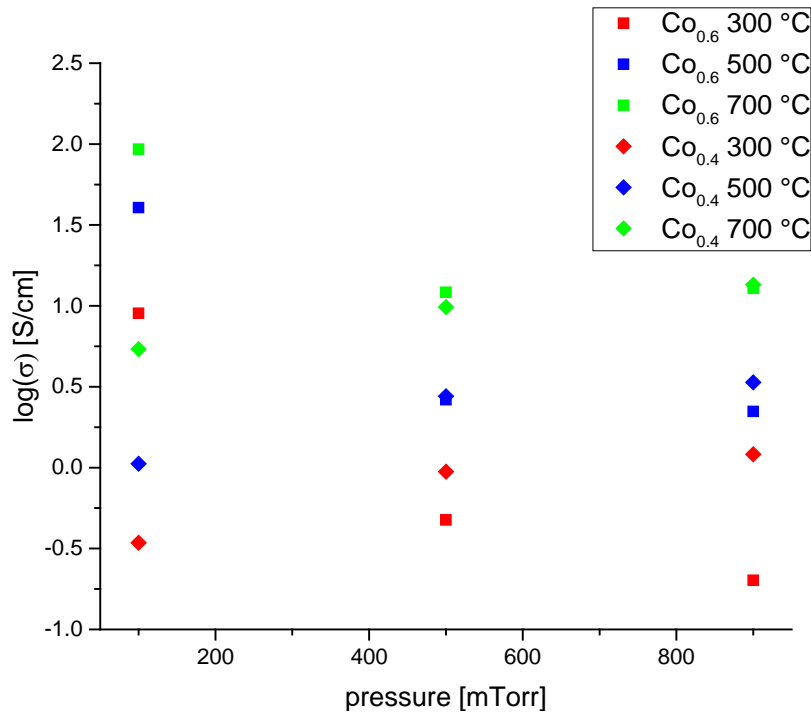


Figure 40: Resistivity comparison and evolution of  $\log(\sigma)$  with deposition  $p(\text{O}_2)$  of  $\text{LaCo}_{0.4}\text{Mn}_{0.6}\text{O}_3$  and  $\text{LaCo}_{0.6}\text{Mn}_{0.4}\text{O}_3$  thin films at 300 °C, 500 °C and 700 °C under ambient air

Considering the samples deposited under 100 mTorr background pressure thin films with a relative amount of Co of 0.6 are more conductive than those with 0.4 Co at the given temperatures in Figure 40. This tendency can be found in the bulk samples as well. An increased background pressure in the PLD chamber lead to a drop in the resistivity in  $\text{LaCo}_{0.4}\text{Mn}_{0.6}\text{O}_3$  specimens. On the other hand, in  $\text{LaCo}_{0.6}\text{Mn}_{0.4}\text{O}_3$  samples a decline of the conductivity at 500 mTorr is followed by a slight rise at 900 mTorr. Consequently at 500 mTorr and 900 mTorr the thin films of  $\text{LaCo}_{0.4}\text{Mn}_{0.6}\text{O}_3$  are more conductive than those of  $\text{LaCo}_{0.6}\text{Mn}_{0.4}\text{O}_3$ . At 500 mTorr both compositions still show nearly the same conductivity at 500 °C and 700 °C. As mentioned above, small inconsistencies occurred by measuring the conductivity of the  $\text{LaCo}_{0.4}\text{Mn}_{0.6}\text{O}_3$ . Hence this comparison has to be taken with a grain of salt.

## 4.5 Tracer Diffusion Measurements

### 4.5.1 LCM $^{18}\text{O}$ Tracer Depth Profiles

For a complete characterization, the diffusion of oxygen through the thin films has to be analyzed as well. Therefore, isotope exchange depth profiling experiments of the produced LCM thin films were made and the diffusion coefficients and surface exchange coefficients determined. Moreover, the impact of the deposition parameters and of the used substrates on the thin film properties will be discussed in the following chapters.

#### 4.5.1.1 LCM Samples Deposited with 1 Hz Repetition Rate

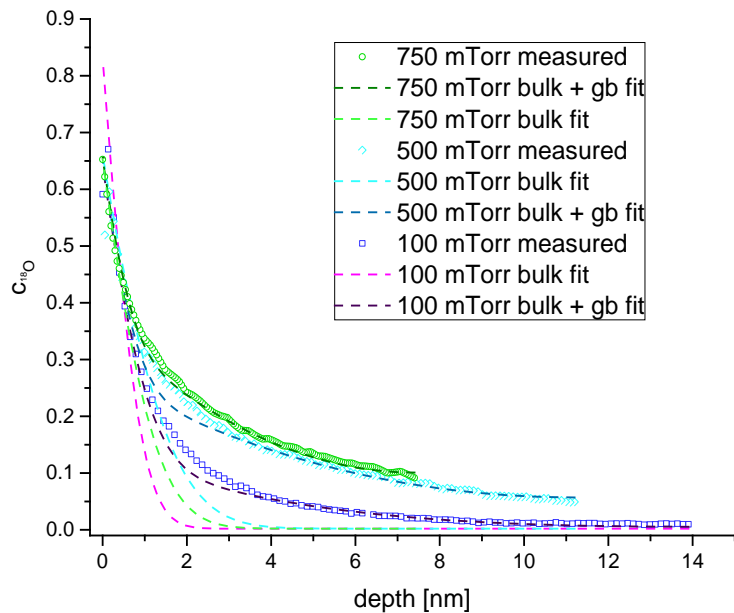


Figure 41: Tracer ion depth profiles of LCM 13, 15, 18 after diffusion at 573 °C for 3<sup>30</sup> hours

In Figure 41 tracer ion depth profiles of LCM thin films on LAO obtained at 573 °C for 3<sup>30</sup> hours, deposited with a rate of 1 Hz, for 20 min and under various  $p(\text{O}_2)$  are shown. With increasing oxygen partial pressure, the produced thin films were getting thinner. In addition, sample LCM 15 and LCM 18 deposited under 750 mTorr and 500 mTorr show nearly the same diffusivity for  $^{18}\text{O}$ . LCM 13 (100 mTorr) has a reduced diffusivity, the relative amount of  $^{18}\text{O}$  drops much faster. Nevertheless, in all shown thin films,  $^{18}\text{O}$  diffused all the way through LCM to the LAO substrate. The  $^{18}\text{O}$  concentration at the interface of LCM and LAO is elevated compared to the natural relative amount (0.25 %) of this oxygen isotope.  $^{17}\text{O}$  (natural abundance 0.038 %) was not considered in this and the following ToF-SIMS measurements.[9]

In all samples shown in Figure 41, grain boundary diffusion plays probably a vital role. It was not possible to fit the measured profiles just with a bulk diffusion coefficient ( $D^*_g$ ) and a bulk surface exchange coefficient ( $k^*_g$ ). In COMSOL Multiphysics® Modeling Software (COMSOL Inc., Germany), which was used for the fitting process,  $D^*_{gb}$  and  $k^*_{gb}$  for the grain boundary diffusion coefficient and the grain boundary surface exchange coefficient had to be implemented. Even though the fitting curves obtained with grain diffusion only matched to the measured values during the first 1 nm, the fit curve drops far too fast to the natural  $^{18}\text{O}$  level. Considering a faster grain boundary diffusion, the quality of the fits became much better. Diffusion and surface exchange coefficients are compared in Figure 43. Nevertheless, a perfect match of fit and measurement data was not obtainable, a discrepancy was always existing. In a depth range of 1.5 nm to 3 nm the disagreement became obvious. A clear explanation could not be found during the thesis, a plausible reason for these differences could be, that in the ToF-SIMS the filmions were intermixed during sputtering and consequently the horizontal resolution was reduced. Hence the disagreement could simply be the consequence of the used measurement method.

In Table 8 an overview of the calculated  $D^*_g$ ,  $D^*_{gb}$ ,  $k^*_g$ ,  $k^*_{gb}$  and the grain size, used for the fittings, is given. The bulk diffusion coefficients of LSC (exchange temperature 400 °C) obtained by Kubicek et al. is  $8.0 \cdot 10^{-20} \text{ m}^2/\text{s}$  [9] and therefore it is exceeding even the grain boundary diffusion coefficients of the discussed samples at 573 °C by a factor of at least 26. The  $k^*_g$  (400 °C exchange temperature) of LSC is  $9,67 \cdot 10^{-13}$  [9], thus lies between the  $k^*_g$  and  $k^*_{gb}$  of the 1 Hz LCM samples. Moreover, a strong strain dependency can be observed in LSC. It exhibit much higher surface exchange and diffusion coefficient when deposited on STO, due to tensile strain which is introduced into the thin film due to the misfit of the cell parameters of the thin film and the substrate. [9]

In LSM100 grain boundary diffusion plays a key role as well. Considering an exchange temperature of 600 °C and a grain diameter of 45 nm,  $D^*_g$  is in a range of  $4 \cdot 10^{-21} \text{ m}^2/\text{s}$ ,  $D^*_{gb}$  of  $4 \cdot 10^{-18} \text{ m}^2/\text{s}$ ,  $k^*_g$  of  $4 \cdot 10^{-13} \text{ m/s}$  and  $k^*_{gb}$  of  $2 \cdot 10^{-11} \text{ m/s}$  in LSM100.[77] The bulk diffusion is by a factor of 100 faster than in LCM, the  $D^*_{gb}$  differ by three orders of magnitude. This large difference can also not be a single consequence of the rather small grain sizes used in these fits. However, surface exchange in bulk and grain boundary of LSM and LCM are quite similar, the  $k^*$  values just differ by a factor of ca. 10.

As mentioned before, grain boundaries play a vital role in the investigated samples, thus also the grain size is a crucial factor in the fitting process. It is decreasing with an increasing  $p(\text{O}_2)$

in the PLD chamber during thin film growth. As consequence of a decreasing grain size the ratio between bulk and boundary is getting smaller and therefore the grain boundary diffusion is more pronounced.

Table 8: Grain size,  $D^*$  and  $k^*$  values of the LCM thin films deposited with 1 Hz

1Hz samples	$p(O_2)$ [mTorr]	$D^*_g$ [ $m^2/s$ ]	$D^*_{gb}$ [ $m^2/s$ ]	$k^*_g$ [m/s]	$k^*_{gb}$ [m/s]	grain size [nm]
LCM 13_1	100	6.31E-23	2.51E-21	2.51E-14	4.01E-12	9.6
LCM 13_a	100	4.30E-23	1.90E-21	6.85E-14	5.36E-12	11.6
LCM 18	500	2.50E-23	3.05E-21	4.40E-14	3.45E-12	4.4
LCM 15	750	1.90E-23	1.50E-21	3.00E-14	1.70E-11	3.0

To sum up, the diffusion of the tracer ions is based on grain and grain boundary diffusion. This is a strong indication for thin films which are not single crystalline epitaxial, but polycrystalline oriented and the grain size plays a crucial role in the diffusion process (compare Figure 45).

The diffusion through LSM thin films on LAO is even faster at an exchange temperature of 400 °C. Comparing LSM and LCM at nearly the same exchange temperature, LCM prepared with 1 Hz deposition rate has lower grain and grain boundary diffusion and surface exchange coefficients.

#### 4.5.1.2 LCM Samples Deposited with 5 Hz Repetition Rate

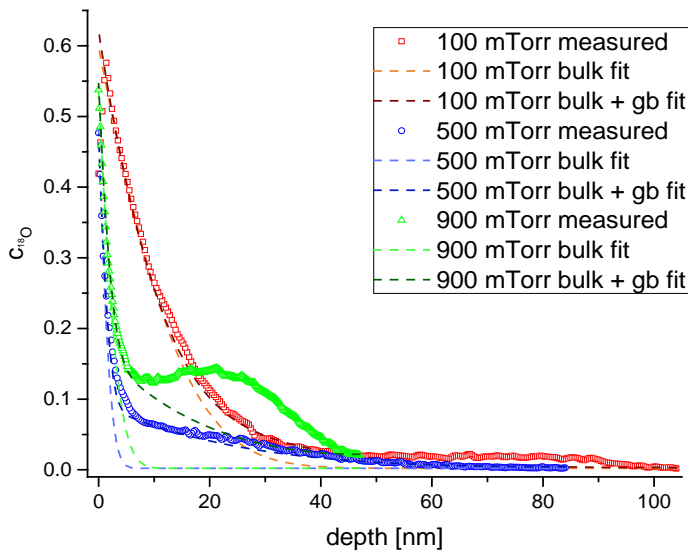


Figure 42: Tracer ion depth profiles of LCM 19, 20, 21 after diffusion at 600 °C for 15<sup>19</sup> hours

In the first part of chapter 4.5.1, the properties of LCM samples deposited with 1 Hz repetition rate were discussed. In the second part, the characteristics of the thin films LCM 19, 20 and 21 are analyzed. These were grown in 30 min with a deposition rate of 5 Hz, the profiles are shown

in Figure 42. Once again grain boundary diffusion must be considered in the fitting process. However, additionally an increase of the oxygen partial pressure in the PLD chamber leads to a third diffusion process, which is most pronounced in LCM 21 (900 mTorr  $p(\text{O}_2)$ , green data series in Figure 42). Apart from these uphill features between ca. 8 nm and 44 nm the sample LCM 20 and LCM 21 show a quite similar diffusivity. LCM 19 (red data series) has the highest bulk diffusivity and a shallow uphill part in the tail of its isotope tracer depth profile, between ca. 55 nm and 90 nm. A rising dislocation concentration could be an explanation for this feature.

A change to an ordered perovskite structure could be the reason for reduced diffusivity in LCM 20 and LCM 21.[25] As described in chapter 2, ordered B-site structures can be realized by performing PLD deposition under high  $p(\text{O}_2)$ .[15, 23] Unfortunately, it was not possible to verify such perovskite-structures in the investigated LCM samples yet.

The obtained diffusion coefficients and surface exchange coefficients are shown in Table 9 below.

Table 9: Grain size,  $D^*$  and  $k^*$  values of the samples deposited with 5 Hz

5Hz samples	$p(\text{O}_2)$ [mTorr]	$D^*_g$ [ $\text{m}^2/\text{s}$ ]	$D^*_{gb}$ [ $\text{m}^2/\text{s}$ ]	$k^*_g$ [m/s]	$k^*_{gb}$ [m/s]	grain size [nm]
LCM 19_1	100	1.40E-21	7.50E-20	2.25E-13	1.00E-12	28.0
LCM 19b	100	1.14E-21	1.65E-20	2.00E-13	2.05E-12	20.0
LCM 20	500	3.52E-23	2.20E-20	1.64E-14	1.38E-12	16.5
LCM 21_1	900	6.00E-23	1.65E-20	2.81E-14	8.60E-13	9.0
LCM 21b_1	900	4.50E-23	1.40E-20	2.70E-14	1.09E-12	7.5

The grain size is decreasing with increasing  $p(\text{O}_2)$  during the thin film preparation.  $D^*_g$  decreases dramatically for LCM samples deposited under higher background pressure. In contrast, grain boundary diffusion is nearly constant and not really affected by the used  $p(\text{O}_2)$  during the PLD process. The surface exchange coefficients show the same tendency, in an alleviated way. Thin films prepared under 900 mTorr  $p(\text{O}_2)$  have the worst diffusivity and smallest grain sizes. The diffusion coefficient of LSC at 400 °C exceeds  $D^*_{gb}$  of the 5 Hz sample at 600 °C as well, however the difference is not as pronounced as between LSC and the 1 Hz samples. The surface exchange coefficient is again between  $k^*_g$  and  $k^*_{gb}$  of the 5 Hz thin films.

$D^*_g$  and  $k^*_g$  of LSM are in the range of  $D^*_g$  and  $k^*_g$  of LCM 19, they just differ by a factor of around 3 respectively of 2. However, the rest of the 5 Hz LCM samples have a lower bulk diffusion and bulk surface exchange coefficients than LSM at 600°C. When comparing

the grain boundary diffusivities, it is obvious that oxygen incorporates/diffuse faster in/through the grain boundaries of LSC.

#### 4.5.1.3 1 Hz and 5 Hz Deposition Rate, Comparison of $D^*$ and $k^*$ Values

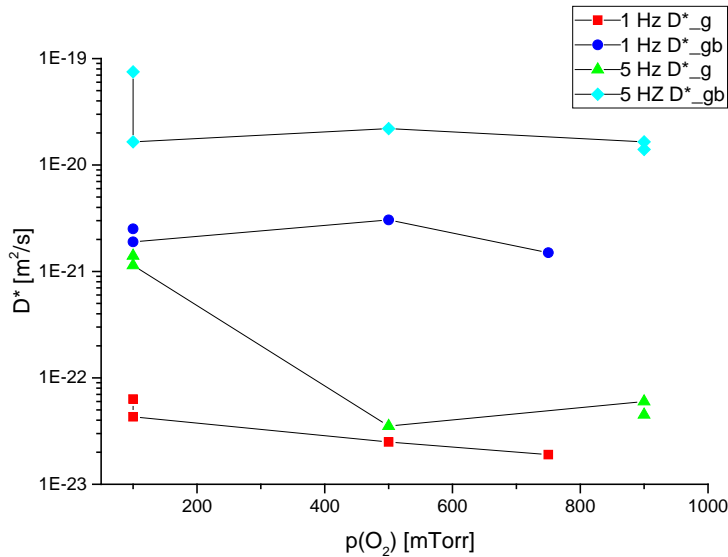


Figure 43:  $D^*_g$  and  $D^*_{gb}$  of LCM thin films on LAO at 573 °C (1 Hz samples) and 600 °C (5 Hz samples)

In 5 Hz LCM thin films,  $D^*_{gb}$  values are around one order of magnitude higher than in 1 Hz samples. They stay nearly constant, when the  $p(O_2)$  during deposition is increased. On the other hand, the  $D^*_g$  values are decreasing with increasing  $p(O_2)$ . Moreover, once again the vital role of grain boundary diffusion is shown, since both the 1 Hz and 5 Hz  $D^*_{gb}$  coefficients are significant higher than the corresponding  $D^*_g$  coefficients, they differ by a factor of 10 to 100. The evolution of the different diffusion coefficients is shown in Figure 43.

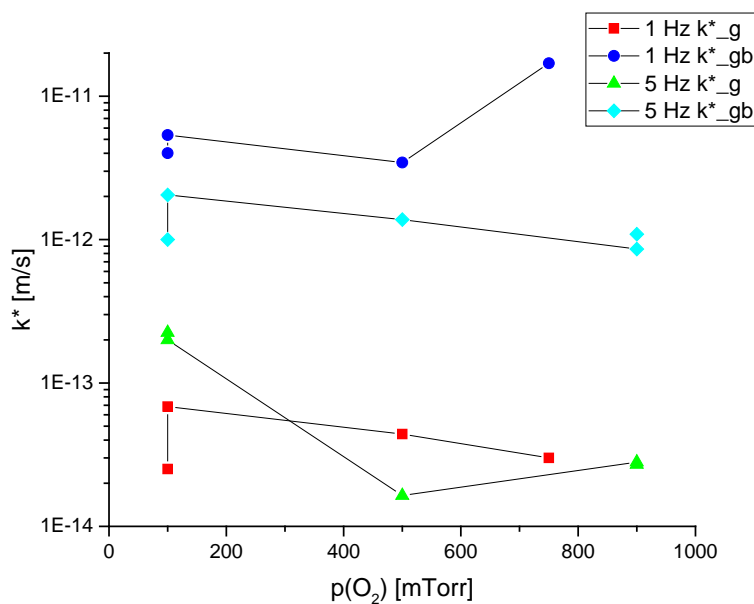


Figure 44:  $k^*_g$  and  $k^*_{gb}$  of LCM thin films on LAO at 573 °C (1 Hz samples) and 600 °C (5 Hz samples)

In Figure 44 the change of the LCM samples  $k^*_g$  and  $k^*_{gb}$  are sketched. The grain boundary surface exchange coefficients are higher than the bulk  $k^*_g$ . 1 Hz  $k^*_{gb}$  values are above the 5 Hz  $k^*_{gb}$  values. In general, all values are decreasing with increasing  $p(O_2)$ , there are just two exceptions. Both the 5 Hz and the 1 Hz series show a slightly increase in  $k^*_{gb}$  (1 Hz) respectively  $k^*_g$  (5 Hz) at each of their highest  $p(O_2)$ , used for deposition.

#### 4.5.1.4 Grain Size Dependency on $p(O_2)$ and Quality of the Fits

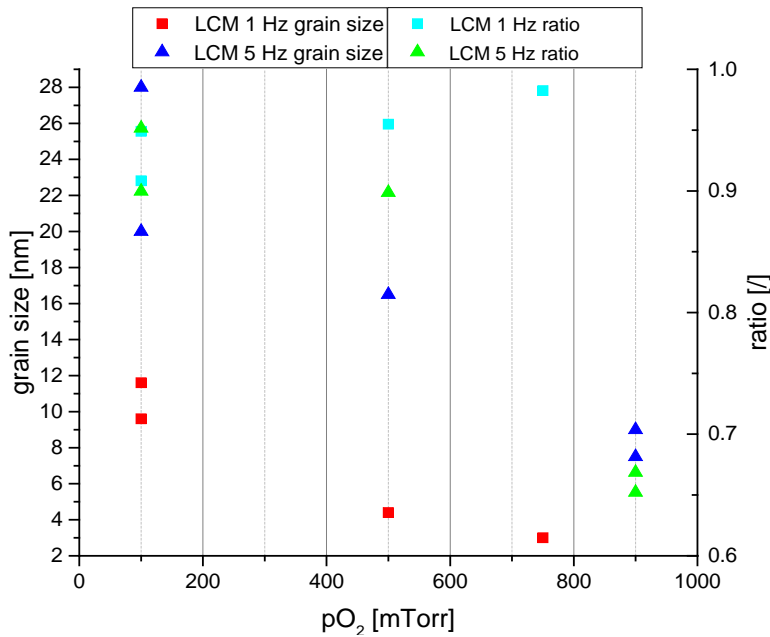


Figure 45: Grain size and fit quality evolution with increasing  $p(O_2)$  during thin film growth

The quality of a fit respectively the match between fitted and measured curve can be described through the ratio of the integrals of the measured isotope exchange depth profiles and the fitted profiles. In the case of a perfect match both areas should be the same and therefore the ratio is one. Otherwise if the fit is bad - the ratio is smaller. There is no perfect fit shown in Figure 45, nevertheless the ratios of the 1 Hz samples are always above 0.9 and even increasing, reaching a maximum at 750 mTorr  $p(O_2)$  for the bulk + gb fits. In Figure 41 the discrepancy between fitting curves and measured relative  $^{18}O$  concentration can be seen. Performing the bulk + gb fits on the 5 Hz thin films the obtained ratio is first slightly decreasing and then plummets to around 0.67. Both the slight decrease and the massive decline in the fit quality are a consequence of the upcoming additional diffusion process described in chapter 4.5.1.2.

Another key factor in grain boundary diffusion is shown in Figure 45 too, the dependency of the grain size on the deposition parameter. In both data series, the grain size is decreasing with rising  $p(O_2)$ . At all oxygen partial pressures, the 5 Hz samples exhibit greater grain sizes than the 1 Hz samples.



## 4.5.2 Strain Effect for Oxygen Diffusion

As mentioned in chapter 3.2 LCCM, thin films were deposited on STO and LAO to investigate strain effect on the oxygen diffusion. Such strain effects are known and described in literature for LSC thin films.[9] In the following graphs, Figure 46 and Figure 47, two ion tracer depth profiles are shown as examples. Both thin films were deposited with 1 Hz under 0.04 mbar  $p(O_2)$  and the followed  $^{18}O$  exchange experiment took place over night. They show an extremely high relative concentration of  $^{18}O$  and a kind of plateau was formed. In the fitting process, just bulk diffusion was taken into account. Thus, only the first part of the fitted curve and the measured values matches in both graphs. When comparing LCCM and LCM films the bulk diffusion coefficient is named  $D^*_g$  in any other context the notation  $D^*$  is sufficient.

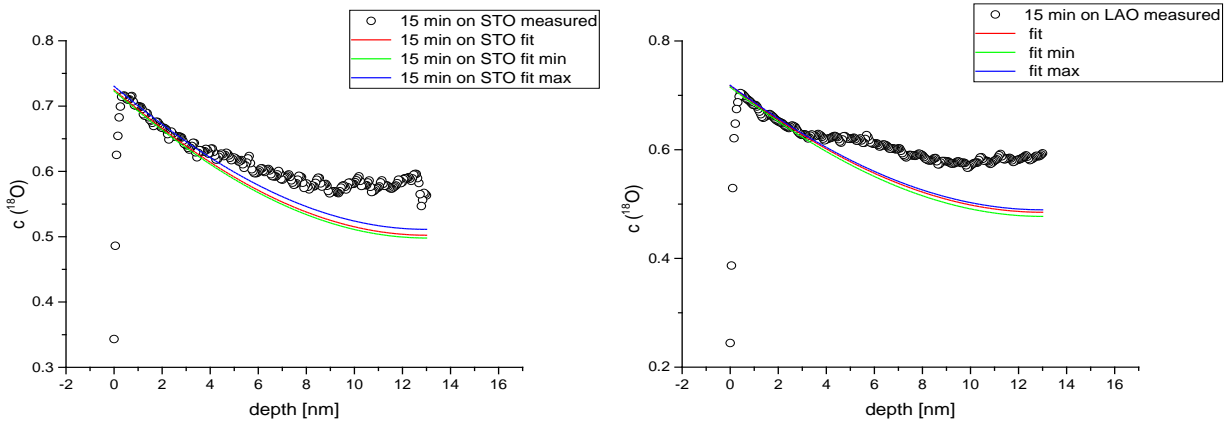


Figure 47:  $^{18}O$  tracer depth profile of LCCM on STO at 600 °C

Figure 46:  $^{18}O$  tracer depth profile of LCCM on LAO at 600 °C

An overview of the obtained  $D^*_g$  and  $k^*_g$  values is given Figure 46 and Figure 47. Since the oxygen partial pressure was mostly higher during LCM thin film growth (min. 100 mTorr), it is hard to compare the bulk diffusions of LCM and LCCM. Nevertheless, if we do so, minimum one order of magnitude difference is revealed in  $D^*_g$  and  $k^*_g$  coefficients between the 1 Hz LCM samples and the LCCM thin films. LCCM possess higher bulk diffusion and surface exchange coefficients, which suggests that either a disorder in the perovskite structure and/or a higher oxygen vacancy concentration resulted from the Ca A-site doping is present.

Table 10:  $D^*_g$  and  $k^*_g$  values obtained from LCCM thin films at 600 °C

deposition time LAO [min]	$D^*_g$ [m <sup>2</sup> /s]	$k^*_g$ [m/s]	deposition time STO [min]	$D^*_g$ [m <sup>2</sup> /s]	$k^*_g$ [m/s]
5	1.27E-21	1.25E-13	15	2.58E-21	3.28E-13
15	2.46E-21	3.16E-13	40	1.65E-20	1.29E-12
40	1.61E-20	1.13E-12	70	3.59E-20	2.27E-12
70	2.75E-21	4.95E-13			

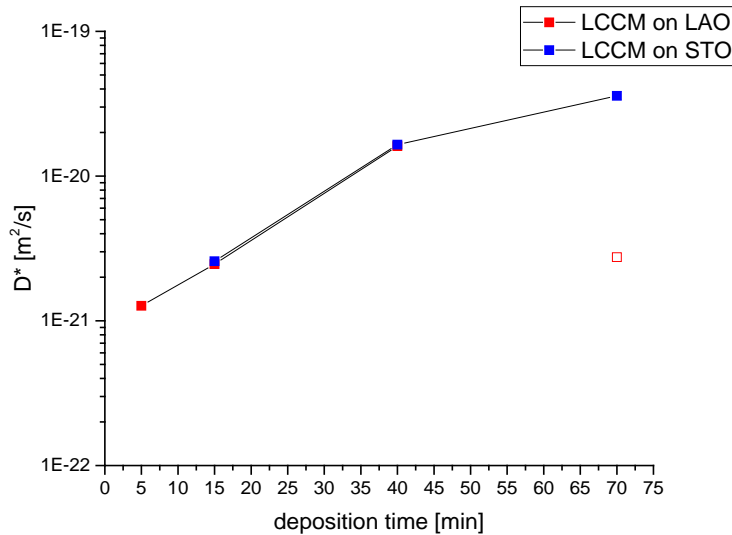


Figure 48:  $D^*_g$  LCCM samples obtained at 600 °C

The LCCM target material has the pseudosquare lattice parameters  $a=b$  of 3.839 Å, considering the facet between the axial vectors  $a$  and  $b$ . LAO and STO have different pseudocubic cell parameters: 3.793 Å and 3.905 Å (provided by CrysTec GmbH Kristalltechnologie, Germany on their data sheets). The pseudosquare lattice constant of LCCM lies between these, hence assuming a growth direction along the  $c$ -axis vector either tensile or compressive planar strain should be introduced by the LAO/STO substrates. Differences in strain can impact diffusion and surface exchange coefficients, as reported in literature.[9] The bulk diffusion coefficient evolution of the thin films deposited on LAO or STO against deposition time is shown in Figure 48.

Even though the films were deposited on different substrates the LCCM samples show nearly the same  $D^*$  values for films with the same thickness. Hence the substrates do not introduce strain in the films or strain does not have any influence on the diffusivity of LCCM. Strain should decrease with increasing thickness, since more and more dislocations are formed and these are able to release the strain based on the lattice mismatch between thin film and substrate. Considering Figure 48, the thicker the thin films the higher  $D^*$  of both data series become. Only the  $D^*$  coefficient of the thickest film on LAO does not follow this trend. From this particular sample only one isotope depth profile was measured, hence another measurement is needed to determine the actual  $D^*$  value and subsequently reveal the real development. Considering both, it is possible that strain is introduced and has an impact on the diffusivity, but the kind of strain is irrelevant. Another more plausible explanation could be that strain has no or only a negligible impact and the faster diffusion of oxygen ions through the thin films is due to a fast diffusion through the dislocations.

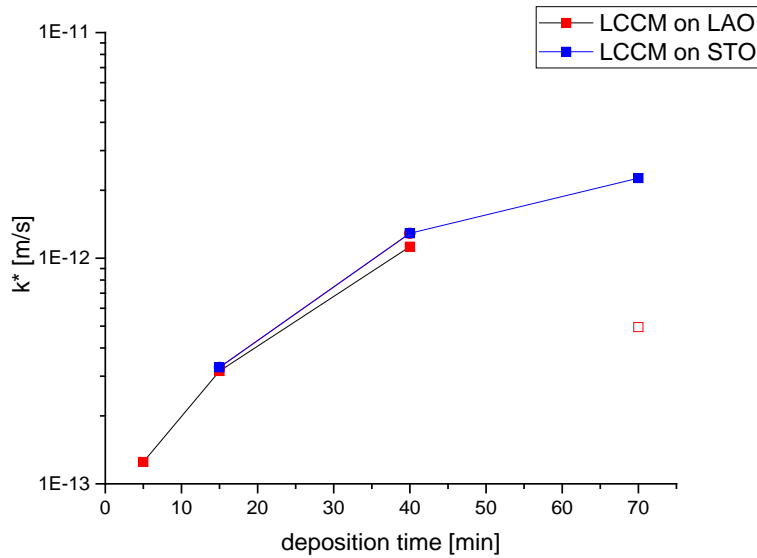


Figure 49:  $k^*_g$  LCCM samples obtained at 600 °C

The surface exchange coefficients  $k^*$  in Figure 49 show the same behavior as the  $D^*$  coefficients. There is hardly no difference between the two different substrate materials, nevertheless an enlargement can be seen with an increasing thickness of the thin films. For 70 min deposition time LCCM sample on LAO show a decreased  $k^*$  value, as mentioned above an additional experiment is necessary at this point.

#### 4.6 Impedance Spectroscopy of LCM Microelectrodes

Finally, the ionic area specific resistance of LCM thin films is going to be discussed. The ionic resistivity can be determined by using impedance spectroscopy on a solid electrolyte material like YSZ with microelectrodes of the investigated material (LCM) on one side (working electrodes) and a thin film of the same material on the other (counter electrode).

##### 4.6.1 LCM 05

The impedance spectra of LCM 05 were obtained on the measurement set-up II-Pot, described in chapter 3.8. For the fitting process by Z-view (Scribner Associates Inc., North Carolina) the equivalent circuit shown in Figure 50 was used. The fitting is performed only for the low frequency part of the obtained spectra, since the electrolyte constant phase element is missing. Impedance spectroscopy was used to determine the area specific resistance of the prepared microelectrodes. The measured impedance data consists out of a real and an imaginary term, which were plotted in a so-called Nyquist plot. On the x-axis the real component and on the y-axis the imaginary component of the complex resistance is plotted.

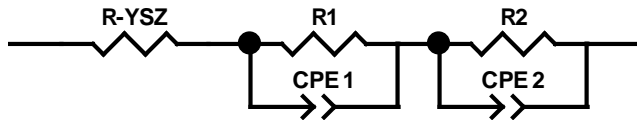


Figure 50: Equivalent circuit

In the equivalent circuit (Figure 50) R-YSZ represents the resistance of the electrolyte (YSZ single crystal) between working and counter electrode. It is an electronically insulating and ionic conductive material. The two following resistor–constant phase element circuits presumably describe the oxygen incorporation at the surface of the thin film and the interface between LCM and the electrolyte. In Figure 51 the produced circular microelectrodes of LCM 05 with three different diameters are shown.



Figure 51: Microelectrodes LCM 05 on YSZ (001) single crystal

The produced microelectrodes in Figure 51 are all smaller than the area coated by the photoresist after UV-lithography. The difference is just in the range of 3 μm and does not vary a lot, thus the electrodes can be used for impedance spectroscopy. On some of them parts of the photoresist remained, these electrodes were not used for the measurements. From the recorded spectra, the area specific resistances (ASR) were calculated and the obtained values plotted in Figure 52.

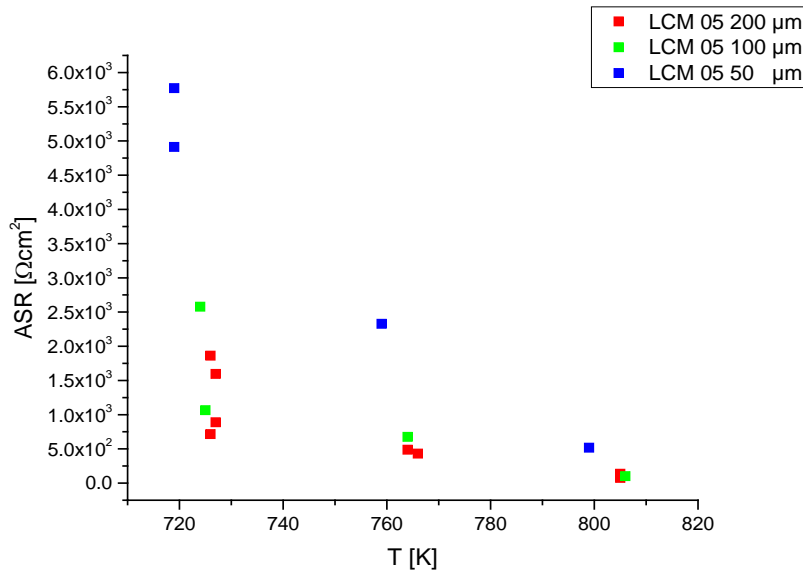


Figure 52: Area specific resistance of LCM 05 microelectrodes,  $T$  calculated from YSZ conductivity

The area specific resistivity was obtained by multiplying the sum of  $R_1$  and  $R_2$  by the surface area of the electrodes. Higher temperatures lead to an decrease of all three resistances, due to better ionic conductivity in YSZ/LCM and enhanced kinetics at the electrodes surfaces. In the case of a limitation connected to the surface of the electrodes the ASR at a specific temperature should be the same for all electrode sizes. The electrodes with diameters of nearly 100  $\mu\text{m}$  and 200  $\mu\text{m}$  meet this criteria quite well, eventhough two groups of data points can be observed at around 725 K. Here the same electrode was measured at the beginning of the measurement series and at the end (100  $\mu\text{m}$  diameter), respectively each time twice (200  $\mu\text{m}$ ). The 50  $\mu\text{m}$  electrode does not fit at all, its ASR is far to high. Degradation can be a possilbe explanation, since small electrodes degrade much faster than big ones in the used set-up.

The various ASRs of different electrodes with the same size at a set temperature of 600 °C are shown in Figure 53. Due to the way of heating, smaller electrodes might be a bit cooler than bigger ones [78], nevertheless in this graph electrodes with the same size are compared, so this minor inaccuracy is negligible.

Two out of three electrodes form a pair with similar area specific resistivities. Even the ASRs of different electrode sizes are in a similar range. However reproducible results were hard to achieve in this set-up, due to degradation and the diverse behaviour of elcetrodes of the same size.

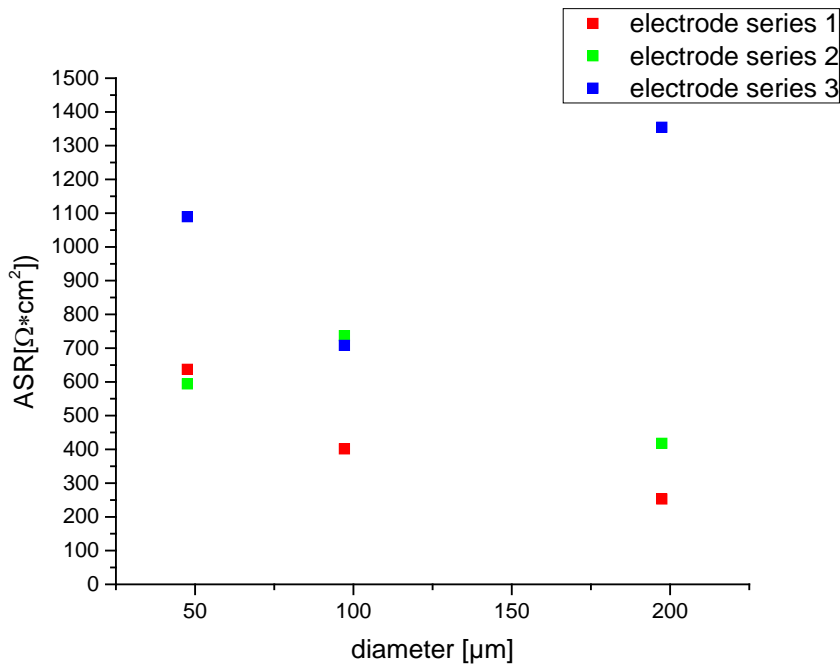


Figure 53: ASR of three different electrodes of each size at a set temperature of 600 °C

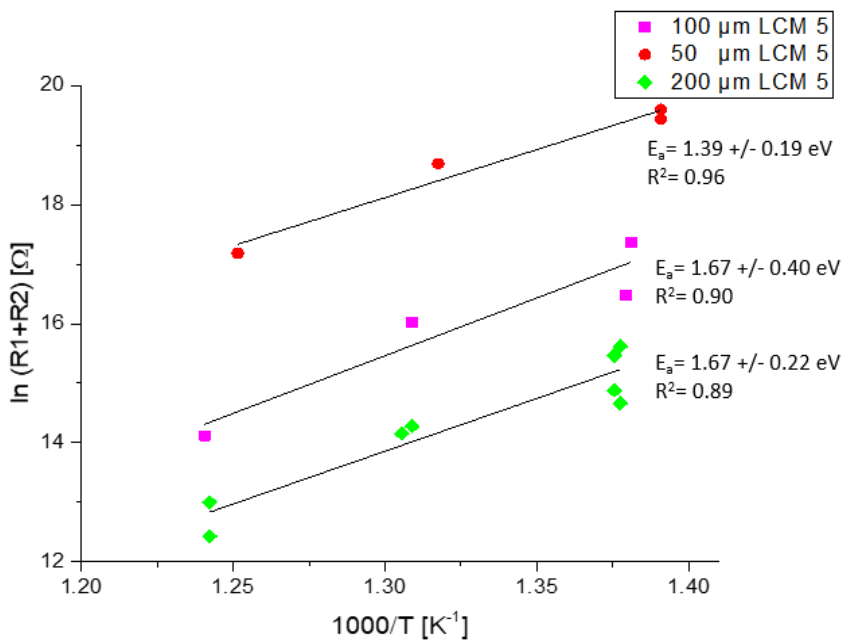


Figure 54: Calculated activation energies of LCM 05

To complete the picture of sample LCM 05, the activation energies of the microelectrodes were calculated from an Arrhenius plot. Thereby the natural logarithm of the sum of  $R_1$  and  $R_2$  (the polarization resistance) is plotted against the inverse temperature. The activation energy is then calculated by multiplying the slope of the regression line by the Boltzmann constant. The regression line fits quite well, the  $R^2$  are always greater or equal 0.89 and the obtained activation energies are in the range of 1.39 eV and 1.67 eV. In comparison  $\text{La}_{0.8}\text{Sr}_{0.2}\text{MnO}_3$  has activation

energies of 1.25 eV- 1.58 eV for finger-type electrodes and 0.95 eV +/- 0.02 eV for circular microelectrodes in a similar temperature regime.[50]

In conclusion, a first idea of the polarization resistance can be obtained but the electrodes suffer from degradation. The differences in the polarization resistance between electrodes of the same size are evident. As a consequence, new electrodes with diameters of 350  $\mu\text{m}$  to 150  $\mu\text{m}$  were prepared and the measurement set-up changed to a MicroMacro set-up, where degradation should be less pronounced or even not present at all.

#### 4.6.2 LCM 06 and LCM 07

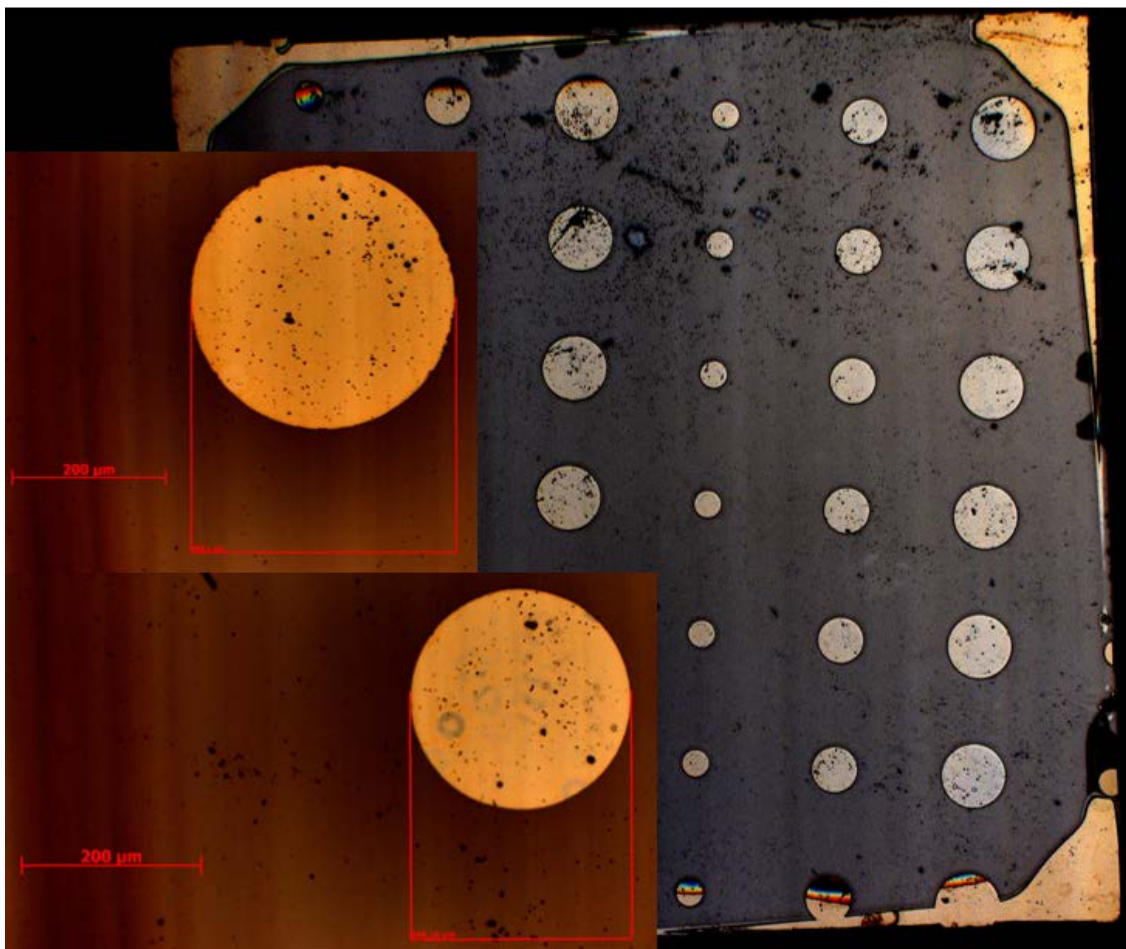


Figure 55: Microelectrodes of LCM 07 on YSZ (001) single crystals

In Figure 55 the sample LCM 07 with its microelectrodes on top is shown. The black grains on most of the electrodes are most likely tiny amounts of photoresist. All electrodes have a circular shape and nearly the desired diameters of 350  $\mu\text{m}$ , 250  $\mu\text{m}$  and 150  $\mu\text{m}$ . The measurements were carried out at the 250  $\mu\text{m}$  and 350  $\mu\text{m}$  electrodes. Thereby the sample were placed in a quartz sword and subsequently heated in a tube furnace (compare chapter 3.8). The obtained impedance spectra of a 350  $\mu\text{m}$  electrode during a temperature cycle are shown in Figure 56.

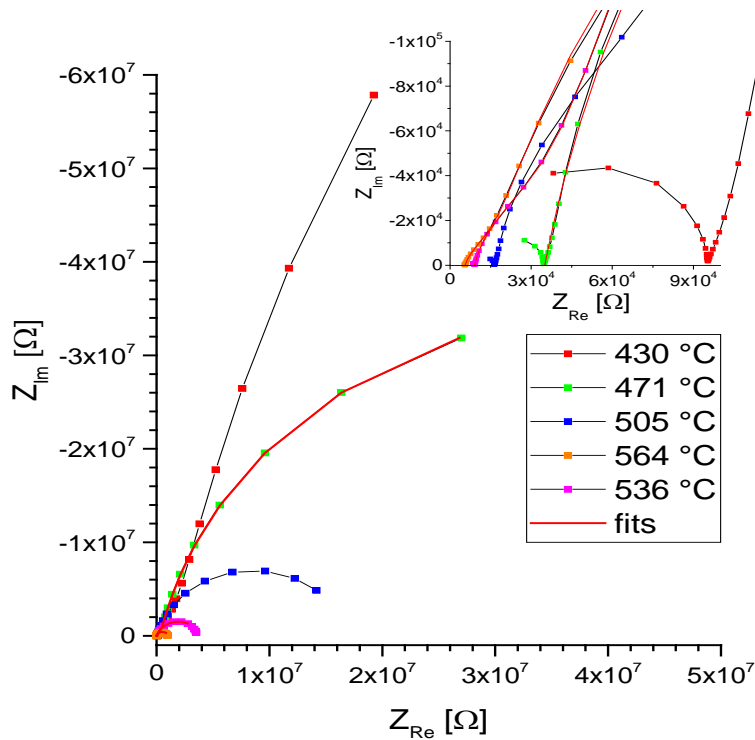


Figure 56: Impedance spectra LCM 07 temperature cycles (heating up)

A typical impedance spectrum (Figure 56) consists of two semicircles, the first one describes the electrolyte YSZ and the second one is from the working electrode.

The second semicircle is deformed and had to be fitted with two resistance and constant phase element circuits, see Figure 50. Like in chapter 4.6.1 the polarization resistance of the working electrode is the sum of R1 and R2. R-YSZ represents the resistance of the electrolyte. With increasing temperature, all resistances decrease and the semicircles are flattened.

Plotting  $\ln(R1+R2)$  against the inverse temperature the activation energies can be calculated. Interestingly, differences in the resistances during heating and cooling of the samples appeared particularly during the first heating and cooling cycle (250  $\mu\text{m}$  electrode). The Arrhenius plots are illustrated in Figure 57.



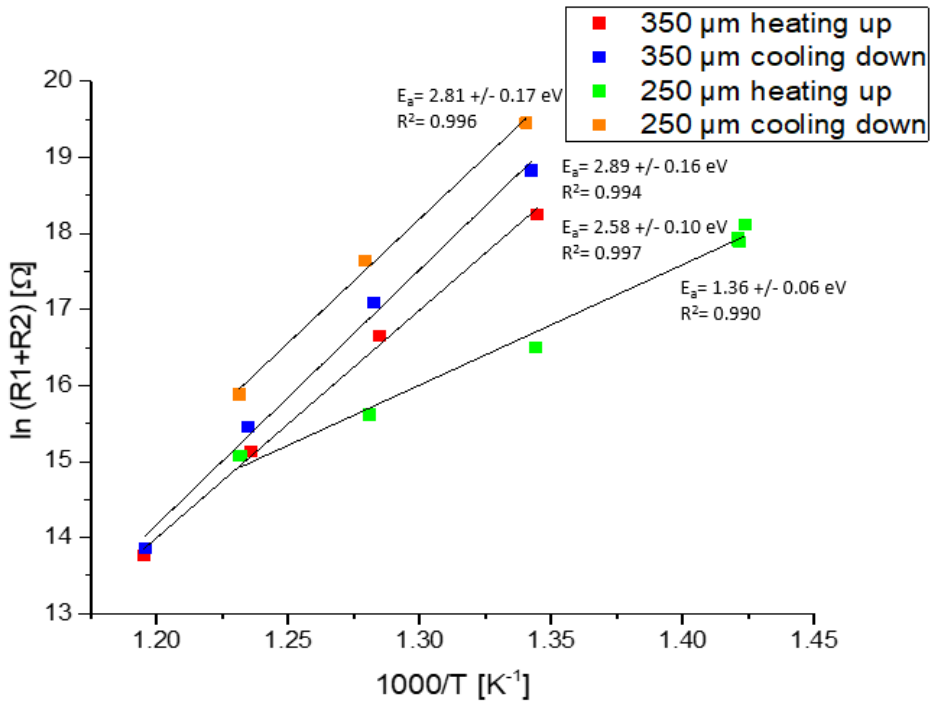


Figure 57: Arrhenius plot of LCM 07 for the first heating/cooling cycle on the 250  $\mu\text{m}$  electrode and the second cycle on the 350  $\mu\text{m}$  electrode

Before the first heating above 550  $^{\circ}\text{C}$ ,  $E_a$  of LCM 07 is in the range of those from the impedance measurements at the II-Pot set-up (LCM 05). Nevertheless, after reaching the temperature maximum the resistance and  $E_a$  are both increasing tremendously. The calculated  $E_a$  of the 250  $\mu\text{m}$  electrode rise from 1.36  $\pm$  0.06 eV for the first heating phase to 2,81  $\pm$  0,17 eV for the cooling phase. Changing to the bigger 350  $\mu\text{m}$  electrode lead to a moderate decrease of the resistance compared to these obtained from the 250  $\mu\text{m}$  electrode during the cooling phase. At intermediate temperatures, still higher resistances were measured during the 350  $\mu\text{m}$  heating phase than for the 250  $\mu\text{m}$  heating phase. The  $E_a$  stayed in the same range and only a slight discrepancy between heating up (2.58  $\pm$  0.10 eV) and cooling down (2.81  $\pm$  0.17 eV) can be seen.

After these first measurements and the observed misfit between LCM 05 and LCM 07, the question arises, if there are still degradation processes existing or if a change of the sample causes the increase in the  $E_a$  and resistance.

Consequently, an overnight degradation measurement was carried out. For that impedance spectra from 10<sup>6</sup> Hz to 0.01 Hz were recorded for a 350  $\mu\text{m}$  electrode of the sample LCM 06 at a temperature of ca. 593  $^{\circ}\text{C}$ . In Figure 58 the result of a degradation measurement is pictured. Selected impedance spectra of a degradation measurement of the 350  $\mu\text{m}$  electrode illustrate the increasing resistance of the second semicircle. Compared to the rise of the microelectrode resistance the change of the YSZ resistance can be neglected (probably due to slight temperature

variations). Even though degradation should not be present in this set-up a moderate degradation can be observed, the resistance nearly doubled overnight. A link to the used photo resist during the micro structuring of the samples is supposed but could not be proven during the thesis.

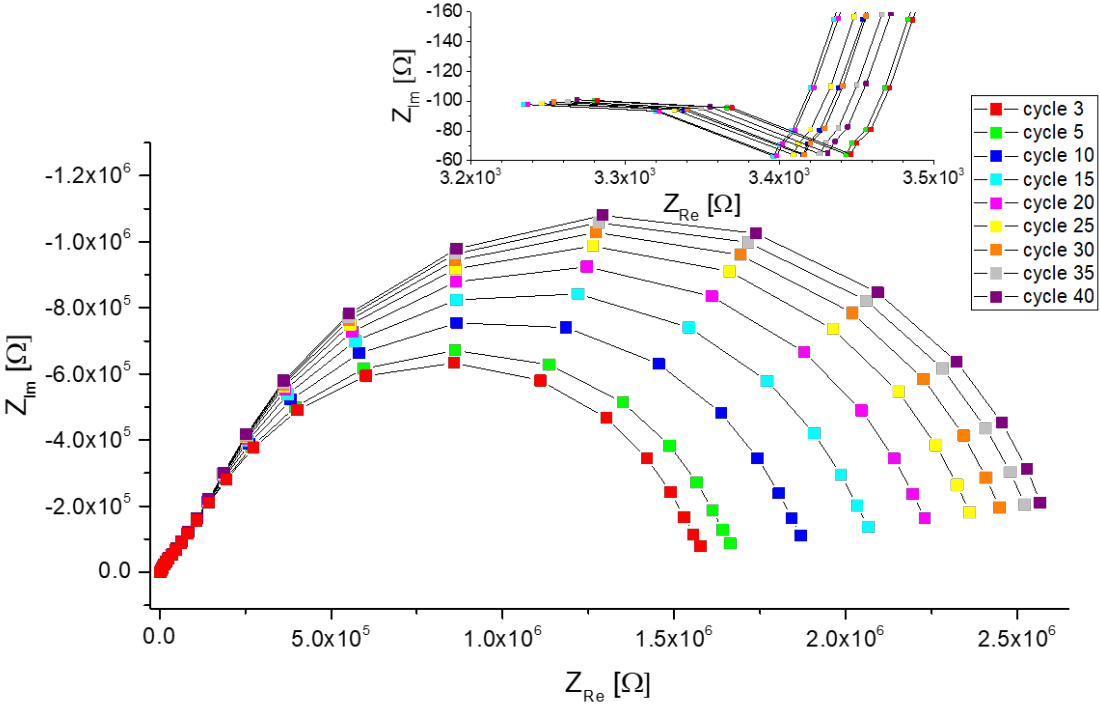


Figure 58: Impedance spectra of the first degradation measurement of a 350 μm electrode on LCM 06 at ca. 593 °C

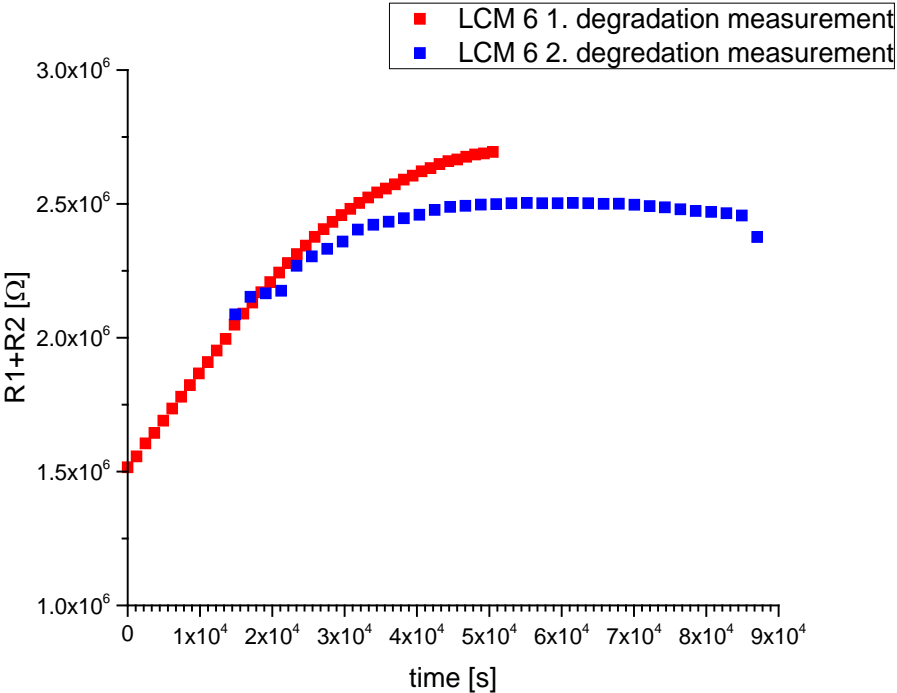


Figure 59: Polarization resistance evolution overnight of two 350 μm electrodes on LCM 06 at ca. 593 °C

In Figure 59, the evolution of the polarization resistance of the previously discussed 350  $\mu\text{m}$  microelectrode (red data points) and a subsequent second degradation measurement on the same sample but of a different 350  $\mu\text{m}$  electrode is shown. At the beginning, they show a similar behavior, later the blue polarization curve flattens and even slightly declines in the end.

Considering the results of the performed impedance measurements a comparison with LSM is very interesting, since the activation energies of LCM and LSM are in the same range, if LCM is heated up only to intermediate temperatures. LSM exhibits activation energies of 1.25 eV - 1.58 eV for finger-type electrodes and 0.95 eV for circular microelectrodes at low temperatures. These oxygen reduction on LSM occurs mostly at the triple phase boundary.[50] Hence, before heating above 550  $^{\circ}\text{C}$  oxygen reduction through the triple phase boundary might be the active reaction pathway for LCM too. This is supported by the fact that, bulk and grain boundary diffusion is even much lower in LCM than in LSM.[77] However, a second process seems to be involved, since the second semicircles of the obtained impedance spectra are always flattened and have to be fitted by two resistor-constant phase element circuits. When heating to temperatures above 550  $^{\circ}\text{C}$  the activation energy and the ASR strongly increase which indicates an irreversible change of the electrode first, strong degradation. More data are required to further analyze the reaction path after this degradation.

## 5. Conclusion

The by far most important parts discussed in this thesis are the van der Pauw measurements and the  $^{18}\text{O}$  exchange experiments combined with ToF-SIMS ion depth profiling. In the following the achievements of this work are summarized.

First of all, A-site doping of LCM with the p-type dopants Sr and Ca lead to a strong enhancement of the electrical conductivity of the investigated bulk samples. Furthermore, Ca decreases the size of the unit cells and Sr changes their structure to rhombohedral. Undoped Bulk LCM exhibits the highest resistivity of all investigated undoped specimens. Thin films made out of LCM are mostly more conductive than the bulk sample. Changing the B-site ratio of Co:Mn enlarges the conductivity, but not as much as A-site doping. A ratio Co:Mn in the bulk of 60:40 is more conductive than a ratio of 40:60. The bulk specimens of both compounds have a smaller resistivity than thin films with the same compositions, except the  $\text{LaCo}_{0.6}\text{Mn}_{0.4}\text{O}_3$  thin film deposited under a background pressure of 100 mTorr.

LCCM and LSCM bulk samples have lower activation energies than bulk LCM.  $\text{LaCo}_{0.6}\text{Mn}_{0.4}\text{O}_3$  has the lowest activation energy of the undoped specimens and the activation energy of  $\text{LaCo}_{0.4}\text{Mn}_{0.6}\text{O}_3$  is in the range of bulk LCM. LSM bulk specimens with 20 % Sr as A-site dopant shows the highest conductivity and the lowest activation energy.

Nearly all thin films have a bend in the Arrhenius plots, with an increased slope above the transition point. A  $\text{N}_2$  atmosphere containing nominal 2 ppm  $\text{O}_2$  was neither able to reduce the bulk samples nor the LCM thin films at any temperature. However a reduced conductivity was obtained in  $\text{LaCo}_{0.4}\text{Mn}_{0.6}\text{O}_3$  and  $\text{LaCo}_{0.6}\text{Mn}_{0.4}\text{O}_3$  thin films under  $\text{N}_2$  atmosphere at temperatures above their transition points.

$^{18}\text{O}$  exchange experiments combined with ToF-SIMS ion depth profiling unveiled the vital role of grain boundary diffusion in LCM thin films. Grain boundaries exhibit a faster diffusivity than the bulk. Moreover the grain boundary diffusion coefficient does not depend on the deposition  $p(\text{O}_2)$ , whereas the grain diffusion coefficient is decreasing with increasing background pressure during thin film growth. With 5 Hz repetition rate higher the grain boundary diffusion coefficients and larger grain sizes can be realized than with a repetition rate of 1 Hz. Thin films produced with a deposition rate of 5 Hz show two more special features: the 500 mTorr and 900 mTorr thin film have a reduced diffusivity, most probably due to ordering effects in the perovskite structure. Secondly an additional diffusion process can be

observed in the 900 mTorr specimen. A connection to the dislocation concentration is suggested. LSC and LSM show a better diffusivity than the investigated LCM thin films.

LCCM was deposited on LAO and STO and investigated by ToF-SIMS tracer ion depth profiling. The obtained profiles were fitted assuming bulk diffusion only. The diffusion coefficient  $D^*$  and oxygen exchange coefficient  $k^*$  increases with increasing background pressure during film growth. Nearly no differences were observed between films deposited on LAO or STO. Thin films on LAO possess slightly reduced  $D^*$  and  $k^*$  values compared to these on STO. Hence no real strain induced difference in diffusivity was observed.

AFM measurements show rougher surfaces if higher background pressures or higher repetition rates were used for thin film deposition. Impedance spectroscopy indicates a change of the LCM sample properties if heated above 550 °C. Keeping them at intermediate temperatures activation energies in the range of LSM can be obtained, thus oxygen reduction via the triple phase boundary in LCM seems to be reasonable.

## 6. Appendix

### 6.1 List of Figures

Figure 1: Schematic of an operating solid oxide fuel cell

Figure 2: Perovskite structure

Figure 3: Triple phase reduction of oxygen, only electronically conductive electrode

Figure 4: Volume (bulk) path of the oxygen reduction reaction, MIEC as electrode

Figure 5: Model of grain boundary diffusion

Figure 6: Pulsed Laser Deposition (PLD)

Figure 7: Calcination program

Figure 8: Sintering program

Figure 9: Left: Overview van der Pauw set up; Right: Sample holder with the four Pt-needles

Figure 10: A) MicroMacro measurement set-up with Pt needle as working electrode contact and Pt sheet as counter electrode B) II-Pot with microscope and gas supply

Figure 11: XRD diffractogram of the LCM target

Figure 12: Peak lists of the target, LCM and  $\text{Co}_3\text{O}_4$  (top to bottom)

Figure 13: XRD diffractogram of the LCCM target

Figure 14: Peak lists of the target, LCCM,  $\text{Co}_3\text{O}_4$  (top to bottom)

Figure 15: XRD diffractogram of the LSCM target

Figure 16: Peak lists of the target, LSCM and  $\text{Co}_3\text{O}_4$  (top to bottom)

Figure 17: XRD diffractogram of the  $\text{LaCo}_{0.4}\text{Mn}_{0.6}\text{O}_3$  target

Figure 18: Peak lists of the target,  $\text{LaCo}_{0.4}\text{Mn}_{0.6}\text{O}_3$  and  $\text{CoO}$  (top to bottom)

Figure 19: XRD diffractogram of the  $\text{LaCo}_{0.6}\text{Mn}_{0.4}\text{O}_3$  target

Figure 20: Peak lists of the target,  $\text{LaCo}_{0.6}\text{Mn}_{0.4}\text{O}_3$  and  $\text{CoO}$

Figure 21: XRD diffractogram of LCM and  $\text{LaB}_6$  powder

Figure 22: Peak lists of the target powder +  $\text{LaB}_6$ ,  $\text{LaB}_6$ , LCM and  $\text{Co}_3\text{O}_4$  (top to bottom)

Figure 23: Basis transformation of a monoclinic unit cell

Figure 24: XRD diffractogram of LCCM +  $\text{LaB}_6$  powder

Figure 25: Peak lists of the target powder +  $\text{LaB}_6$ ,  $\text{LaB}_6$ , LCCM and  $\text{CoO}$

Figure 26: XRD diffractogram of LSCM +  $\text{LaB}_6$  powder

Figure 27: Peak lists of the target powder +  $\text{LaB}_6$ ,  $\text{LaB}_6$ , LCCM and  $\text{Co}_3\text{O}_4$

Figure 28: AFM pictures of LCM 13, 17 and 18

Figure 29: AFM pictures of LCM 19, 20 and 21

Figure 30: Surface roughness  $R_q$  of LCM thin films

Figure 31: TEM images of LCM on a STO (001) single crystal

Figure 32: TEM images of LCM on LAO (001) single crystal (sample LCM 21)

Figure 33:  $\ln(\sigma \cdot T)$  vs the reciprocal temperature of all polycrystalline bulk samples

Figure 34:  $\log(\sigma)$  vs relative Mn concentration of undoped bulk samples

Figure 35: Impact of Ca or Sr A-site doping on the conductivity

Figure 36: Van der Pauw measurements of  $\text{LaCo}_{0.5}\text{Mn}_{0.5}\text{O}_3$  thin films deposited with 1 Hz and 5 Hz repetition rate

Figure 37: Conductivity evolution of LCM thin film samples with background pressure during deposition at 300 °C, 500 °C and 700 °C

Figure 38: Arrhenius plot of the conductivity of  $\text{LaCo}_{0.4}\text{Mn}_{0.6}\text{O}_3$  thin films and corresponding bulk sample, measured under ambient atmosphere and  $\text{N}_2$  containing nominal 2 ppm  $\text{O}_2$

Figure 39: Arrhenius plots van der Pauw measurements of  $\text{LaCo}_{0.6}\text{Mn}_{0.4}\text{O}_3$  thin films

Figure 40: Resistivity comparison and evolution of  $\log(\sigma)$  with deposition  $p(\text{O}_2)$  of  $\text{LaCo}_{0.4}\text{Mn}_{0.6}\text{O}_3$  and  $\text{LaCo}_{0.6}\text{Mn}_{0.4}\text{O}_3$  thin films at 300 °C, 500 °C and 700 °C under ambient air

Figure 41: Tracer ion depth profiles of LCM 13, 15, 18 after diffusion at 573 °C for 3<sup>30</sup> hours

Figure 42: Tracer ion depth profiles of LCM 19, 20, 21 after diffusion at 600 °C for 15<sup>19</sup> hours

Figure 43:  $D^*_g$  and  $D^*_{gb}$  of LCM thin films on LAO at 573 °C (1 Hz samples) and 600 °C (5 Hz samples)

Figure 44:  $k^*_g$  and  $k^*_{gb}$  of LCM thin films on LAO at 573 °C (1 Hz samples) and 600 °C (5 Hz samples)

Figure 45: Grain size and fit quality evolution with increasing  $p(\text{O}_2)$  during thin film growth

Figure 46: <sup>18</sup>O tracer depth profile of LCCM on STO

Figure 47: <sup>18</sup>O tracer depth profile of LCCM on LAO

Figure 48:  $D^*_g$  LCCM samples

Figure 49:  $k^*_g$  LCCM samples

Figure 50: Equivalent circuit

Figure 51: Microelectrodes LCM 05 on YSZ (001) single crystal

Figure 52: Area specific resistance of LCM 05 microelectrodes

Figure 53: ASR of three different electrodes of each size at a set temperature of 600 °C

Figure 54: Calculated activation energies of LCM 05

Figure 55: Microelectrodes of LCM 07 on YSZ (001) single crystals

Figure 56: Impedance spectra LCM 07 temperature cycle (heating up)

Figure 57: Arrhenius plot of LCM 07 for the first heating/cooling cycle on the 250  $\mu\text{m}$  electrode and the second cycle on the 350  $\mu\text{m}$  electrode

Figure 58: Impedance spectra of the first degradation measurement of a 350  $\mu\text{m}$  electrode on LCM 06 at ca. 593  $^{\circ}\text{C}$

Figure 59: Polarization resistance evolution overnight of two 350  $\mu\text{m}$  electrodes on LCM 06 at ca. 593  $^{\circ}\text{C}$

## 6.2 List of Tables

Table 1: PLD deposition parameters

Table 2: Van der Pauw measurement parameters

Table 3: Powder XRD measurement details

Table 4: Bulk activation energies of the electrical conductivity under ambient and  $\text{N}_2$  atmosphere

Table 5: Activation energies of LCM thin films measured under ambient air and  $\text{N}_2$  containing 10 ppm  $\text{O}_2$

Table 6: Activation energies of  $\text{LaCo}_{0.4}\text{Mn}_{0.6}\text{O}_3$  thin films measured under ambient atmosphere and  $\text{N}_2$  containing 10 ppm  $\text{O}_2$

Table 7: Activation energies of  $\text{LaCo}_{0.4}\text{Mn}_{0.6}\text{O}_3$  thin films measured under ambient atmosphere and  $\text{N}_2$  containing 2 ppm  $\text{O}_2$

Table 8: Grain size,  $D^*$  and  $k^*$  values of the LCM thin films deposited with 1 Hz

Table 9: Grain size,  $D^*$  and  $k^*$  values of the samples deposited with 5 Hz

Table 10:  $D^*_g$  and  $k^*_g$  values obtained from LCCM thin films



## 7. References

1. I. Dincer and M.A. Rosen, *Sustainability aspects of hydrogen and fuel cell systems*. Energy for Sustainable Development, 2011. **15**(2): p. 137-146.
2. D. Hart, *Sustainable energy conversion: fuel cells - the competitive option?* Journal of Power Sources 2000. **86**: p. 23-27.
3. H. Turton and L. Barreto, *Long-term security of energy supply and climate change*. Energy Policy, 2006. **34**: p. 2232-2250.
4. Harking, *Congressional record, in proceedings and debates of the 107<sup>th</sup> congress first session*, C. (U.S.), Editor. 2001, United States Government Printing Office: Washington. p. 10323-11816.
5. S. Dunn, *Hydrogen futures: toward a sustainable energy system*. International Journal of Hydrogen Energy 2002. **27**: p. 235-264.
6. A.J. Jacobson, *Materials for solid oxide fuel cells*. Chemistry of Materials, 2010. **22**(3): p. 660-674.
7. K. Kendall, *High-temperature solid oxide fuel cells for the 21st century fundamentals, design and applications chapter 1: Introduction to SOFCs*, ed. K. Kendall and M. Kendall. 2016.: p. 1-24, London, United Kingdom: Elsevier Ltd..
8. A. Egger, E. Bucher, and W. Sitte, *Oxygen exchange kinetics of the IT-SOFC cathode material  $Nd_2NiO_{4+\delta}$  and comparison with  $La_{0.6}Sr_{0.4}CoO_{3-\delta}$* . Journal of The Electrochemical Society, 2011. **158**(5): p. B573-B579.
9. M. Kubicek, Z. Cai, B. Yildiz, H. Hutter, and J. Fleig, *Tensile lattice strain accelerates oxygen surface exchange and diffusion in  $La_{1-x}Sr_xCoO_{3-\delta}$  thin films*. ACSNANO, 2013. **7**(4): p. 3276-3286.
10. J. Fleig, *Solid oxide fuel cell cathodes: Polarization mechanisms and modeling of the electrochemical performance*. Annual Review of Materials Research, 2003. **33**(1): p. 361-382.
11. E. Siebert, A. Hammouche, and M. Kleitz, *Impedance spectroscopy analysis of  $La_{1-x}Sr_xMnO_3$ -yttria stabilized zirconia electrode kinetics*. Electrochimica Acta, 1995. **40**(11): p. 1741-1753.
12. A. Manthiram, J.K. Kim, Y.N. Kim, and K.T. Lee, *Crystal chemistry and properties of mixed ionic-electronic conductors*. Journal of Electroceramics, 2011. **27**(2): p. 93-107.
13. H.Z. Guo, A. Gupta, T. G. Cavarese, and M.A. Subramanian, *Structural and magnetic properties of epitaxial thin films of the ordered double perovskite  $La_2CoMnO_6$* . Applied Physics Letters, 2006. **89**(26): p. 262503 1-3.
14. J.K. Murthy, K. D. Chandrasekhar, S. Murugavel, and A. Venimadhav, *Investigation of the intrinsic magnetodielectric effect in  $La_2CoMnO_6$ : role of magnetic disorder*. Journal of Materials Chemistry C, 2015. **3**(4): p. 836-843.
15. M.P. Singh, S. Charpentier, K.D. Turong, and P. Fournier, *Evidence of bidomain structure in double-perovskite  $La_2CoMnO_6$  thin films*. Applied Physics Letters, 2007. **90**(21): p. 211915-1-211915-3.
16. R.X. Silva, A.S. de Menezes, R.M. Ameid, R.L. Moreira, R. Paniago, X. Marti, H. Reichlova, M. Maryško, M.V. dos S. Rezende, and C.W.A. Paschoal, *Structural order, magnetic and intrinsic dielectric properties of magnetoelectric  $La_2CoMnO_6$* . Journal of Alloys and Compounds, 2016. **661**: p. 541-552.
17. R.I. Dass and J.B. Goodenough, *Multiple magnetic phases of  $La_2CoMnO_{6-\delta}$  ( $0 \leq \delta \leq 0.05$ )*. Physical Review B, 2003. **67**(1).
18. K.D. Truong, J. Laverdière, M.P. Singh, S. Jandl, and P. Fournier, *Impact of Co/Mn cation ordering on phonon anomalies in  $La_2CoMnO_6$  double perovskites: Raman spectroscopy*. Physical Review B, 2007. **76**(13).
19. C.L. Bull, D. Gleeson, and K.S. Knight, *Determination of B-site ordering and structural transformations in the mixed transition metal perovskites  $La_2CoMnO_6$  and  $La_2NiMnO_6$* . Journal of Physics: Condensed Matter, 2003. **15**: p. 4927-4936.

20. B. Orayech, I. Urcelay-Olabarria, G. A López, O. Fabelo, A. Faik, and J. M. Igartua, *Synthesis, structural, magnetic and phase-transition studies of the ferromagnetic La<sub>2</sub>CoMnO<sub>6</sub> double perovskite by symmetry-adapted modes*. Dalton Transactions, 2015. **44**(31): p. 13867-80.
21. J. Burgess, H. Guo, A. Gupta, and S. Street, *Raman spectroscopy of La<sub>2</sub>NiMnO<sub>6</sub> films on SrTiO<sub>3</sub> (100) and LaAlO<sub>3</sub> (100) substrates: Observation of epitaxial strain*. Vibrational Spectroscopy, 2008. **48**(1): p. 113-117.
22. M.P. Singh, K.D. Truong, S. Jandl, and P. Fournier, *Long-range Ni/Mn structural order in epitaxial double perovskite La<sub>2</sub>NiMnO<sub>6</sub> thin films*. Physical Review B, 2009. **79**(22): p. 224421 1-6.
23. M.P. Singh, K.D. Truong, J. Laverdière, S. Charpentier, S. Jandl, and P. Fournier, *Cationic ordering and role of A-site ion in manganese-based double perovskites*. Journal of Applied Physics, 2008. **103**(7): p. 07E315.
24. V. Vashook, D. Franke, J. Zosel, L. Vasylechko, M. Schmidt, and U. Guth, *Electrical conductivity and oxygen nonstoichiometry in the double B mixed La<sub>0.6</sub>Ca<sub>0.4</sub>Mn<sub>1-x</sub>Co<sub>x</sub>O<sub>3-δ</sub> perovskite system*. Journal of Alloys and Compounds, 2009. **487**(1-2): p. 577-584.
25. N. Yuan, X. Liu, F. Meng, D. Zhou, and J. Meng, *First-principles study of La<sub>2</sub>CoMnO<sub>6</sub>: A promising cathode material for intermediate-temperature solid oxide fuel cells due to intrinsic Co-Mn cation disorder*. Ionics, 2014. **21**(6): p. 1675-1681.
26. G.H. Jonker, *Magnetic and semiconducting properties of perovskites containing manganese and cobalt*. Journal of Applied Physics, 1966. **37**(3): p. 1424-1430.
27. H. Gamari-Seale, I.O. Troyanchuk, A.P. Sazonov, K. L. Stefanopoulos, and D. M. Toebbens, *Structure and magnetic order in La<sub>0.7</sub>Ca<sub>0.3</sub>Mn<sub>0.5</sub>Co<sub>0.5</sub>O<sub>3</sub> and La<sub>0.8</sub>Sr<sub>0.2</sub>Mn<sub>0.5</sub>Co<sub>0.5</sub>O<sub>3</sub> perovskites*. Physica B: Condensed Matter, 2008. **403**(17): p. 2924-2929.
28. K.J. Murthy, K.D. Chandrasekhar, H.C. Wu, H.D. Yang, J.Y. Lin, and A. Venimadhar, *Antisite disorder driven spontaneous exchange bias effect in La<sub>2-x</sub>Sr<sub>x</sub>CoMnO<sub>6</sub> (0 ≤ x ≤ 1)*. Journal of Physics: Condensed Matter, 2016. **28**(8): p. 086003.
29. R.A. De Souza, J. Zehnpfenning, M. Martin, and J. Maier, *Determining oxygen isotope profiles in oxides with Time-of-Flight SIMS*. Solid State Ionics, 2005. **176**(15-16): p. 1465-1471.
30. L.J. van der Pauw, *A method of measuring specific resistivity and Hall effect of discs of arbitrary shape*. Philips Research Reports, 1958. **13**(1): p. 1-9.
31. C. Kasl and M.J.R. Hoch, *Effects of sample thickness on the van der Pauw technique for resistivity measurements*. Review of Scientific Instruments, 2005. **76**(3): p. 033907.
32. T. Matsumura and Y. Sato, *A Theoretical study on van der Pauw measurement values of inhomogeneous compound semiconductor thin films*. Journal of Modern Physics, 2010. **01**(05): p. 340-347.
33. D.W. Koon, *Effect of contact size and placement, and of resistive inhomogeneities on van der Pauw measurements*. Review of Scientific Instruments, 1989. **60**(2): p. 271-274.
34. K.A. Borup, E.S. Toberer, L.D. Zoltan, G. Nakatsukasa, M. Errica, J.P. Fleuriol, B.B. Iversen, and G.J. Snyder, *Measurement of the electrical resistivity and Hall coefficient at high temperatures*. Review of Scientific Instruments, 2012. **83**(12): p. 123902.
35. J.A. Kilner, S.J. Skinner, and H.H. Brongersma, *The isotope exchange depth profiling (IEDP) technique using SIMS and LEIS*. Journal of Solid State Electrochemistry, 2011. **15**(5): p. 861-876.
36. N. Minh, *Solid oxide fuel cell technology-features and applications*. Solid State Ionics, 2004. **174**(1-4): p. 271-277.
37. N.Q. Minh, *Ceramic fuel cells*. Journal of the American Ceramic Society, 1993. **76**(3): p. 564-587.
38. K. Gurbinder, *Solid oxide fuel cell components interfacial compatibility of SOFC glass seals chapter 2: Cell voltages, polarisation and performances*. 2016.: p. 43-78, Switzerland: Springer International Publishing AG Switzerland.
39. W. Winkler, *High-temperature solid oxide fuel cells for the 21st century fundamentals, design and application chapter 3: Thermodynamics*, ed. K. Kendall and M. Kendall. 2016.: p. 51-85, London, United Kingdom: Joe Hayton, Elsevier Ltd.

40. J.M. Ralph, A.C. Schoeler, and M. Krumpelt, *Materials for lower temperature solid oxide fuel cells*. Journal of Materials Science, 2001. **36**: p. 1161– 1172.
41. T. Ishihara, M. Honda, T Shibayama, H. Furutan, and Y. Takita, *An intermediate temperature solid oxide fuel cell utilizing superior oxide ion conducting electrolyte, doubly doped LaGaO<sub>3</sub> perovskite*. Ionics, 1998. **4**: p. 395-402.
42. R.D. Shannon, *Revised effective ionic radii and systematic studies of interatomic distances in halides and chalcogenides*. Acta Crystallographica, 1976. **A 32**: p. 751-767.
43. R.D. Shannon and C.T. Prewitt, *Effective ionic radii in oxides and fluorides*. Acta Crystallographica, 1969. **B25**(8): p. 925-946.
44. I. Riess, *Mixed ionic–electronic conductors—material properties and applications*. Solid State Ionics, 2003. **157**(1-4): p. 1-17.
45. C. Wagner, *Equations for transport in solid oxides and sulfides of transition metals*. Progress in Solid-State Chemistry, 1975. **10**(1): p. 2-16.
46. T. Ishihara, *Materials for high-temperature fuel cells chapter 3: Oxide ion-conducting materials for electrolytes*, ed. G.Q. Max Lu. 2013.: p. 97-132, Weinheim, Germany: Wiley-VCH Verlag GmbH & Co. KGaA.
47. J. Sunarso, S. Baumann, J.M. Serra, W.A. Meulenbergh, S. Liu, Y.S. Lin, and J.C. Diniz da Costa, *Mixed ionic–electronic conducting (MIEC) ceramic-based membranes for oxygen separation*. Journal of Membrane Science, 2008. **320**(1-2): p. 13-41.
48. C. Pirovano, A. Rolle, and R.-N. Vannier, *Perovskite and derivative compounds as mixed ionic–electronic conductors*. 2015.: p. 169-188, Wiley-VCH Verlag GmbH & Co. KGaA.
49. S.B. Adler, *Factors governing oxygen reduction in solid oxide fuel cell cathodes*. Chemical Reviews, 2004. **104**(10): p. 4791-4843.
50. T.M. Huber, M. Kubicek, A.K. Opitz, and J. Fleig, *The relevance of different oxygen reduction pathways of La<sub>0.8</sub>Sr<sub>0.2</sub>MnO<sub>3</sub> (LSM) thin film electrodes*. Journal of The Electrochemical Society, 2015. **162**(3): p. F229-F242.
51. M. Prestat, A. Infortuna, S. Korrodi, S. Rey-Mermet, P. Muralt, and L.J. Gauckler, *Oxygen reduction at thin dense La<sub>0.52</sub>Sr<sub>0.48</sub>Co<sub>0.18</sub>Fe<sub>0.82</sub>O<sub>3-δ</sub> electrodes part II: Experimental assessment of the reaction kinetics*. Journal of Electroceramics, 2007. **18**(1-2): p. 111-120.
52. H. Mehrer, *Diffusion in solids fundamentals, methods, materials, diffusion-controlled processes*. in solid state science, ed. M. Cardona, P. Fulde, K. von Kitzling, H.-J. Queisser, R. Merlin, H. Störmer. 2007, Berlin Heidelberg, Germany: Springer-Verlag Berlin Heidelberg.
53. R. Galceran, C. Frontera, L.I. Balcells, J. Cisneros-Fernández, L. López-Mir, J. Roqueta, J. Santiso, N. Bagueés, B. Bozzo, A. Pomar, F. Sondiumenge, and B. Martinez, *Engineering the microstructure and magnetism of La<sub>2</sub>CoMnO<sub>6-δ</sub> thin films by tailoring oxygen stoichiometry*. Applied Physics Letters, 2014. **105**(24): p. 242401.
54. C.L. Bull, R. Mortimer, G. Sankar, D. Gleeson, C.R.A. Catlow, I.G. Wood, and G.D. Price, *Structural & physical properties of the binary transition metal- containing perovskite La<sub>2</sub>CoMnO<sub>6</sub>*. Synthetic Metals, 2001. **121**: p. 1467-1468.
55. W. Zhou, Z. Shao, C. Kwak, and H.J. Park, *Materials for high-temperature fuel cells chapter 2: Advanced cathodes for oxide fuel cells*, ed. G.Q. Max Lu. 2013.: p. 49-96, Weinheim, Germany, Wiley-VCH Verlag GmbH & Co. KGaA.
56. R.J.D. Tilley, *Defects in solids*, ed. R.B. King. 2008, Hoboken, New Jersey: John Wiley & Sons Inc.
57. D. Gupta, *Diffusion processes in advanced technological materials chapter 1: Diffusion in bulk solids and thin films: Some phenomenological examples*, ed. D. Gupta. 2005.: p. 1-68, Norwich, New York: William Andrew Inc.
58. G. Tiwari and R.S. Mehrotra, *Diffusion processes in advanced technological materials chapter 2: Solid state diffusion and bulk properties*, ed. D. Gupta. 2005.: p. 69-111, Norwich, New York: William Andrew Inc.
59. Y. Mishin and C. Herzig, *Grain boundary diffusion: recent progress and future research*. Materials Science and Engineering, 1999. **A260**: p. 55-71.

60. J.W. Evans, *Approximations to the Whipple solution for grain boundary diffusion and an algorithm for their avoidance*. Journal of Applied Physics, 1997. **82**(2): p. 628-634.
61. R. Smoluchowski, *Theory of grain boundary diffusion*. Physical Review, 1952. **87**(3): p. 482-487.
62. J.C. Fisher, *Calculation of diffusion penetration curves for surface and grain boundary diffusion*. Journal of Applied Physics, 1951. **22**(1): p. 74-77.
63. D.P. Norton, *Pulsed laser deposition of thin films application-led growth of functional materials chapter 1: Pulsed laser deposition of complex materials: Progress towards applications*, ed. R. Eason. 2007.: p. 3-31 , Hoboken, New Jersey: John Wiley & Sons Inc.
64. H.M. Christen and G. Eres, *Recent advances in pulsed-laser deposition of complex oxides*. Journal of Physics: Condensed Matter, 2008. **20**(26): p. 264005-1-264005-16.
65. G. Rijnders and D.H.A. Blank, *Pulsed laser deposition of thin films application-led growth of functional materials chapter 8: Growth kinetics during Pulsed laser deposition*, ed. R. Eason. 2007.: p. 177-191, Hoboken, New Jersey: A John Wiley & Sons Inc.
66. L.J. van der Pauw, *A method of measuring the resistivity and Hall coefficient on lamellae of arbitrary shape*. Philips Technical Review, 1958/59. **20**(8): p. 220-224.
67. M.P. Pechini, *Method of preparing lead and alkine earth titanates and niobates and coating method using the same to form a capacitor*, U.S.P. Office, Editor. 1967: United States of America.
68. I.A. Farbut, I.V. Romanova, and S.A. Kirillov, *Optimal design of powdered nanosized oxides of high surface area and porosity using a citric acid aided route, with special reference to ZnO*. Journal of Sol-Gel Science and Technology, 2013. **68**(3): p. 411-422.
69. *Ausstattung x-ray center TU Wien*. [web site, 10. Mai 2015 19.05.2017]; Available from: <http://xrc.tuwien.ac.at/ausstattung/>.
70. M. Gerstl, T. Frömling, A. Schintlmeister, H. Hutter, and J. Fleig, *Measurement of <sup>18</sup>O tracer diffusion coefficients in thin yttria stabilized zirconia films*. Solid State Ionics, 2011. **184**(1): p. 23-26.
71. G. Holzlechner, M. Kubicek, H. Hutter, and J. Fleig, *A novel ToF-SIMS operation mode for improved accuracy and lateral resolution of oxygen isotope measurements on oxides*. Journal of Analytical Atomic Spectrometry, 2013. **28**(7): p. 1080-1089.
72. R.A. De Souza, and R.J. Chater, *Oxygen exchange and diffusion measurements: The importance of extracting the correct initial and boundary conditions*. Solid State Ionics, 2005. **176**(23-24): p. 1915-1920.
73. T. Sun, J. Ma, Q.Y. Yan, Y.Z. Huang, J.L. Wang, and H.H. Hng, *Influence of pulsed laser deposition rate on the microstructure and thermoelectric properties of Ca<sub>3</sub>Co<sub>4</sub>O<sub>9</sub> thin films*. Journal of Crystal Growth, 2009. **311**(16): p. 4123-4128.
74. J.H. Kuo, H.U. Anderson, and D.M. Sparlin, *Oxidation-reduction behavior of undoped and Sr-doped LaMnO<sub>3</sub>: Defect structure, electrical conductivity, and thermoelectric power*. Journal of Solid State Chemistry, 1990. **87**: p. 55-63.
75. J. Mizusaki, J. Tabuchi, T. Matsuura, S. Yamauchi, and K. Fueki, *Electrical conductivity and Seebeck coefficient of nonstoichiometric La<sub>1-x</sub>Sr<sub>x</sub>CoO<sub>3-δ</sub>*. Journal Electrochemical Society, 1989. **1989**(7): p. 2082-2088
76. Y. Adachi, N. Hatada, and T. Uda, *Sintering, electrical conductivity, oxygen nonstoichiometry, thermal expansion and thermal stability of ruddlesden-popper type cobaltite La<sub>4</sub>Co<sub>3</sub>O<sub>10</sub>*. Journal of The Electrochemical Society 2016. **163**(9): p. F1084-F1090.
77. E. Navickas, T.M. Huber, Y. Chen, W. Hetaba, G. Holzlechner, G. Rupp, M. Stöger-Pollach, G. Friedbacher, H. Hutter, B. Yildiz, and J. Fleig, *Fast oxygen exchange and diffusion kinetics of grain boundaries in Sr-doped LaMnO<sub>3</sub> thin films*. Physical Chemistry Chemical Physics, 2015. **17**(12): p. 7659-69.
78. T.M. Huber, A.K. Opitz, M. Kubicek, H. Hutter, J. Fleig, *Temperature gradients in microelectrode measurements: Relevance and solutions for studies of SOFC electrode materials*. Solid State Ionics, 2014. **268**: p. 82-93.